Universidade federal de pernambuco
Departamento de fisica – CCEN
Programa de Pós-Graduação em Física

Edwin Danelli Coronel Sánchez

Nanoscale magnetometry with a microcontroller-based magnetometer using a single nitrogen-vacancy defect in nanodiamond

Recife
2020

Edwin Danelli Coronel Sánchez

Nanoscale magnetometry with a microcontroller-based magnetometer using a single nitrogen-vacancy defect in nanodiamond

Tese apresentada ao Programa de Pós-Graduação em Física da Universidade Federal de Pernambuco, como requisito parcial para a obtenção do título de Doutor em Física.

Research area: Optics

Advisor: Prof. Leonardo de Souza Menezes

Recife
2020

Catalogação na fonte
Bibliotecária Arabelly Ascoli CRB4-2068

S211n Sánchez, Edwin Danelli Coronel
Nanoscale magnetometry with a microcontroller-based magnetometer using a single nitrogen-vacancy defect in nanodiamond / Edwin Danelli Coronel Sánchez. – 2020.
111 f.: il. fig.

Orientador: Leonardo de Souza Menezes
Tese (Doutorado) – Universidade Federal de Pernambuco. CCEN. Física. Recife, 2020.
Inclui referências e apêndices.

1. Microscopia óptica confocal. 2. Nanodiamante. 3. Fotoluminescência. 4. Ressonância de espin eletrônico. I. Menezes, Leonardo de Souza (orientador). II. Título.

535.2 CDD (22. ed.) UFPE-CCEN 2020-114

Edwin Danelli Coronel Sánchez

Nanoscale magnetometry with a microcontroller-based magnetometer using a single nitrogen-vacancy defect in nanodiamond

Tese apresentada ao Programa de Pós-Graduação em Física da Universidade Federal de Pernambuco, como requisito parcial para a obtenção do título de Doutor em Física.

Aprovada em: 22/05/2020

BANCA EXAMINADORA

Participação via Videoconferência

Prof. Leonardo de Souza Menezes
Orinentador
Universidade Federal de Pernambuco

Participação via Videoconferência

Prof. Anderson Monteiro Amaral
Examinador interno
Universidade Federal de Pernambuco

Participação via Videoconferência

Prof. José Wellington Rocha Tabosa
Examinador interno
Universidade Federal de Pernambuco

Participação via Videoconferência

Prof. Felipe Arruda de Araújo Pinheiro
Examinador externo
Universidade Federal do Rio de Janeiro

Participação via Videoconferência

Prof. Thiago Pedro Mayer Alegre
Examinador externo
Universidade Estadual de Campinas

This thesis is dedicated to my parents Zacarias and Alicia. Thanks for giving me the support and best education that you could. I love you!

Acknowledgements

I would like to express my special appreciation and thanks to my advisor Leonardo Menezes by the unconditional support along all this learning stage. I am grateful to him because despite the difficulties that arose in the laboratory he always helped me to find solutions to overcome them, besides encouraging me to follow with the research showing his enthusiasm and characteristic sense of humor that everyone knows in the lab.

The Professors of the Physics Department for their contribution spending time in conversations about physics in the corridors of the department and/or in the seminars. Administrative staff, particularly Ailton da Silva and Alexsandra Soares who are always supporting us in any urgent procedure we need. Thanks to Valdomiro da Silva and João de Paula Filho of the mechanics shop by the design of several of the pieces used in the experiments. Electronics shop technician Daniel Melo, to whom I am deeply grateful because he made his expertise available to the development of the various home-made electronic systems used in this work.

I want to thank the people who contributed from the beginning of the project: Professor Oliver Benson (Humboldt University of Berlin) for opening the doors of his laboratory to works with his Ph.D. students, like Nikola Sadzak, Bernd Sontheimer, Niko Nikolay, and Florian Böhm who always shared their experiences and knowledge of physics and programming. Also, Regina Rheinländer always supporting me during my whole stay in Germany.

I would like to express my appreciation to those who were involved directly in the development of the magnetometer used in this project: Thanks a lot Professor Anderson Amaral for his patient and time dedicated always giving me his support. Daniel Melo who was in charge of the electronic design not only of this magnetometer but all electronic built for this project and finally Allison Pessoa who was in charge of the microcontroller programming, definitively without him it would have been very difficult to carry out this project. Thanks, Jefferson, Rodrigo, and Igor (Nano Optics lab at UFPE) for supporting

me in any issues arising in the laboratory. Thanks to all people who always help me when I need it, for the nice conversations and shared experiences: Kelly, Winnie, Manoel, Albert, Talita, Jessica, Maxwell, Melissa among others.

I also want to thank all my heart to my parents, brother, and sister for giving me their unconditional support during my whole formation stage. Thanks, because in our difficult condition they did everything possible sacrificing many things to realize my dreams. These achievements are also their achievements. I hope they are proud of me and I haven't ever disappointed them. Finally to my partner Saira Esperanza who during this period of studies gave me her help and sacrifice to support me. Thank for giving me the smile that makes my soul happy. I am indebted with you.

≪ Nobody ever figures out what life is all about, and it doesn't matter. Explore the world. Nearly everything is really interesting if you go into it deeply enough [1]≫

Richard Feynman

Abstract

In the last few years, the study of the negatively charged nitrogen-vacancy (NV^-) defect in diamond has increased in many areas of science because of its interesting optical and spin properties, such as high photostability and possibility of performing coherent control of their spin states even under ambient conditions. This makes the NV^- defect attractive for the development of diverse application areas such as nanomagnetometry, quantum information processing and nanobiothermometry, as well as for the development of new applications in the spintronic area and quantum technology. The NV^- defect is a solid-state system that presents extraordinary sensitivity to magnetic fields and allows sensing schemes with high spatial resolution. Moreover, its paramagnetic triplet ground state evidences predominantly spin-spin interaction that splits the spin projection $m_{gs} = 0$ from the degenerate state $m_{gs} = \pm 1$ by $D_{gs} = 2.87$ GHz. With the action of an external local magnetic field the degeneracy is lifted by Zeeman effect and the energy levels splitting is proportional to the projection of magnetic field along to the defect symmetry axis, to which the magnetic dipole moment of the NV^- center is parallel. This particular characteristics, together with its nanometric scale, allows building nanomagnetometers that work simply by probing the electronic ground state by Optically Detected Magnetic Resonance (ODMR). In the present work, an ODMR−based system for performing nanomagnetometry was developed using an Arduino Due board microcontroller as a main tool for the magnetometer implementation by means of an established in-system programming. The implemented nanomagnetometry method is simple and relies on the frequency modulation of the NV^- defect electron spin resonance (ESR). This is done by introducing in the system an alternated magnetic field produced by also alternated current square pulses that passes through a wire loop located in the vicinity of the nanodiamond. An important fact is that the method uses a single microwaves source to excite spin transitions. The alternating magnetic field produced by the switching of an electric current modulates the NV^- ESR central frequency at a conveniently chosen frequency. Since an in-system programming is established, it is possible compute a differential photon counting technique in phase with

the modulated field obtaining a signed error signal. The microcontroller is responsible both for controlling the modulated field through the current pulse and for calculating the error signal. The resulting imbalance in photon counts is then used to detect the Zeeman shift in the ESR central frequency applying an ODMR approach. The developed system has a reasonable sensitivity of 4 $\mu\mathrm{T}/\sqrt{\mathrm{Hz}}$ and is able to measure magnetic field variations at a rate of around 4 mT/s. This system was used for nanoimaging the inhomogeneous spatial magnetic field profile of a magnetized steel microwire, and a spatial magnetic field gradient of 13 μT/63 nm was measured. Besides, its usefulness in nanoscale imaging of magnetic fields, the present work can be of interest in development of compact nanodiamond based magnetometer.

Keywords: Confocal optical microscopy. Nanodiamond. Photoluminescence. Electron spin resonance. Nanomagnetometry.

Resumo

Nos últimos anos, o estudo dos defeitos do nitrogênio-vacância negativamente carregados (NV^-) em diamante tem aumentado em muitas áreas da ciência devido às suas interessantes propriedades ópticas e de spin, assim como a alta fotoestabilidade e possibilidade de controle coerente de seus estados de spin mesmo em condições ambientes. Essas características tornam o defeito de NV^- atraente em diversas áreas da aplicação, como a magnetometria, processamento de informação quântica e nanobiotermometria, como também para o desenvolvimento de novas aplicações nas áreas da spintrônica e tecnologia quântica. O NV^- é um sistema de estado sólido com sensibilidade extraordinária a campos magnéticos e permite esquemas de detecção com alta resolução espacial. Além disso, seu estado fundamental tripleto de spin, paramagnético, evidencia predominantemente a interação spin-spin que separa a projeção de spin $m_{gs} = 0$ do estado degenerado $m_{gs} = \pm 1$ em $D_{gs} = 2.87$ GHz. Com a interação de um campo magnético local externo, a degenerescência é quebrada por efeito Zeeman e a amplitude do splitting é proporcional à projeção do campo magnético ao longo do eixo de simetria do defeito NV^-, que é paralelo ao seu momento de dipolo mágnetico permanete. Esta particular característica, junto com a sua escala nanométrica, permite construir magnetômetros operando a partir da simples sondagem do estado fundamental eletrônico usando a técnica de ressonância magnética detectada opticamente (sigla em inglês: ODMR). No presente trabalho, um sistema baseado em ODMR foi desenvolvido para construção de um magnetômetro apresentando resolução espacial nanométrica, que usa o microcontrolador da placa Arduino Due como a principal ferramenta para a implementação. O método escolhido para nanomagnetometria é simples e depende da frequência de modulação da ressonância magnética do spin eletrônico do defeito NV^-. Isso é feito introduzindo no sistema um campo magnético alternado, gerado por pulsos quadrados também alternados de corrente que percorrem uma pequena espira nas proximidades do nanodiamante. O campo magnético alternado produzido pela comutação de uma corrente elétrica modula a frequência central da RSE numa frequência convenientemente escolhida. Mediante uma programacão é possível calcular uma contagem diferencial

de fótons em fase com o campo modulado obtendo um sinal de erro. O microcontrolador é responsável tanto pelo controle do campo modulado por meio do pulso da corrente quanto pelo cálculo do sinal de erro. O desbalanço resultante nas contagens dos fótons é usado para detetar o deslocamento Zeeman da frequência central da RSE do NV^-, aplicando a abordagem de ODMR. O sistema desenvolvido tem uma sensibilidade razoável de 4 $\mu T/\sqrt{Hz}$ e é capaz de medir variações de campo magnético a uma taxa cerca de 4 mT/s. Este sistema foi utilizado para obter uma nanoimagem do perfil do campo magnético não homogêneo de um microfio de aço magnetizado, tendo sido medido um gradiente espacial de campo magnético de 13 μT/63 nm. Além da utilidade nas imagens em nanoescala de campos magnéticos, o presente trabalho pode ser de interesse no desenvolvimento de magnetômetros compactos baseados em nanodiamantes.

Palavras-chave: Microscopia óptica confocal. Nanodiamante. Fotoluminescência. Ressonância de spin eletrônico. Nanomagnetometria.

List of Figures

Contents

Chapter 1

Introduction

Measurement of magnetic fields is a basic technique to characterize materials, so a few methods are developed for this task based on the use of induction coils, fluxgate magnetometers, magnetoresistive and Hall effect magnetometers, magneto-optical and optically pumped magnetometers [2–4]. The superconducting quantum interference devices (SQUIDs) [5] are the most effective magnetic flux detector due to their high sensitivity and ability to operate in a large magnetic field. They can have centimeter sizes and reach sensitivities down to 1 fT/$\sqrt{\text{Hz}}$. The limitation of this kind of sensors is that they require cryogenic temperatures since its basic operation consists of the use of superconductors, making difficult the use of samples that can be studied [6].

Another kind of magnetometer uses atoms, enclosed within a vapor cell [7], and that depends on accurate measurement of the Larmor spin precession frequency ω_L of the atomic spins caused by a magnetic field B. This frequency is given by [8]

$$\omega_L = \gamma' B \tag{1.1}$$

where γ' is the gyromagnetic ratio, which is the ratio of the magnetic moment to the angular momentum. In alkali-metal atoms (K, Rb and Cs) γ' is generally on the order of $2\pi \times 5$ kHz/μT. The advantage of the atomic magnetometer over SQUID magnetometers is that the first one does not require cryogenic temperatures [9]. The sensitivity of the atomic magnetometer reaches $\sim$ 1 fT/$\sqrt{\text{Hz}}$ with a limitation given by spin-exchange collisions in

atoms [10]. To overcome this limitation one can operate the magnetometer with a very low magnetic field to eliminate relaxation due to spin-exchange collisions reaching a sensitivity of the ~ 0.01 fT/$\sqrt{\text{Hz}}$ [11].

In these techniques mentioned above the dimension of the magnetometers are on the centimeter scale and their systems are not appropriates to be easily manipulated. However, for other applications, it could be necessary to perform magnetic field measurements on the nanoscale. Understanding the magnetic properties in the nanoscale is an important tool in the creation of several devices with novel functionalities [12–14]. For example, ultra dense magnetic data storage relies on sensing magnetic field gradients at the nanoscale [15], while nanoscopic spintronics devices may play an important role in information processing [16]. The measurement and control of magnetic fields with nanoscale accuracy are also relevant in biotechnology, where for example the targeted application of forces [17] and torques [18] is needed. Nanomagnetometry has a strategic status in such areas and using a single spin within a solid state matrix as the magnetic field sensor allows the enhancement of the spatial resolution provided by such a magnetometer.

The nitrogen-vacancy (NV) defect in nanodiamond is a solid state system with extraordinary characteristics, as photostability and long spin coherence times [19–21]. Due to the high concentration of N_2 in the environment, defects in the diamond lattice, as nitrogen inclusions, can be found naturally in nanodiamonds (NDs). However, different techniques as High Pressure High Temperature (HPHT) treatment [22] and Chemical Vapor Deposition (CVD) process [23] have been developed to produce a synthetic diamond containing NV defects.

The NV defect belongs to the C_{3v} group symmetry in a model that involves 5 electrons, three of them due to the three nearest carbon atoms, and two from the nitrogen atom. When the NV center captures an electron from the diamond lattice (negatively charged NV: NV^-), the defect presents a magnetic dipole moment well oriented along the ND crystalline lattice [24] and behaves like a single atom in its optical and spin properties. The NV^- center can be optically excited with green light and detected using its photoluminescence

(PL) in the red spectral region [25,26]. A single NV^- center emits single photons efficiently even at room temperature [27] and at a high rate due to characteristics as large absorption cross-sections, a relatively short lifetime of the excited state and high emission efficiency [28]. The diamond host matrix also protects the NV^- from the environment, which leads to a chemically stable emitter without suffering from blinking or bleaching. When hosting a NV^-, the ND is a highly stable light emitter and presents low cytotoxicity, becoming a nanoscale fluorescent source adequate for imaging biological systems as well [29, 30]. Particularly important for magnetic field sensing, the electronic ground state presents a spin triplet that can be optically pumped with a linearly polarized green light (typically at 532 nm) to its magnetic sublevel $m_{gs} = 0$ [31]. A non-radiative intersystem crossing substantially couples the excited states with $m_{es} = \pm 1$ to an intermediate singlet state with $m_s = 0$ which then decays to the $m_{gs} = 0$ ground state magnetic sublevel. Spin dynamics of NV^- defect allows to subsequently apply a microwave (MW) field around 2.87 GHz which can be used to couple the ground state sublevel $m_{gs} = 0$ to the sublevels $m_{gs} = \pm 1$, that increases the probability of nonradiative decay via intersystem crossing from the excited electronic states. This photophysics can be used in Electron Spin Resonance (ESR) processes, leading to a spectroscopic technique called Optically Detected Magnetic Resonance (ODMR) [32, 33], whose signal exhibits changes in its PL fluorescence that depend on the electronic spin transition. In this system, the $m_s = \pm 1$ sublevels are degenerate at zero external magnetic field and present coupling characteristics with the electronically excited states. This coupling leads to a non-negligible nonradiative decay route that reduces the PL signal by typically $\sim 20\%$ when the MW field frequency, ν_{MW}, couples $m_s = 0$ to one of the $m_s = \pm 1$ sublevels. One thus can record the NV^- PL signal as a function of the MW frequency and build an ODMR curve where a dip determines the ESR frequency.

Practical implementations of NV^- based magnetometers often use lock-in techniques [34]. By modulating a variable of the magnetometer and locking the detection system to this modulation frequency it is possible to remove systematic effects in the ODMR detection. The most evident parameter to modulate is the MW field frequency, ν_{MW} [35,36]. However,

while some sophisticated MW sources allow modulating their output frequency directly, as in [35], many are not able to have their outputs modulated at kHz frequencies or above. This is an important limitation since it implies a lower bound for the device time resolution. An alternative to avoid this limitation in lab-scale experiments consists in the use a fast switching element to alternate between two different MW sources tuned at distinct frequencies [36], which in turn increases the complexity and cost of the magnetometer.

In this work, an alternative approach to use a single MW source in which output frequencies cannot be modulated at kHz rates or above is presented. Instead of producing a modulation in the MW field directly, a small modulation in the NV^- ESR frequency was produced by applying a modulated external magnetic field through a home-made, computer controllable square wave current generator and a wire loop. Given the scientific and technological relevance of producing compact and sensitive magnetometers [35, 37], the present proposal can provide a useful alternative to some of the technical challenges in system integration.

This Thesis brings results on nanomagnetometry exploiting single NV^- defects in individual NDs, using an approach compromising spatial resolution, sensitivity and experimental simplicity based on a phase-locked loop photon counting system implemented using an Arduino Due board. Chapter 2 discusses two common methods to obtain NV defects in diamond and mentions the main properties of these NV defects taking into account the electronic structure and the photophysics arising from their spin sublevels. Then, the spin Hamiltonian of the NV^- defect is studied and solved for taking few considerations into account to get an expression for the ESR frequencies. Finally, using this expression two methods are described to determine the orientation of the NV^- defect magnetic dipole moment axis, that it is determinant to perform magnetometry, which is the aim of this work. In chapter 3, it is briefly discussed the confocal microscopy technique and the experimental setup used to detect nanodiamonds. Then, it is explained the design and calibration of the electromagnets used to apply both DC and AC magnetic fields in order to determine the orientation of the NV^- axis. Also, it is done a description of the implementation and operation of the nanomagnetometer developed based on Arduino Due, which performs different tasks synchronously with peripheral devices. In chapter 4, the experimental results

are shown, beginning with the characterization of the nanodiamond, which consists in the detection of one nanodiamond and its photoluminescence study by Hanbury-Brown and Twiss (HBT) interferometry to determine whether it has a single photon source behavior. Besides, a study of the ODMR spectrum as a function of an external magnetic field is performed to measure the orientation of the NV^- dipole moment axis. Then, the method used in this work to measure magnetic fields is described, including an evaluation of the modulation frequency and sampling time to optimize the magnetometer. Measurements to check the linearity response of the system are performed as well as the capability to measure AC magnetic fields is verified. At the end of this chapter, a magnetic field imaging is performed by scanning a magnetized microwire in a micro region over the nanodiamond. Finally, in chapter 5 the conclusions and perspectives of this work are presented.

Chapter 2

The NV defect in diamond

In this chapter, the main optical and spin properties of the NV defect in diamond are discussed. In order to understand why the NV system is considered so important in different areas of condensed matter and others, the process that involves the manipulation of the NV defect spin sublevel is described. Furthermore, as the main interest of this work is to perform magnetometry experiments it will be necessary to study the interaction of an external magnetic field with the NV spin sublevels by means of the spin Hamiltonian of the system, allowing to obtain a relation between the ESR frequency and magnetic field that is employed to measure the NV magnetic dipole moment axis orientation as well as to perform magnetometry. Finally, an overview about concepts involved in magnetometry, crucial for our experiments, will be given.

2.1 Diamond and NV defect formation

Diamond has been studied for years and today the industry takes advantage of many of its properties such as mechanical hardness, heat conductivity, and optical transparency [38]. Besides this, it is chemically inert and resistant to most acids and bases. The combination of all these features only in one material, makes the diamond very useful in diverses technological applications [39]. Furthermore, diamond attracts attention because it is a wide bandgap semiconducting material, with a gap of 5.5 eV [40, 41] that corresponds to wavelengths in the ultraviolet region, meaning that visible light could be transmitted

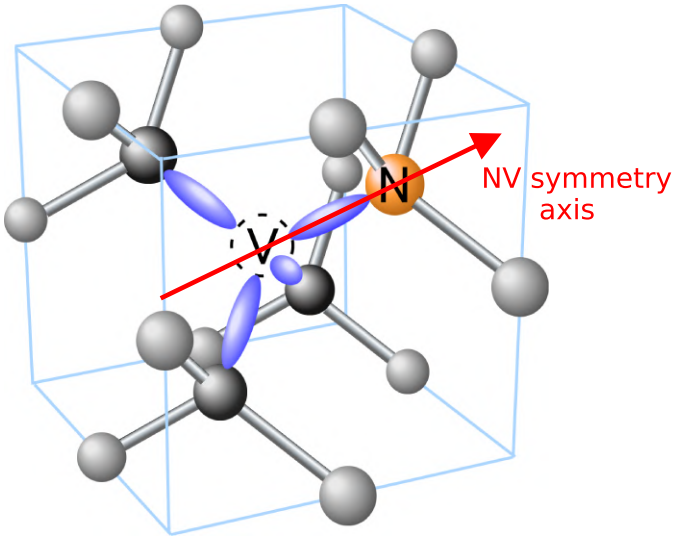

Figure 1: Scheme depicting the diamond crystallographic structure (face centered cubic lattice) with the NV defect in the lattice. The defect consists of a substitutional nitrogen (N) atom next to a missing carbon atom - a vacancy (V) [45].

through it. This gives diamond the appearance of a colorless material. Nowadays, it is known that diamond is also found in various colors due to impurities incorporated in the crystal structure, which can significantly alter some of its properties [42, 43]. Actually, the change in color is just for decoration and aesthetic; the incredible of this fact is that some impurities give diamond interesting spin and optical properties [44].

In fact, some impurities in diamond attract great attention because their quantum behavior and photostability even under ambient conditions [45] because its high Debye temperature that ensure that NV defects in NDs are in thermal equilibrium with the local heat environment. These particular features, among others, make diamond an excellent candidate for applications in solid-state quantum technologies [43, 46]. Impurities present in diamond structure are known as defects or color centers and can occur in natural or synthetic diamond. Despite the fact that there exist hundreds of defect kinds in diamond, one in particular will be studied, which has been for the last decade the most promising in the implementation of quantum cryptography system, quantum information processing and quantum sensing: the NV defect in diamond (see figure 1).

Nitrogen is the most common impurity studied in diamond and it is found as a substitutional atom inside the crystalline lattice. The structure created with one nitrogen impurity and one vacancy in its nearest neighborhood is the NV point defect. A few methods exist to create NV defects in diamond, among which High Pressure High Temperature (HPHT) and Chemical Vapor Deposition (CVD) are the best known [47, 48]. By irradiating electrons or ions with a high energy ranging from keV up to few MeV it is possible to produce vacancies in the diamond lattice. Those vacancies can diffuse as a result of an annealing treatment, taking them towards a lattice site adjacent to the nitrogen atom, thus forming the NV defects [49]. An interesting point is that it is possible to place the NV defect at a certain depth just controlling the energy of the irradiation particles. This is important because one could increase the sensitivity to measure magnetic fields by placing NV defects with negative charge (see next section) close enough (generally < 5 nm) to the surface of diamond [50] since the interaction with its local environment gets increased. However, locating the NV defect too close to the diamond surfaces is a problem for magnetometry applications because the coherence time decrease and the photoluminescence gets less stable [51].

For magnetometry is required a triplet spin system exhibiting a Zeeman behavior in the presence of magnetic fields. This system is presented by the negatively charge nitrogen vacancy (NV^-) defect, which rises when a NV defect capture an electron from the crystal lattice resulting in a NV^- defect. The next sections will be a starting point to understand the properties of the NV^- defect in diamond and how these can be used in nanomagnetometry.

2.2 Electronic structure of the NV defect in diamond

The structure of the NV defect in diamond has a C_{3v} symmetry (figure 2a), which means that for rotations multiple of 120° around the NV symmetry axis the system is unchanged [52]. In this basic configuration (5 optically active electrons), the NV system commonly receives the name of neutral NV defect (NV^0). When a sixth electron coming

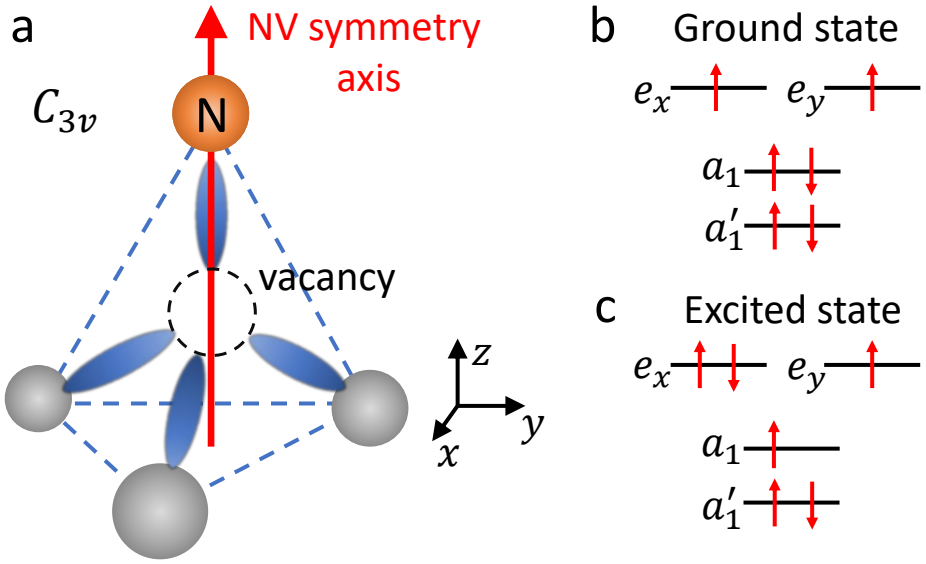

Figure 2: (a) Tetrahedral geometry of the NV defect depicting the C_{3v} symmetry and definition of the xyz reference frame, in which the defect symmetry axis is oriented along z. The red arrow shows the NV symmetry axis along which the magnetic dipole moment of the defect lays. (b) and (c) Schematic of the NV^- orbital level structure in the ground and excited states, respectively, showing for each one the four orbitals ($a_1^{'}$, a_1, e_x and e_y) [56].

from elsewhere in the crystal lattice is captured by the vacancy [53] the result is a negative total charge, and the defect is conventionally labeled as NV^-. The NV defects, however also present positively charged states, NV^+ [43]. In this thesis, one will focus in the particular case when the NV is negatively charged (NV^-).

Generally, the formalism used to describe the electronic structure of the NV^- defect is the group theory [54, 55]. By using symmetry properties, one can construct a set of four molecular orbitals, which form a base given by $\{a_1^{'}, a_1, e_x, e_y\}$ [56]. When the NV^- system is in its ground state, all electrons are placed in their corresponding orbitals maintaining the $a_1^{'}$ and a_1 orbitals completely filled and two electrons occupying each of the e_x and e_y orbitals, following the Aufbau principle [54, 55] (figure 2b). Similar to electronic configuration of atoms, in this case the ground state has configuration $a_1^{'2}a_1^2e^2$, with the number of occupying electrons indicated in the superscript. If an excitation source has the required energy to excite one electron, this is promoted to either e_x or e_y orbitals, assuming a configuration $a_1^{'2}a_1^1e^3$ [55–57] (figure 2c). In both cases, the total spin angular

momentum is $S = 1$ and ground and excited states are spin triplets. The properties of this kind of system when optically activated will be discussed in the next section.

2.3 NV$^-$ energy levels and spin properties

The NV$^-$ defect energy levels are built based on their spin angular momentum. As discussed above, as two out of six electrons trapped in the vacancy are unpaired the total spin is $S = 1$, allowing formation of spin triplets in the ground $|g\rangle$ and first excited $|e\rangle$ electronic states [58]. Illuminating the NV$^-$ defect typically with green light originates electronic transitions that lead to a broad vibronic PL spectrum from 600 to 800 nm and a zero phonon line (ZPL) at 1.95 eV (637 nm) that involves no phonons [38], as shown in figure 3. The ZPL is the optical transition at which an excitation or relaxation is not phonon assisted and is located at a frequency determined by the intrinsic difference in energy levels between ground and excited state.

As already mentioned, the spin ground state is a triplet, with projections along the NV$^-$ symmetry axis that will be labeled as $m_{gs} = 0$ indicating the lower spin state and $m_{gs} = \pm 1$ as a degenerate doublet state. Both are separated predominantly by spin-spin interaction with a zero field splitting (ZFS) $D_{gs} \approx 2.87$ GHz. Besides, in thermal equilibrium, these spin ground states are equally populated at room temperature, according to the Boltzman distribution [73]. In the excited state the ZFS is $D_{es} \approx 1.42$ GHz [32, 59].

Shining the defect with a linearly polarized continuous wave (CW) off-resonance laser (532 nm), spin-conserving optical transitions between the NV$^-$ electronic levels are excited according with the optical selection rules, which means that the allowed transitions occur when $\Delta m = 0$ is satisfied. A scheme of these transitions is depicted in figure 4a. The PL emitted is highly stable and follows relaxation mechanisms between the excited and ground state which are spin-dependent, making the NV$^-$ defect initialize into $m_{gs} = 0$ by means of optical pumping, as will be seen in what follows. It is relevant to point out that the NV$^-$ system can decay from the optically excited state towards the ground state by two paths. The first one, it emits photons (a radiative path) and in the other one it

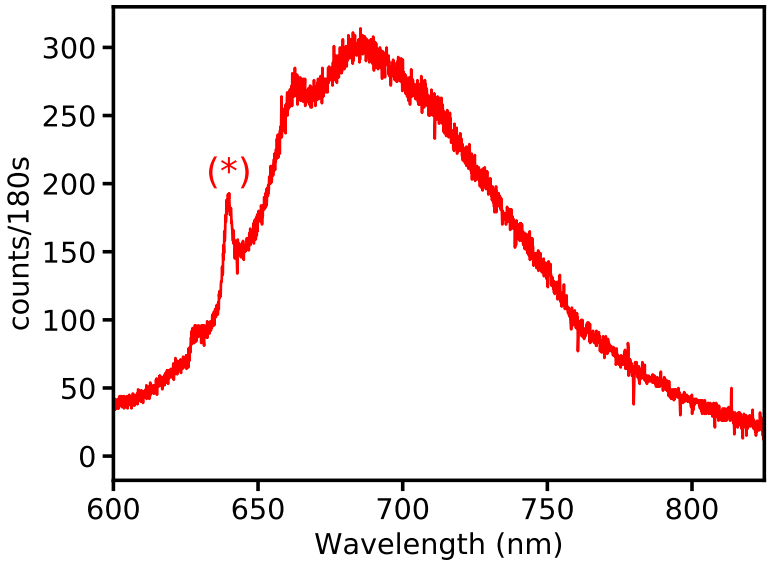

Figure 3: Photoluminescence spectrum of a single NV$^-$ defect in diamond measured under ambient conditions (T = 293 K) with its characteristic zero phonon line at 637 nm (*) and a wide phonon sideband from 600 nm to 800 nm (due to the coupling with crystalline lattice vibrations).

decays through a channel known as intersystem crossing (ISC) (figure 4a) that involves a spin singlet [60, 61]. This singlet level $m_s = 0$ is close in energy with the excited state, and spin-orbit induces triplet-singlet ISC [62]. Moreover, the singlet $m_s = 0$ plays an important role in the spin dynamics of the NV$^-$ defect. Actually, whereas the optical transitions between $m_{gs} \rightarrow m_{es}$ are spin-conserving, ISC transition $m_{es} \rightarrow m_s$ are strongly spin-selective to then decay preferentially towards the ground state sublevel $m_{gs} = 0$. As depicted in figure 4a, transition $m_{gs} = 0 \rightarrow m_{es} = 0$ results in a predominantly radiative decay (thick red arrow) while the transitions $m_{gs} = \pm 1 \rightarrow m_{es} = \pm 1$ decay radiatively with a smaller probability (thin red arrow). The latter transitions, however, have a higher probability to occur via ISC to a singlet intermediate spin state, $m_s = 0$, with a characteristically time $\lesssim 1$ ns and then to the ground state sublevel $m_{gs} = 0$ with an average time of 300 ns [62], without radiation emission. After a few optical cycles all population ends up in the ground spin sublevel $m_{gs} = 0$ and it is said that the NV$^-$ system was spin polarized by optical pumping. This spin dynamics is characteristic in this kind of system and allows to prepare it in an initialized and known state [63] giving a chance to develop protocols for quantum information processing [64]. Furthermore, as

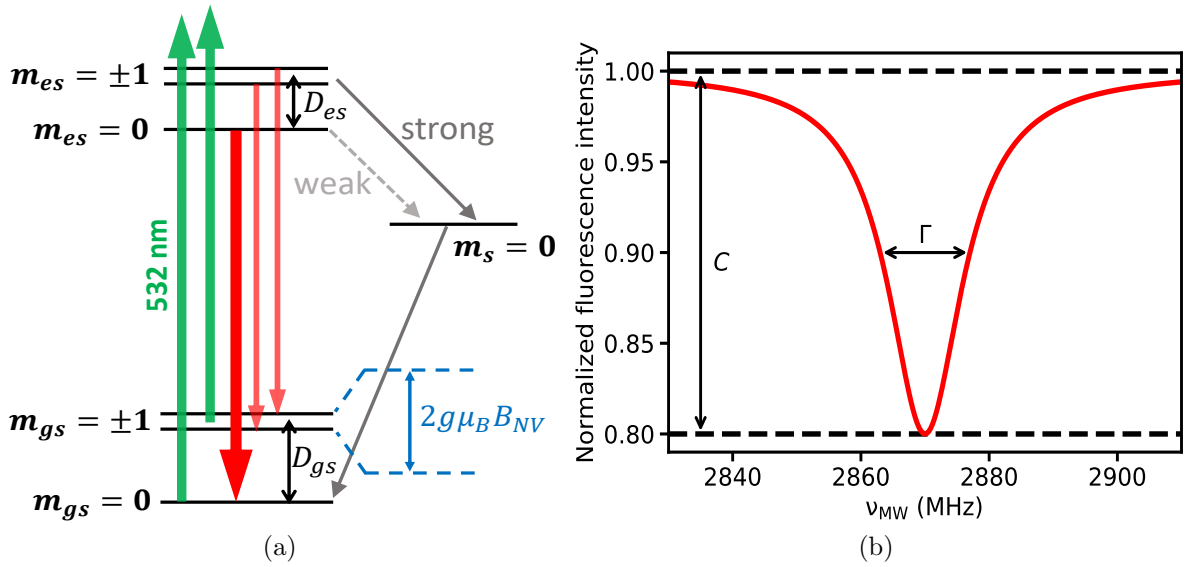

Figure 4: (a) Schematic energy level structure (not to scale) of the NV⁻ defect in diamond depicting its photophysics in the process of optical excitation (green arrow) and fluorescence emission (red arrows). Transitions between ground and excited states are predominantly spin conserving. Decay through intersystem crossing (ISC) gives rise to a spin polarization, switching from $m_s = \pm 1$ to $m_s = 0$ by means of a non-radiative path. (b) Normalized Optically Detected Magnetic Resonance (ODMR) simulated spectrum at zero external magnetic field indicating a dip centered in a typical resonance frequency of 2.87 GHz. C is the optical contrast and Γ is the linewidth of the spin transition of the NV⁻ defect magnetic dipole.

explained below, the fluorescence emission rate changes depending on the NV⁻ initial spin state. As result of this dependence ESR can be optically detected. In the experiments, sweeping microwave fields around the ESR frequency, when microwave frequency is in resonance with the $m_{gs} = 0 \rightarrow \pm 1$ transition, the $m_{gs} = \pm 1$ states are populated while continuously driving optical transitions it is leads to reduction in the intensity of the emitted fluorescence by the NV⁻ defect at approximately $C = 20\%$ as seen in figure 4b.

Extraordinary sensitivity and nanoscale resolution in presence of local magnetic fields is reached with the NV⁻ system [58, 65] even under ambient conditions [66]. This, because the effects of the magnetic field over the NV⁻ act as a perturbation, lifts the degeneracy of the $m_{gs} = \pm 1$ spin sublevels and spliting them by Zeeman effect. Besides, energy splitting $h\delta\nu$ is proportional to the projection of the magnetic field along the NV⁻ defect axis, given by $2g\mu_B B_{NV}$, as shown in the bottom of figure 4a. Here, g is the Landé factor, μ_B

is the Bohr magneton and B_{NV} is the magnetic field component along NV^- axis (further details on the Zeeman effect will be given on section 2.5). Thus, measurement of magnetic field can be performed just sensing the splitting between its $m_{gs} = \pm 1$ spin states [67, 68]. In the next section, a protocol will be presented, that allows to control the spin sublevels, which is frequently used in magnetometer experiments.

2.4 Coherent manipulation of the spin sublevels

Up to this point some important features about the NV^- defect in diamond were indicated and how it has being considered as a potential solid-state system to be used in magnetometry as well. However, these attributes can be exploited only by having access to the sublevels of the spin ground state. Thus, it is necessary to create a spin state manipulation protocol to take control of its spin dynamics [69, 70]. A powerful technique used for performing this type of control is the well-known Optically Detected Magnetic Resonance (ODMR) [71]. It is a technique which makes possible to drive spin transitions by resonant spin excitation and optical readout illuminating the quantum system and detecting its fluorescence simultaneously [72]. The principle of this technique will be used in the present experiments of magnetometry, being important for implementation on a protocol to carry out this task.

The protocol involves spin sublevels of the NV^- center, which, as previously, at thermal equilibrium are equally populated at room temperature, according to the Boltzmann distribution. By pumping continuously the NV^- defect with green light, population from the ground spin sublevels are promoted towards their corresponding excited spin sublevel. As described in the last section, after a few optical cycles the system ends up polarized as consequence of the re-orientation of the ground state spin in the $m_{gs} = 0$ state. Then, with an initialized system it can be possible to access and manipulate the ground state by means of microwave fields, driving transitions from $m_{gs} = 0$ to $m_{gs} = \pm 1$ spin sublevels. The sweep over a given frequency range leads to an ODMR spectrum that shows a drop in the intensity of the PL (figure 4b) emitted by the NV^- when frequency is in resonance

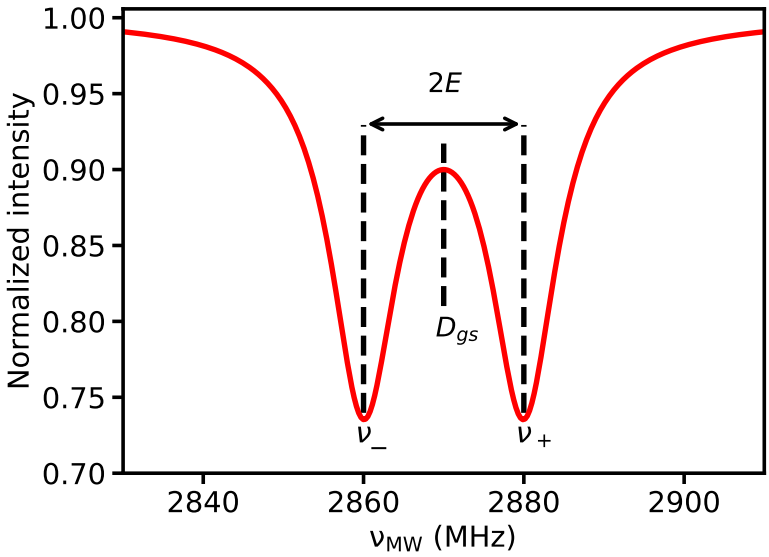

Figure 5: Typical ODMR spectrum depicting the two ESR frequencies ν_- and ν_+. D_{gs} is the average of the two resonance frequencies and the E parameter is defined as half of its difference in absolute value.

with the spin transition. This property is the key for magnetometry applications. When a external magnetic field is applied, in response two resonance peaks corresponding to transitions $m_{gs} = 0 \rightarrow -1$ and $m_{gs} = 0 \rightarrow +1$ are observed. A measure of the strength of applied magnetic field is given by a detection of the Zeeman splitting between the two resonance peaks (see figure 5). The next section describes the Hamiltonian of the NV⁻ defect and solves it as a method to measure magnetic fields.

2.5 Spin Hamiltonian of the NV⁻ defect

The ground state of the NV⁻ defect can be better understood studying its Hamiltonian. Since the NV⁻ defect involves two unpaired electrons there is an interaction between them known as spin-spin interaction, which exhibits a ZFS in the electronic ground state given by **S**·D·**S** [67]. **S** is the spin operator and D the tensor that describes the dipolar interaction. Considering the NV⁻ defect symmetry axis oriented along the z-direction (see figura 2a), the Hamiltonian due this interaction is given by [68]

$$H_{ZF} = hD_{gs}S_z^2 + hE(S_x^2 - S_y^2) \tag{2.1}$$

where h is the Planck's constant, D_{gs} e E are the ZFS parameters (see figure 5); S_x, S_y and S_z are the Pauli matrices. In this Hamiltonian, D_{gs} is the largest energy scale and sets the spin quantization axis parallel to the NV$^-$ symmetry axis direction. Furthermore, it is a constant parameter that separates $m_s = 0$ from the $m_s = \pm 1$ by $D_{gs} = 2.87$ GHz. The $E \neq 0$ parameter appears when the local axial symmetry is lost and the degeneracy is lifted due to surface strain present in NDs associated to the piezoelectric properties of the matrix and/or the presence of external electric field [55]. Diamonds with a weak strain present an $E \approx 100$ kHz, while in nanodiamonds where the mechanical strain is stronger the typical value of E is around a few MHz [68].

There is another term in the Hamiltonian that appears when the NV$^-$ defect is in the presence of an external magnetic field, inducing a change in the split energy of the $m_s = \pm 1$ spin sublevels by Zeeman effect. The Zeeman splitting is proportional to the magnitude of the applied magnetic field [77], such that by increasing the field magnitude the separation in energy between the spin sublevels increases as well. Thus, the interaction term between the NV$^-$ defect and the magnetic field can be written as

$$H_Z = g\mu_B \mathbf{B} \cdot \mathbf{S}. \tag{2.2}$$

Here, $\mathbf{B}$ is the external magnetic field. Then, neglecting the hyperfine interaction, the total Hamiltonian frequently found in the literature reads as

$$H = hD_{gs}S_z^2 + hE(S_x^2 - S_y^2) + g\mu_B \mathbf{B} \cdot \mathbf{S}. \tag{2.3}$$

The last term of the equation can be separated in its three spatial components and then the Hamiltonian can be rewritten as [68]

$$H = \overbrace{hD_{gs}S_z^2 + g\mu_B B_{NV} S_z}^{H_\parallel} + \overbrace{g\mu_B(B_x S_x + B_y S_y)}^{H_\perp} + hE(S_x^2 - S_y^2) \tag{2.4}$$

where it is typical to make $B_{NV} = B_z$. The term $H_\parallel$ involves the components of spin and magnetic field oriented along the NV$^-$ defect symmetry axis whereas $H_\perp$ involves the

transverse components. Thus, one can solve the Hamiltonian to find the ESR frequencies just introducing in the Hamiltonian the spin components in their matrix form. Since S_x, S_y and S_z are the components of the spin operator, they can be written as a function of the Pauli matrices as

$$S_x = \frac{1}{\sqrt{2}}\begin{pmatrix} 0 & 1 & 0 \\ 1 & 0 & 1 \\ 0 & 1 & 0 \end{pmatrix}, \qquad S_y = \frac{1}{\sqrt{2}}\begin{pmatrix} 0 & -i & 0 \\ i & 0 & -i \\ 0 & i & 0 \end{pmatrix}, \qquad S_z = \begin{pmatrix} 1 & 0 & 0 \\ 0 & 0 & 0 \\ 0 & 0 & -1 \end{pmatrix} \tag{2.5}$$

then,

$$B_x S_x + B_y S_y + B_z S_z = \begin{pmatrix} B_z & \frac{B_x - iB_y}{\sqrt{2}} & 0 \\ \frac{B_x + iB_y}{\sqrt{2}} & 0 & \frac{B_x - iB_y}{\sqrt{2}} \\ 0 & \frac{B_x + iB_y}{\sqrt{2}} & -B_z \end{pmatrix} \tag{2.6}$$

and

$$S_x^2 - S_y^2 = \begin{pmatrix} 0 & 0 & 1 \\ 0 & 0 & 0 \\ 1 & 0 & 0 \end{pmatrix} \tag{2.7}$$

replacing equations 2.6 and 2.7 in 2.4 one gets

$$\begin{aligned} H &= hD_{gs}\begin{pmatrix} 1 & 0 & 0 \\ 0 & 0 & 0 \\ 0 & 0 & 1 \end{pmatrix} + hE\begin{pmatrix} 0 & 0 & 1 \\ 0 & 0 & 0 \\ 1 & 0 & 0 \end{pmatrix} + g\mu_B \begin{pmatrix} B_z & \frac{B_x - iB_y}{\sqrt{2}} & 0 \\ \frac{B_x + iB_y}{\sqrt{2}} & 0 & \frac{B_x - iB_y}{\sqrt{2}} \\ 0 & \frac{B_x + iB_y}{\sqrt{2}} & -B_z \end{pmatrix} \\ &= \begin{pmatrix} hD_{gs} + g\mu_B B_z & \frac{g\mu_B}{\sqrt{2}}(B_x - iB_y) & hE \\ \frac{g\mu_B}{\sqrt{2}}(B_x + iB_y) & 0 & \frac{g\mu_B}{\sqrt{2}}(B_x - iB_y) \\ hE & \frac{g\mu_B}{\sqrt{2}}(B_x + iB_y) & hD_{gs} - g\mu_B B_z \end{pmatrix}. \end{aligned} \tag{2.8}$$

Considering that the NV$^-$ system is interacting with weak magnetic fields and that the magnetic field transverse component is much smaller than $hD_{gs}/g\mu_B \approx 100$ mT [68] (condition easily met in the experiments performed in this work, as shown ahead), the diagonal terms in the matrix become predominant. Thus, neglecting the B_x and B_y components of the magnetic field the equation 2.8 reads as

$$H = \begin{pmatrix} hD_{gs} + g\mu_B B_z & 0 & hE \\ 0 & 0 & 0 \\ hE & 0 & hD_{gs} - g\mu_B B_z \end{pmatrix}. \tag{2.9}$$

In this case, one determines the energy eigenvalues by solving the characteristic equation

$$\det(H - \epsilon I) = 0 \tag{2.10}$$

where ϵ represents the eigenvalues of H and I is the identity matrix. Replacing explicitly in the equation 2.10 one has the following

$$\left| \begin{pmatrix} hD_{gs} + g\mu_B B_z & 0 & hE \\ 0 & 0 & 0 \\ hE & 0 & hD_{gs} - g\mu_B B_z \end{pmatrix} - \epsilon \begin{pmatrix} 1 & 0 & 0 \\ 0 & 1 & 0 \\ 0 & 0 & 1 \end{pmatrix} \right| = 0 \tag{2.11}$$

then, two eigenvalues are found

$$\epsilon_\pm = hD_{gs} \pm \sqrt{(g\mu_B B_z)^2 + (hE)^2} = h\nu_\pm. \tag{2.12}$$

Here, $\nu_\pm$ are the ESR frequencies where $\pm$ indicate the corresponding spin state. Reminding again that the quantization axis is fixed by the NV$^-$ defect symmetry axis, the ESR frequencies are given by the following expression

$$\nu_\pm = D_{gs} \pm \sqrt{\left(\frac{g\mu_B B_z}{h}\right)^2 + E^2}. \tag{2.13}$$

The difference between both ESR frequencies gives us the total Zeeman splitting, $\delta\nu$

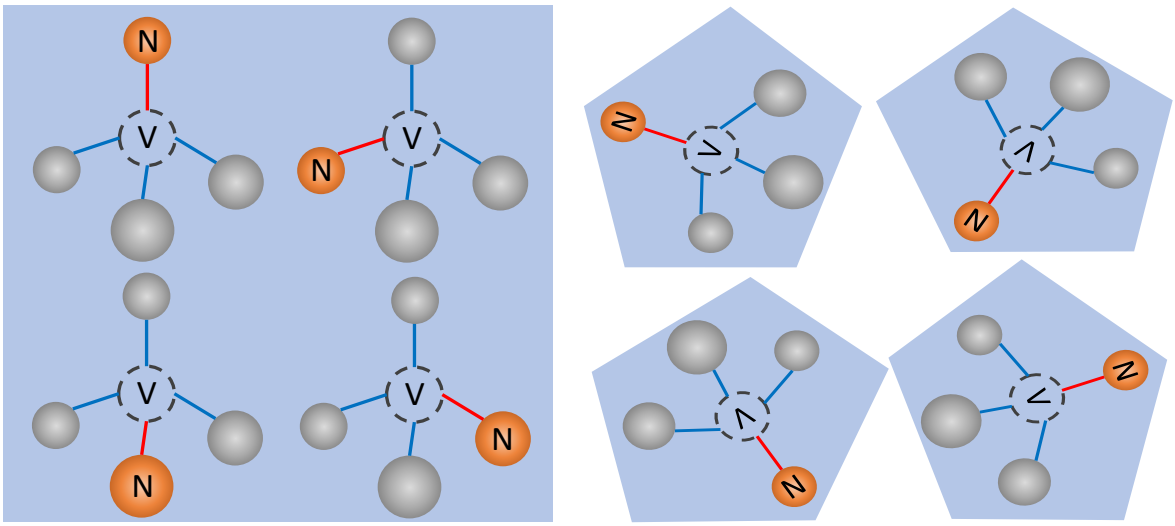

(a) (b)

Figure 6: (a) Illustration of the four possible orientations of the NV$^-$ symmetry axis in the crystalline structure of a bulk diamond. (b) Diamond nanocrystals containing a single NV$^-$ defect. In this case, the NV$^-$ symmetry axis can take all possible spacial orientations.

$$\delta\nu = 2\sqrt{\left(\frac{g\mu_B}{h}B_z\right)^2 + E^2}. \tag{2.14}$$

It is important to note that in both equations 2.13 and 2.14 the ZFS parameter E sets a limitation to detect Zeeman splitting. When $\frac{g\mu_B}{h}B_z \ll E$ the ESR frequencies are found as $\nu_\pm \approx D \pm E$, making the NV$^-$ defect insensitive to detect external magnetic fields in this regime. In order to overcome this inconvenient, a bias magnetic field $B_{bias} \gg \frac{hE}{g\mu_B}$ (in general a few militeslas) is generally used [75, 76].

All this treatment assumes magnetic fields oriented along the same direction of the NV$^-$ axis, otherwise the orientation of the NV$^-$ axis relative to the magnetic field must be determined. In the present work, nanodiamonds are spread on a surface by spin coating, randomly orienting their magnetic dipole moments. As the split of the Zeeman sublevels $m_{gs} = \pm 1$ is proportional to the magnetic field applied along to the magnetic dipole moment axis it is relevant measure its orientation to perform magnetometry experiments. Thus, two different methods were used to determine that orientation, which are described in the next section.

2.5.1 Determination of the NV$^-$ defect symmetry axis orientation

The use of NV$^-$ defects in NDs is increasing in different areas of science but particularly in magnetic sensing. The advantage of using them for this task is their nanoscopic size that allows to measure magnetic fields with nanoscale spatial resolution. Unlike bulk diamond, where the crystalline structure sets only four possible orientations for the NV defect symmetry axis, as shown in figure 6a, NDs with a single NV$^-$ defect present all possible orientations when they are randomly deposited over a surface (figure 6b) like what happens when using the spin coating technique for that. Then, if one wants to use a nanodiamond with a single NV$^-$ defect for performing nanomagnetometry, its magnetic dipole moment orientation must be determined. In order to do that, it will be necessary to realize a coordinate transformation from the laboratory reference frame (XYZ), in relation to which applied magnetic field is applied, to the coordinate system (xyz) in which the NV$^-$ magnetic dipole moment is conveniently oriented along the z direction. Applying a counterclockwise elemental rotation of the coordinate system XYZ by an angle φ around the fixed Z-axis followed by a rotation by θ around the Y-axis, as seen in figure 7a, it is possible to get such transformation. Figure 7b shows a projection of an external magnetic field B_{ext} over the NV$^-$ axes, which produces the separation in ESR energy by Zeeman effect. Thereby, the coordinate transformation allows us to rewrite B_z in function of the components of the magnetic field applied in the XYZ reference frame, as follows

$$\begin{pmatrix} B_x \\ B_y \\ B_z \end{pmatrix} = \begin{pmatrix} \cos\theta & 0 & \sin\theta \\ 0 & 1 & 0 \\ -\sin\theta & 0 & \cos\theta \end{pmatrix} \begin{pmatrix} \cos\varphi & -\sin\varphi & 0 \\ \sin\varphi & \cos\varphi & 0 \\ 0 & 0 & 1 \end{pmatrix} \begin{pmatrix} B_{\mathrm{X}} \\ B_{\mathrm{Y}} \\ B_{\mathrm{Z}} \end{pmatrix} \therefore$$

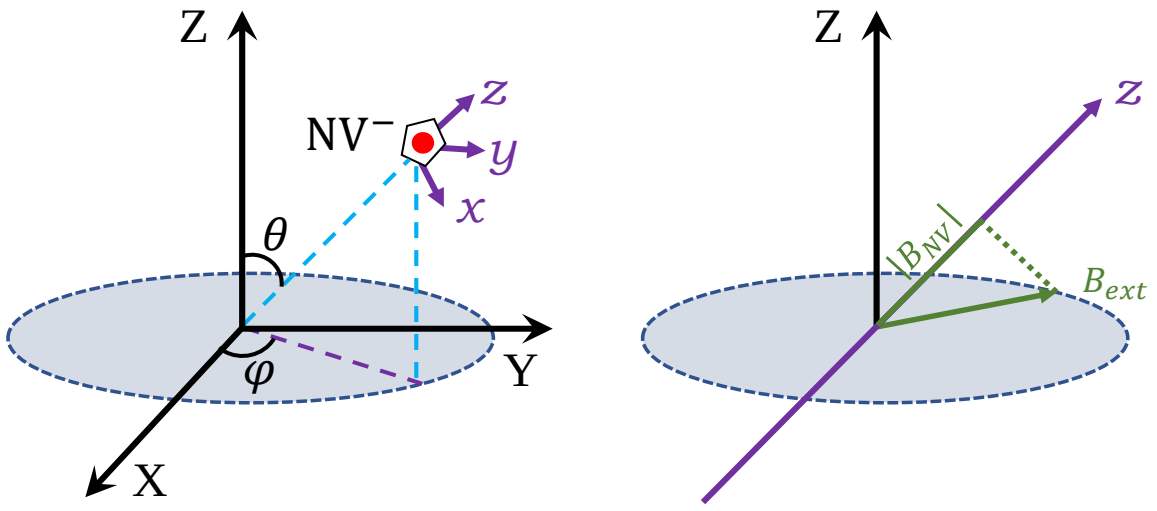

(a) (b)

Figure 7: (a) Definition of the NV⁻ defect magnetic dipole axis orientation angles in the nanodiamond reference frame *xyz* in relation to the laboratory reference frame XYZ. The NV⁻ defect magnetic dipole moment is oriented along the z axis. (b) Scheme depicting the projection of the external magnetic field on the dipole moment axis. This projection acts as a perturbation over the NV⁻ quantum states $m_s = \pm 1$ lifting their degeneracy by the Zeeman effect.

$$
\begin{aligned}
&= \begin{pmatrix} \cos\theta\cos\varphi & -\cos\theta\sin\varphi & \sin\theta \\ \sin\varphi & \cos\varphi & 0 \\ -\sin\theta\cos\varphi & \sin\theta\sin\varphi & \cos\theta \end{pmatrix} \begin{pmatrix} B_{\mathrm{X}} \\ B_{\mathrm{Y}} \\ B_{\mathrm{Z}} \end{pmatrix} \\
&= \begin{pmatrix} B_{\mathrm{X}}\cos\theta\cos\varphi - B_{\mathrm{Y}}\cos\theta\sin\varphi + B_{\mathrm{Z}}\sin\theta \\ B_{\mathrm{X}}\sin\varphi + B_{\mathrm{Y}}\cos\varphi \\ -B_{\mathrm{X}}\sin\theta\cos\varphi + B_{\mathrm{Y}}\sin\theta\sin\varphi + B_{\mathrm{Z}}\cos\theta \end{pmatrix}
\end{aligned}
\tag{2.15}
$$

considering that only the B_z component is able to cause the Zeeman split, then

$$
B_z = -B_{\mathrm{X}}\sin\theta\cos\varphi + B_{\mathrm{Y}}\sin\theta\sin\varphi + B_{\mathrm{Z}}\cos\theta \tag{2.16}
$$

Thus, equations 2.13 and 2.14 can be written as a function of the angular coordinates and spatial components of the magnetic field as

$$\nu_{\pm} = D \pm 2\sqrt{\left(\frac{g\mu_B(-B_{\mathrm{X}}\sin\theta\cos\varphi + B_{\mathrm{Y}}\sin\theta\sin\varphi + B_{\mathrm{Z}}\cos\theta)}{h}\right)^2 + E^2} \tag{2.17}$$

$$\delta\nu = 2\sqrt{\left(\frac{g\mu_B(-B_{\mathrm{X}}\sin\theta\cos\varphi + B_{\mathrm{Y}}\sin\theta\sin\varphi + B_{\mathrm{Z}}\cos\theta)}{h}\right)^2 + E^2} \tag{2.18}$$

One can restrict even more, for example by neglecting the component B_{Z} (for reasons that will get clear soon) to rewrite equations 2.17 and 2.18 as

$$\nu_{\pm} = D \pm \sqrt{\left(\frac{g\mu_B(-B_{\mathrm{X}}\sin\theta\cos\varphi + B_{\mathrm{Y}}\sin\theta\sin\varphi)}{h}\right)^2 + E^2} \tag{2.19}$$

$$\delta\nu = 2\sqrt{\left(\frac{g\mu_B(-B_{\mathrm{X}}\sin\theta\cos\varphi + B_{\mathrm{Y}}\sin\theta\sin\varphi}{h}\right)^2 + E^2} \tag{2.20}$$

These expressions are useful in the typical experimental situation of this Thesis, in which NDs are spread over a coverslip, because they offer the possibility to use two methods to determine the orientation of the NV$^-$ defect magnetic dipole moment.

The procedure of the first method consists of applying static magnetic fields in the X- and Y-directions independently and recording the respective Zeeman splittings. Thus, using equation 2.19 and invoking the symmetry of the splitting around the unperturbed resonance frequency one gets two equations with two variables (θ and φ), which are solved to determine the two magnetic dipole moment orientation angles.

In the second method, equation 2.20 is considered, which is useful when a magnetic field is applied with a constant magnitude but rotating in the XY-plane. By recording the Zeeman splitting at every rotated angle it is possible to determine both θ and φ angles.

Figure 8 depicts a simulation that results from the first method: Zeeman splitting in response of an external magnetic field applied for different angles relatives to the NV$^-$ magnetic dipole moment orientation. As can be seen, as the angle approaches to $\theta = 90°$

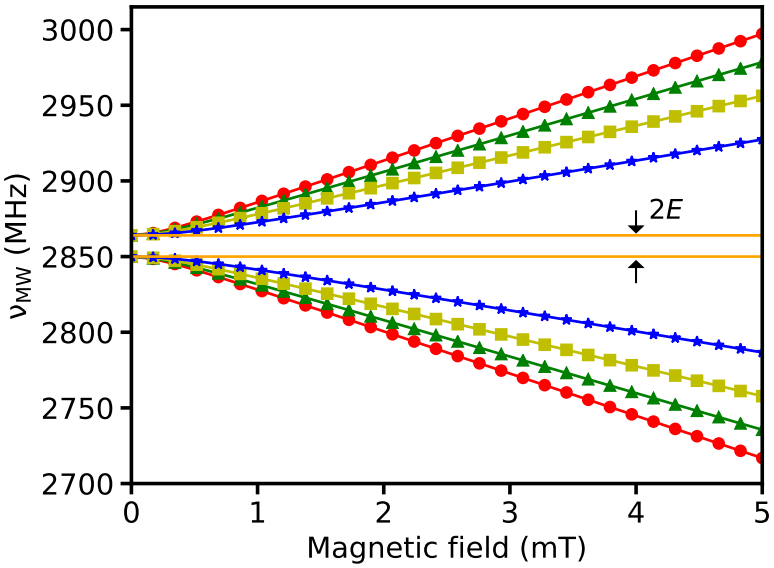

Figure 8: ESR curves (considering $E = 7$ MHz) in function of the magnetic field amplitude applied in direction $\theta = 0°$, $\theta = 30°$, $\theta = 45°$, $\theta = 60°$ and $\theta = 90°$ (circle, triangle, square, star and line, respectively) relative to the NV$^-$ magnetic dipole moment direction.

the interaction between the NV$^-$ defect magnetic dipole moment and the magnetic field (see equation 2.2) gets negligible, evidencing only the ZFS parameter $2E$, while for $\theta = 0°$, when the magnetic field is positioned parallel with the NV$^-$ magnetic dipole moment axis, a maximum Zeeman splitting is observed.

For the second procedure, following the theoretical model in figure 9a, an oscillatory behavior of the Zeeman splitting is verified, when a magnetic field with fixed magnitude (5 mT) is rotated by an angle Φ over the XY-plane. Here the fixed magnitude is related with the B_x and B_y components as a classical vector $|B| = \sqrt{B_x^2 + B_y^2}$. Thus, setting the θ angle one observes a shift in phase of the Zeeman splitting for different φ azimuthal angle values. Moreover, as can be seen, the minimal $\delta\nu$ value is limited to the ZFS $2E$, as expected. On the other hand, figure 9b shows the results for fixing the azimuthal angle φ while the polar angle θ takes different values, evidencing a reduction in the splitting amplitude when it is approached to form 90° degrees with the NV$^-$ axis. In this case, projection of the applied magnetic field along the magnetic dipole moment vanishes, making null the Zeeman interaction term $\mathbf{B} \cdot \mathbf{S}$ in the Hamiltonian, which in turn is reflected in a zero splitting of the $m_s = \pm 1$ states due to the external magnetic field but keeping the ZFS $2E$

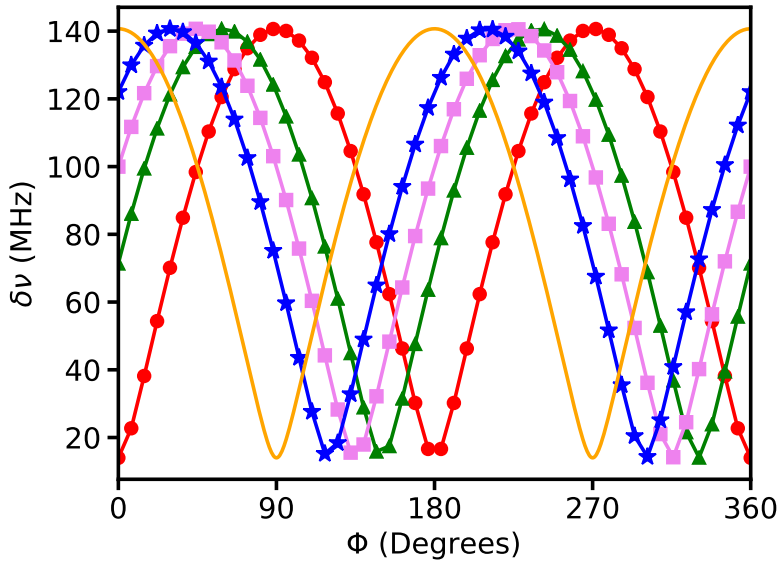

(a)

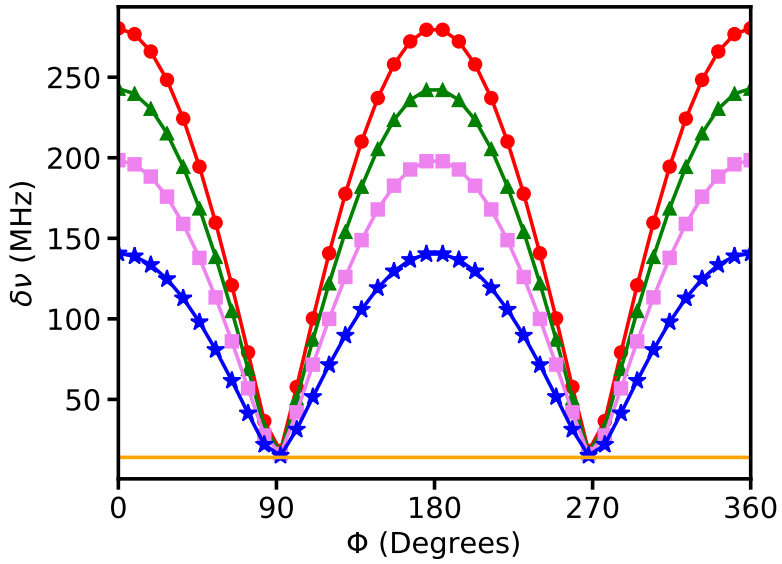

(b)

Figure 9: (a) Sinusoidal behavior of the Zeeman splitting $\delta\nu$ when a variation of the Φ angle occurs due to the rotation of the applied magnetic field, in the reference frame XYZ. The parameter $E = 7$ MHz and a magnetic field magnitude of 5 mT were used. For a fixed $\theta = 30°$ it can be observed a phase shift in the sine curve for $\varphi = 0°$, $\varphi = 30°$, $\varphi = 45°$, $\varphi = 60°$ and $\varphi = 90°$ (line, star, square, triangle and circle, respectively). Note that for $\varphi = 90°$ split is not evidenced maintaining only the ZFE E. (b) Variation in the splitting amplitude is depicted when $\varphi = 0°$ is fixed and θ varies for $\theta = 0°$, $\theta = 30°$, $\theta = 45°$, $\theta = 60°$ and $\theta = 90°$ (line, star, square, triangle and circle, respectively). In the particular case $\theta = 0°$, projection of magnetic field on the dipole moment axis disappears neglecting the Zeeman splitting.

as in the previous case. The experimental implementation of both approaches and the corresponding results will be discussed in section 4.1.

2.6 Magnetometry with single NV$^-$ defects

As was mentioned in section 2.3, the NV$^-$ defect has intrinsic properties that allow an immediate response when interacting with a magnetic field, and this is why magnetometry with NV$^-$ defects in diamond is becoming a common technique for magnetic field sensing. As a point defect, it can be localized in a diamond matrix with a nanometer length scale. Thus, a NV$^-$ defect in ND can achieve nanometer scale spatial resolution. Moreover, unlike other magnetic sensors with high sensitivity which require cryogenic temperatures, the NV$^-$ defect exhibits its magnetic properties at room temperature [58,65,66,70,78] and due its long coherence time sensitive magnetometry can be achieved as well. For NV$^-$-based magnetometers are implemented a few magnetic fields sensing schemes, between the well known are the DC and AC schemes, which will be briefly discussed in what follows.

2.6.1 DC sensing scheme: ODMR sequence

This scheme takes advantage of the Zeeman splitting shown as an immediate response of the paramagnetic ground state of the NV$^-$ defect when interacts with magnetic fields. Thus, monitoring one of the two ESR frequencies in the ODMR spectrum is the simplest method for measuring magnetic fields. As seen in figure 10, the ODMR scheme consists of polarizing the NV$^-$ state to $m_{gs} = 0$ by optical excitation. Then by applying a MW field it is possible to drive spin transitions between $m_{gs} = 0$ and $m_{gs} = +1(-1)$ and detect them by fluorescence intensity measurement. In order to perform magnetometry, it is necessary to take into account the sensitivity of the system, which will be affected, among other factors, by photon shot-noise introduced by the photodiodes used to perform the readout protocols and that are present in the NV$^-$ magnetometry schemes. Thus, it is important to determine the sensitivity of the magnetometer to know the smallest magnetic field magnitude that can be measured by it (a “large” sensitivity means the system can

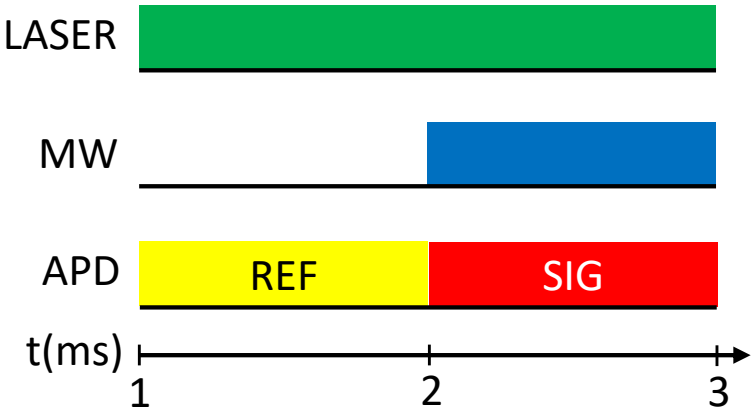

Figure 10: Scheme depicting the ODMR sequence. CW green laser is shining constantly to polarize the system in $m_{gs} = 0$. The APD collects the reference light during the first half of the sequence. Then, during the other half the MW is ON and the fluorescence signal is recorded by the same APD.

measure a "very small" magnetic field amplitude). This can be understood by considering the following: NV⁻-based magnetometers involve the spin states of the defect and its operation is carried out by ODMR. Coupling of the total spin angular momentum, **S**, with an applied magnetic field and optimization in the optical detection efficiency contributes to increasing the sensitivity of this kind of magnetometers. Detection of magnetic fields is performed monitoring the ESR frequency through its fluorescence that depends on the microwave field frequency for which a Lorentzian profile is commonly chosen

$$I = I_0 \left(1 - C \frac{(\Gamma/2)^2}{(\nu - \nu_0)^2 + (\Gamma/2)^2}\right) \tag{2.21}$$

In equation 2.21 I_0 is the photon count rate in the non-saturated regime and with the MW frequency far from the ESR; C is defined as the optical contrast or 1 minus the quotient of the total number of photons collected in resonance with the electron spin transition divided by the total number of photons out of resonance; ν_0 the ESR central frequency and Γ its full width at half maximum. Then, the PL signal, $S(B)$, acquired during an interval of time Δt, introducing the photon shot-noise limited photon measurement, is given by [79]

$$S(B) = I(B)\Delta t \pm \sqrt{I(B)\Delta t} \tag{2.22}$$

Assuming an infinitesimal variation of the magnetic field, a change can be detected in the fluorescence signal as

$$\begin{aligned} \delta S &= \left(\frac{\partial S}{\partial B}\right)\delta B \\ &= \left(\frac{\partial I}{\partial B}\right)\Delta t \delta B \end{aligned} \tag{2.23}$$

Then, the expression for the signal-to-noise ratio can be written by

$$SNR = \frac{\delta S}{\sqrt{I(B)\Delta t}} = \frac{\left(\frac{\partial I}{\partial B}\right)}{\sqrt{I(B)\Delta t}}\Delta t \delta B \tag{2.24}$$

Thus, it is possible to determine a sensitivity to measure magnetic fields, which is defined as [80]

$$\eta = \delta B\sqrt{\Delta t} \tag{2.25}$$

The last expression is directly related to the smallest variation of the magnetic field δB and to the square root integration time Δt with units expressed in T$\sqrt{\text{Hz}}$. A small η corresponds to a more sensitivity magnetometer implicating that a lower magnetic field can be detected. Thus, one is interested in the minimum detectable magnetic field amplitude. Assuming $SNR = 2$ one can rewrite the equation (2.25) as

$$\eta = \frac{2\sqrt{I(B)}}{(\partial I/\partial B)} \approx \frac{h}{g\mu_B}\frac{2\sqrt{I_0}}{(\partial I/\partial \nu)_{max}} \tag{2.26}$$

where $\sqrt{I(B)} \approx \sqrt{I_0}$ to simplify the result. Besides, the derivative $\partial I/\partial \nu$ must be maximum to get maximum sensitivity. As in the present work it is assumed a Lorentzian ESR profile, its maximum derivative is written as

$$\left(\frac{\partial I}{\partial \nu}\right)_{max} = \frac{3\sqrt{3}}{4}\frac{I_0 C}{\Gamma} \tag{2.27}$$

by replacing (2.27) in (2.26) and then in (2.25), it is possible to find an expression for sensitivity in terms of experimentally measurable parameters as:

$$\eta = \frac{4}{3\sqrt{3}} \frac{h}{g\mu_B} \frac{2\Gamma}{C\sqrt{I_0}}. \tag{2.28}$$

Thus, from the last expression, the sensitivity can be enhanced using appropriate parameters for the optical pumping, increasing I_0 through improved the PL collection efficiency. Besides, how the linewidth is affected by radiation intensity, reducing the microwave power the ESR linewidth Γ is reduced.

Various works have been implemented following the DC scheme and their sensitivities were measured. For example, Schoenfeld and Harneit [36] performed realtime measurements of DC and AC magnetic fields with frequencies up to 8.3 Hz. To do that, they used two microwave sources which were modulated by a rectangular wave pattern created to alternately switch them. For a fixed microwave center frequency in the resonance spin transition, when an external magnetic field is enough to shift the ESR frequency a change in the PL signal is evidenced. In their approach, they could follow the resonance position allowing them to measure the external magnetic field in realtime continuously adjusting and recording the microwave frequency value using this signal. With this method, they achieved a sensitivity of 1 $\mu\mathrm{T}/\sqrt{\mathrm{Hz}}$.

L. Rondin *et al.* [68] demonstrated a nanoscale magnetic field mapping using a single nanodiamond placed at the apex of an atomic force microscope tip. Applying two slightly different microwave frequencies and recording the PL difference as an error signal, they can use the lock-in method to track the ESR frequency single NV$^-$ defect while scanning a magnetic sample. Using these approaches, a mapping of the magnetic field distribution of a commercial magnetic hard disk is done. The system operated with a $\delta B = 27\mu\mathrm{T}$, which combined with an acquisition time per pixel of $\Delta t = 10$ ms gives an experimental field sensitivity of $\eta = 9$ $\mu\mathrm{T}$ $/\sqrt{\mathrm{Hz}}$.

As seen in these two examples, the DC scheme is the simplest method in the implementation of a NV$^-$-based magnetometer. However, from equation 2.28 one can observe that one limitation of the method is related to the ESR linewidth, Γ, which in turn is proportional to the inverse of the dephasing time as $\Gamma \sim 1/T_2^*$. For diamond isotopically purified with

carbon-12 (^{12}C) atoms during a bulky sample growth, the concentration of carbon-13 (^{13}C) can be reduced to less than 0.01 % [74], reducing the content of nuclear spins associated with ^{13}C that limit the coherence time. Being possible increase T_2^* and subsequently reduce Γ. On the other hands, the MW field and a spin readout laser contribute to broadening the linewidth being both indispensable in the process of spin manipulation and PL readout. A way to reduce Γ involves separating these radiation fields, which can be achieved via Ramsey sequences. The methods explained below will serve as a complement to have a broader background, but the experiments related to these approaches will not be carried out in the present work.

2.6.2 DC sensing scheme: Ramsey sequence

In this DC scheme, the Ramsey sequence is used to avoid the interaction of the radiation fields with the NV$^-$ spin dephasing, allowing to access T_2^* and reducing the linewidth broadening. The Ramsey sequence (see figure 11) consists of simple steps, beginning with the polarization of the NV$^-$ spin in the $m_{gs} = 0$ state. Then, a MW $\pi/2$ pulse rotates the NV$^-$ electron spin to a coherent superposition of the $m_{gs} = 0$ and $m_{gs} = 1$ ($m_{gs} = -1$) states interacting only with the external magnetic field applied accumulating a phase $\phi = 2\pi\gamma B\tau$ (where γ is the gyromagnetic ratio of the electron spin) with respect to $m_{gs} = 0$. The characteristics of the $\pi/2$ pulse (temporal width for a used MW power) can be determined by means of previously performed Rabi oscillation experiments [82]. Then, the spin is free from any radiation fields during a time τ after which another MW $\pi/2$ pulse projects the NV$^-$ electron spin back again to the $m_{gs} = 0$. Thus, measuring the accumulated phase ϕ one can extract the magnetic field magnitude applied.

Magnetic field sensitivity is improved by maximizing the phase ϕ which implies increasing the precession time τ. To estimate the sensitivity produced by this method, one can model the PL signal, S, taking into account the average of photons as follows: defining a as the number of photons collected in the absence of an external magnetic field and b the number of collected photons when there is a phase accumulation of $\phi = \pi$ during the precession time τ. In this case, the average of the photon numbers collected is $(a + b)/2$. When

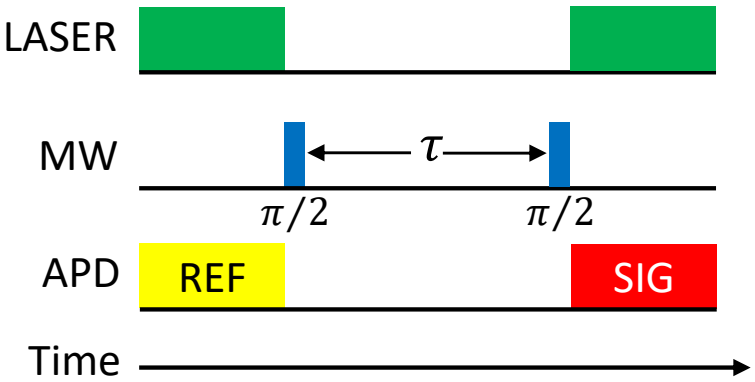

Figure 11: Pulse sequence employed for the Ramsey scheme. Laser ON shining to initialize the NV$^-$ defect in $m_{gs} = 0$. Subsequently a $\pi/2$ pulse prepares the spin into a superposition of the $m_{gs} = 0$ and $m_{gs} = +1$ ($m_{gs} = -1$) states to then decay freely during a time τ. Finally, another $\pi/2$ pulse is applied and the signal is readout by means of its fluorescence.

an external magnetic field B is interacting with the NV$^-$ spin, the signal S is described in function of the phase accumulation during a dephasing time τ, which can be roughly written as [58, 83]

$$S = \frac{(a+b)}{2} + \frac{(a-b)}{2}\cos(2\pi\gamma B\tau) \tag{2.29}$$

Considering the last equation, one can obtain an expression for the sensitivity η_R of a magnetometer which uses the Ramsey scheme to measure the magnetic field. As in the DC scheme, the uncertainty of δS is related directly proportional with the uncertainty to measure magnetic field δB times the slope

$$\delta S = \left(\frac{\partial S}{\partial B}\right)\delta B. \tag{2.30}$$

From the last equation, one can see that the smallest variation of the magnetic field can be achieved at a maximum slope. Thus, δB is written as

$$\delta B = \frac{\delta S}{\left(\frac{\partial S}{\partial B}\right)_{max}} \tag{2.31}$$

where the maximum slope is obtained deriving the equation 2.29 to get

$$\begin{aligned}\left(\frac{\partial S}{\partial B}\right)_{max} &= 2\pi\gamma\tau\frac{(a-b)}{2} \\ &= 2\pi\gamma\tau\left(\frac{a-b}{a+b}\right)\left(\frac{a+b}{2}\right) \\ &= 2\pi\gamma\tau C_R I_0 t_L \end{aligned} \tag{2.32}$$

where $C_R = (a-b)/(a+b)$ is the measurement contrast and the collected photons during a time t_L (readout laser pulse duration) is expressed as $(a+b)/2 = I_0 t_L$. Moreover, considering that the uncertainty of the signal S is dominated by photon shot noise, equation 2.31 be rewritten as

$$\delta B = \frac{\sqrt{I_0 t_L}}{2\pi\gamma\tau C_R I_0 t_L}. \tag{2.33}$$

Then, the sensitivity η_R in the Ramsey scheme is

$$\begin{aligned}\eta_R &= \frac{\sqrt{I_0 t_L}}{2\pi\gamma\tau C_R I_0 t_L}\sqrt{\tau} \\ &= \frac{\hbar}{g\mu_B}\frac{1}{C_R\sqrt{I_0 t_L}}\frac{1}{\sqrt{\tau}}. \end{aligned} \tag{2.34}$$

If the pulse sequence uses an optimized time interval $\tau \approx T_2^*$ [68] the previous equation becomes

$$\begin{aligned}\eta_R &= \frac{\sqrt{I_0 t_L}}{2\pi\gamma\tau C_R I_0 t_L}\sqrt{\tau} \\ &= \frac{\hbar}{g\mu_B}\frac{1}{C_R\sqrt{I_0 t_L}}\frac{1}{\sqrt{T_2^*}}. \end{aligned} \tag{2.35}$$

Magnetic field sensitivity using Ramsey scheme is analyzed theoretically in a few papers, such as [65, 81]. Based on this method, the DC field sensitivity from a single NV$^-$ center can be as high as $\eta_R = 1\ \mu\text{T}/\sqrt{\text{Hz}}$ for $T_2^* = 1\ \mu$s, which is what was typically achieved in the present setup for the NDs used in this work [82]. The dephasing time is the limitation of this method, but can be improved using ultra-pure diamond reaching T_2^* as long as 100 μs, leading to magnetic field sensitivities about $\eta_R = 40\ \text{nT}/\sqrt{\text{Hz}}$. In order to circumvent

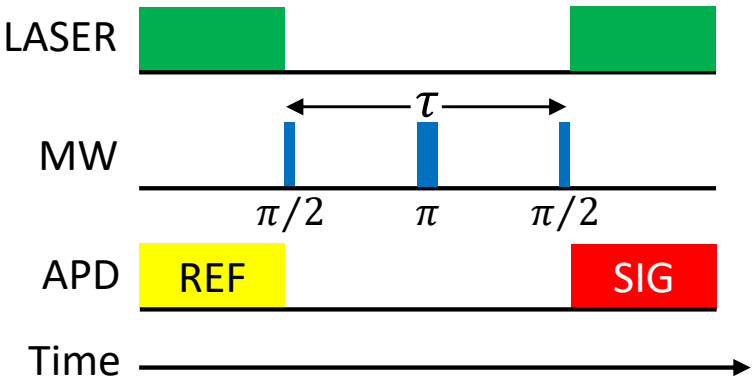

Figure 12: Scheme depicting the Hahn echo pulse sequence. The green laser is pumping the system to polarize the spin in $m_{gs} = 0$. Afterward, a $\pi/2$ pulse place the spin in a coherent superposition and immediately after the magnetic dipole moment precess freely during a time $\tau/2$. Then, the spin is flipped by a π pulse and let evolve during a time $\tau/2$ again and finally another $\pi/2$ pulse is applied and the signal is measured.

this limitation given by the inhomogeneous dephasing time, the Hahn echo sequence can be applied, as detailed in the next section.

2.6.3 AC sensing scheme: Hahn echo sequence

This method is a more complex spin manipulation scheme, which avoids the inhomogeneous spin-dephasing and prolongs effectively the NV$^-$ spin coherence to T_2 homogeneous time [20]. By Hahn echo dynamical decoupling protocol one can improve the sensitivity to magnetic field measurements. The spin echo pulse sequence consists of the Ramsey sequence but using an extra π-pulse in the middle of the sequence. This additional pulse flips the sign of accumulated phase during the free precession time resulting in the cancellation of DC and low frequency magnetic field. When the pulse duration matches the period of the AC magnetic field, however, the phase survives and continues to be accumulated. As a result, this scheme is useful only for detecting AC magnetic fields and its sensitivity is related to the pulse sequence duration. As in the Ramsey scheme, the PL signal oscillates as a function of the accumulate phase during its free precession time τ between a (corresponding to $\phi = 0$) and b (corresponding to $\phi = \pi$) [83]

$$S = \frac{(a+b)}{2} + \frac{(a-b)}{2}\cos(4\gamma B\tau) \tag{2.36}$$

By adding a π MW pulse in the middle of the Ramsey sequence (as seen in figure 12), the Hahn echo sequence removes the effect of environmental perturbations [65]. Thus, considering a signal field $b(t) = B\sin(2\pi f_{ac}t - \phi_0)$ (where f_{ac} is the magnetic field frequency) oscillating in phase with the pulse sequence produces an accumulated net phase ϕ in the process of free precession. π-pulse occurs at $t = \tau/2$ such that the accumulated phase ϕ is given by

$$\begin{aligned} \phi &= \int_0^{\tau/2} 2\pi\gamma b(t)dt - \int_{\tau/2}^{\tau} 2\pi\gamma b(t)dt \\ &= 4\pi\gamma B\int_0^{\tau/2} \sin(2\pi f_{ac}t - \phi_0)dt \\ &= 4\gamma B\tau\cos(\phi_0) \end{aligned} \tag{2.37}$$

For an optimal situation one can consider an accumulated phase $\phi_0 = 0$ [65] the net phase becoming in $\phi = 4\gamma B\tau$. Thus, the sensitivity to magnetic field measurements is optimized.

Uncertainty in the signal δS as in the DC sensing scheme is related directly proportional to the uncertainty in the measure of the field δB by the slope

$$\delta S = \frac{\partial S}{\partial B}\delta B. \tag{2.38}$$

For small changes in the magnetic field measurements, one has to measure the maximum slope

$$\begin{aligned} \left(\frac{\partial S}{\partial B}\right)_{max} &= 4\gamma\tau\frac{(a-b)}{2} \\ &= 4\gamma\tau\frac{(a-b)}{(a+b)}\frac{(a+b)}{2} \\ &= 4\gamma\tau C_{HE}I_0 t_L. \end{aligned} \tag{2.39}$$

Then, as the uncertainty in the signal is dominated by photon shot noise one can approximate $\delta S \approx \sqrt{I_0 t_L}$. Thus,

$$\delta B = \frac{1}{4\gamma\tau C_{HE}\sqrt{I_0 t_L}}. \tag{2.40}$$

As a result the sensitivity η_{HE} of the Hahn echo scheme is given by

$$\eta_{HE} = \frac{1}{4\gamma\tau C_{HE}\sqrt{I_0 t_L}}\sqrt{\tau}. \tag{2.41}$$

In essence, this scheme improves the sensitivity because it allows extending τ from the limit set by T_2^* up to value T_2. Thus, equation 2.41 is expressed as

$$\eta_{HE} = \frac{\pi}{2}\frac{\hbar}{g\mu_B C_{HE}\sqrt{I_0 t_L}}\frac{1}{\sqrt{\mathrm{T_2}}}. \tag{2.42}$$

The latter expression is related to the equation 2.35 by means of the following expression

$$\eta_{HE} = \eta_R\sqrt{\frac{\mathrm{T_2^*}}{\mathrm{T_2}}}. \tag{2.43}$$

The AC field sensitivity to magnetometer based on a single NV$^-$ defect in diamond can be as high as $\eta_{HE} \sim 1$ nT / $\sqrt{\mathrm{Hz}}$ for $\mathrm{T_2} \sim 1$ ms [65].

Various papers were published up to date using this approach. P. Maletinsky *et al.* [84] for example, show an alternative method to improve the sensitivity of scanning NV$^-$ magnetometers. This method is similar to the AFM technique but this time replacing the AFM tip by a scheme based on a monolithic diamond nanopillar containing a single defect. The high quality of diamond used for the nanopillar fabrication allows high coherence time. Besides, it is advantageous to use nanopillar since it behaves as an optical wave-guide of the NV$^-$ fluorescence. Thus, the long coherence time combined with the high collection efficiency resulting in an excellent magnetic field sensitivity. The Hahn echo spin coherence time achieved in the Maletinsky work was of $\mathrm{T_2} = 74.8$ μs achieving a maximal sensitivity of 56 nT/ $\sqrt{\mathrm{Hz}}$ for an AC magnetic field at a frequency of 33 kHz.

Maze *et al.* [85] demonstrated nanoscale magnetic sensing using impurities of NV$^-$ defects in ultrapure diamond. The key feature of the demonstrated sensor is that NV$^-$ defects

in bulk diamonds or as diamond nanocrystal (30 nm) can be directly located at $\sim$ 10 nm from the surface of the diamond. Since the magnetic field of an electron spin at this distance is roughly in the microstesla range, it is easy to detect it [58]. The echo signal measured in this work was of $T_2 \sim 4$ μs. Thus, magnetic field sensing using a diamond nanocrystal at a frequency of 380 kHz can be demonstrated reaching a sensitivity of ~ 0.5 $\mu T/\sqrt{Hz}$.

It is important to note that for use the Hahn echo scheme the AC magnetic field with amplitude B and frequency ν must be properly phased with respect to the microwave pulse. When the duration of the Hanh echo sequence τ is $\sim 1/\nu$ the accumulated phase of the electronic spin is proportional to B.

These schemes are commonly found in the literature but certainly, other ones exist that are more complicated such as the published in [86, 87], that requires a complex pulse sequence implementation and that inclusive demands more sophisticated equipment. Sometimes, the lack of all these tools makes the laboratory research difficult, so it was thought the implementation of a system able to employ the simplest protocol to achieve magnetic field measurements involving reasonable sensitivity with the possibility to use it in the real world conditions. This approach will be demonstrated in the next chapter.

Chapter 3

Setup implementation

This chapter is dedicated to explaining the procedural details used in the present work as the application of the confocal microscopy technique and its operation. Besides, it will be described how every single part of the experimental setup was built, as the case of the coils used to generate magnetic fields, for example. This chapter will be concluded with the design and implementation of a home-built magnetometer, the aim of this work.

3.1 Home-made inverted probe scanning confocal microscope

The spectroscopic study of single quantum emitters is a challenge due to the difficulty to detect them because of their low brightness in comparison with the background light and noise caused by spurious light scattered from their neighbor region. In order to perform detection of single NV^- defects, a home-made inverted confocal microscope was built to acquire images with high spatial resolution [82]. With this optical imaging technique, it is feasible to increase the optical resolution and contrast, which would be impossible to get with standard microscopes. The technique uses a pinhole as a spatial filter that blocks out of focus light resulting in sharper images. The pinhole is confocal to the focal plane, as seen in figure 13a. Hence, the fluorescence light coming from the ND illuminated in the focal plane is allowed to pass and the residual light from other regions is blocked (grey

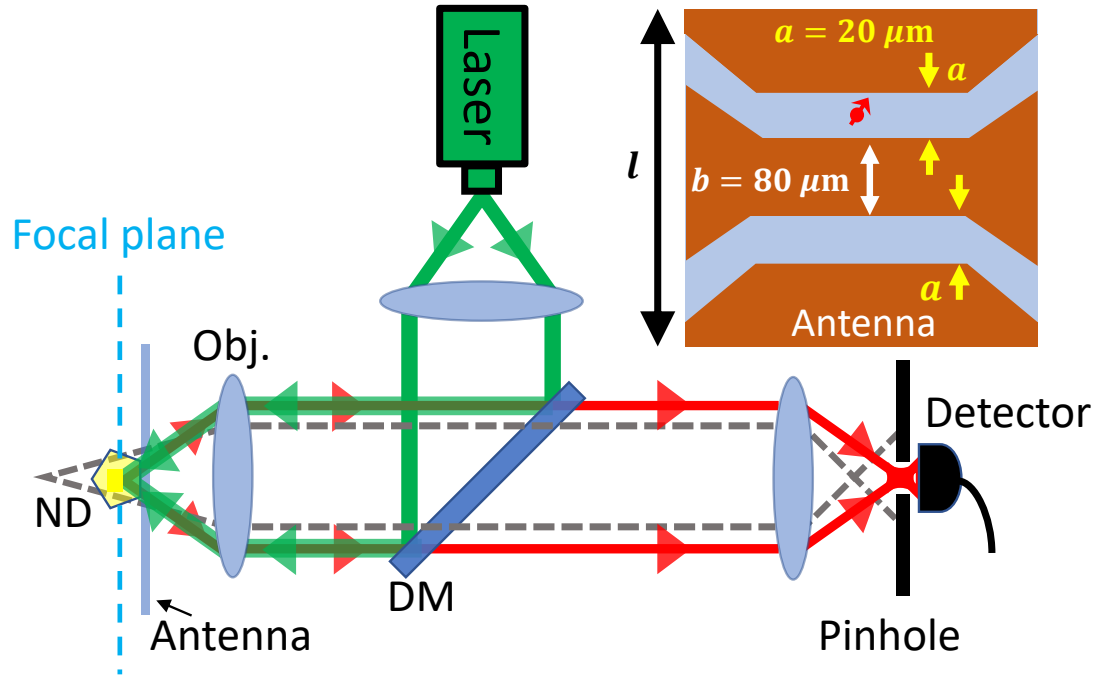

(a)

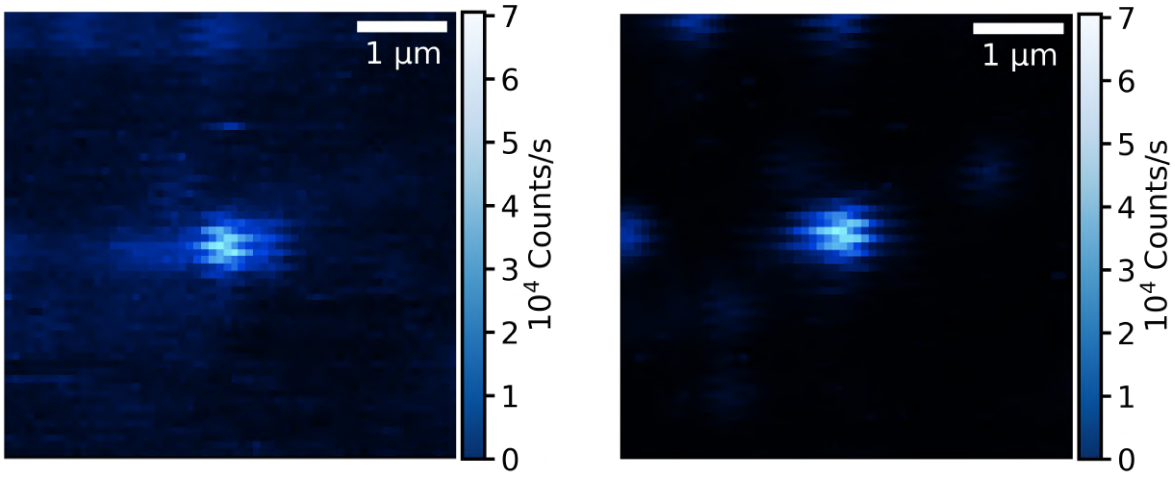

(b) (c)

Figure 13: (a) Scheme depicting the right focus position allowing the light coming from the focal plane to pass through the pinhole and then be detected. Top right, a top view scheme of an square MW antenna ($l = 18$ mm) made by photolithography technique (dimensions are not scale) on a glass coverslip. The red dot represents the NV^- defect (on the glass, the light blue region) and the red arrow its magnetic dipole moment. The brown part of the MW antenna is the conductor material deposited on the glass. (b) and (c) Scanning producing fluorescence images over a region of the antenna showing the standard and confocal microscopy modes respectively.

dashed lines in figure 13a). Also, it is possible to realize a scan over a micrometric region using a XY-piezo scanner. Thus, the light coming from the illuminated region, where the sample is deposited, forms an image as shown in figures 13b and 13c, in standard and confocal modes respectively. As can be seen, the confocal mode allows to observing an image with a slight improvement in sharpness where even is possible to see other particles in the nearby regions, which is difficult in the standard mode. In the subsection, the experimental apparatus mounted in the laboratory is described. The setup includes this technique and other implementations that make the magnetometry experiments possible.

3.1.1 Experimental apparatus

The experimental apparatus needs to be able to detect individual NDs containing a single NV^- defect. For that purpose, a Hanbury-Brown and Twiss (HBT) interferometer was built, allowing to verify the single photon characteristic of the PL emitted by the NDs observing the second order correlation function behavior. The observation of $g^{(2)}(0) < 0.5$ is a typical characteristic from single photon sources [89, 90]. Furthermore, as single NDs are spin-coated on a coverslip, where a MW antenna (see figure 13a) for performing ODMR is lithographically deposited, the orientation of the NV^- defect magnetic dipoles get randomly oriented in space. Since the magnetometer to be built measures the component of the external magnetic field along the NV^- magnetic dipole moment, it is necessary to determine the symmetry axis orientation of the NV^- defect chosen relative to the reference frame for performing magnetometry. In that sense, the setup built in the laboratory must have all the necessary features to carry out the mentioned tasks.

Most measurements presented in this thesis are related to optical excitation on the NDs sample and detection of their fluorescence. To carry them out, single nanoparticle spectroscopy was performed with a home-made inverted scanning probe optical confocal microscope equipped with an oil immersion objective lens (Olympus, UPlanSapo 100X/1.4) as seen in the figure 14. Synthetic NDs (Quantum Particles 25, Microdiamant AG) with an average size of 25 nm containing mainly one or two NV^- defects were used. Illuminating the sample with a linearly polarized CW laser emitting at 532 nm (Shanghai Laser &

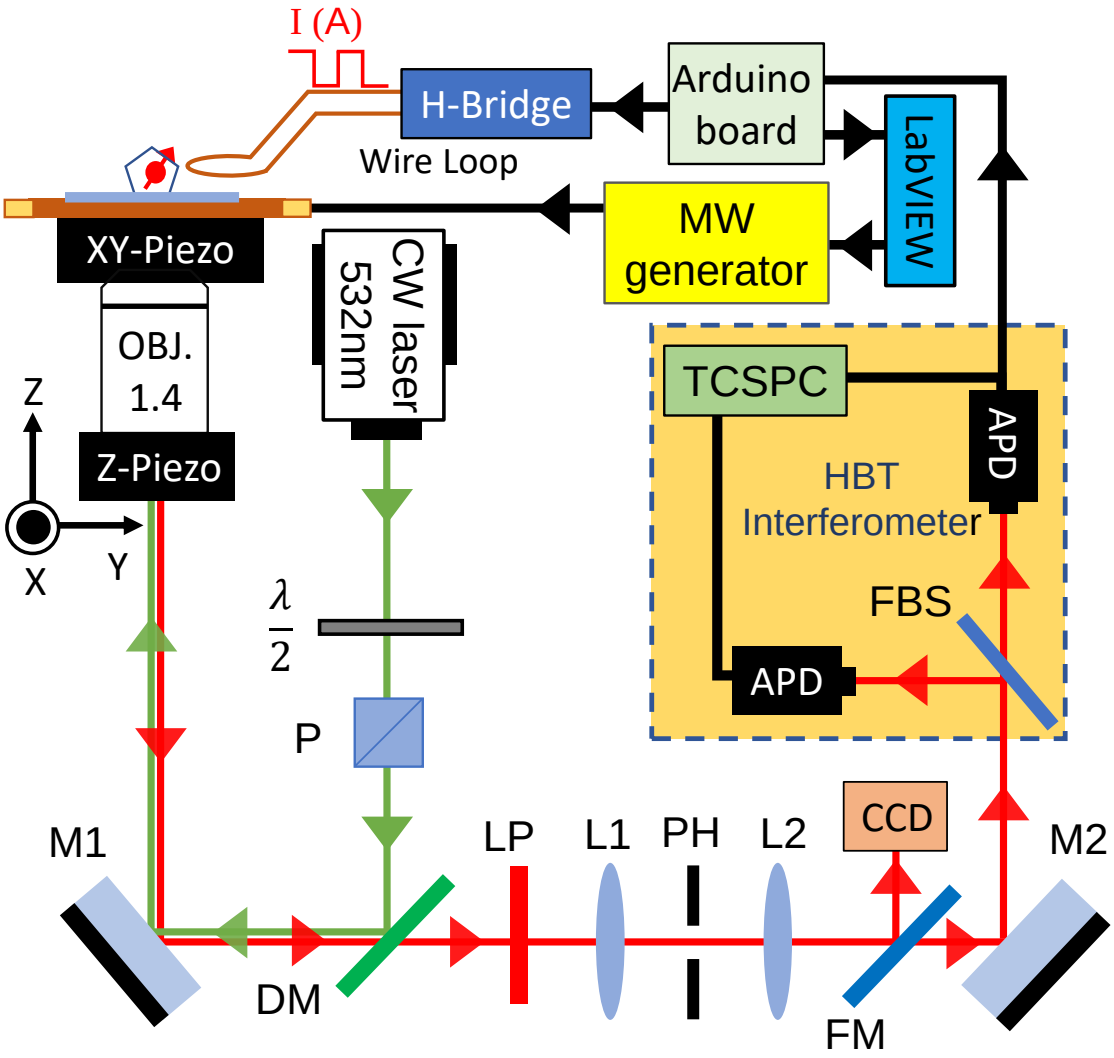

Figure 14: Sketch of experimental setup. The CW (532 nm) laser is the excitation source. A half-wave plate $\lambda/2$ and the polarizer (P) are used to control the laser power of the laser delivered to the microscope. Light is reflected by the dichroic mirror (DM) to the high NA objective (OBJ.), which focuses light on the nanodiamond (ND) and collects its PL. A Long Pass (LP) filter is used to eliminate residual excitation light, L1 lens focuses the PL towards the pinhole (PH) used as spatial filter and lens L2 collects the divergent PL and collimates it again. Then, the PL can be sent toward a high sensitivity CCD camera by flipping a mirror (FM) to obtain an image or to a HBT interferometer to measure $g^{(2)}(\tau)$. A flip-mounted 50:50 beam splitter (FBS) can be removed to use only one APD for PL detection. Thus electrical signal generated for every photon detected from this APD is sent to microcontroller and converted in photon counts. LabVIEW is an intermediary software of control, which receives information from the microcontroller necessary to calculate and send the appropriate value of ν_{MW} and estimate the magnitude of the magnetic field as well. M1(M2): mirrors.

Optics Century, GL532T3-200), used as excitation source, a ND is located by scanning the antenna (figure 13a) on the coverslip across the excitation laser focal spot and detecting the ND PL with an avalanche photodiode (APD; PerkinElmer, SPCM-AQR-14). The laser power (P = 250 μW) before the objective lens is controlled by the $\lambda/2$ plate and a polarizer as seen in figure 14. The dichroic mirror (DM, Semrock FF562 DI03) and long pass (LP) filter (Semrock, FF01-593/LP) ensure that the residual light from the excitation does not reach the APDs. The spatial filter composed of L1, PH, and L2 blocks light coming from the perifocal region and allows higher resolution images of the NDs. Since one wants to select a ND hosting a single NV^- center, the setup is coupled to a Hanbury-Brown and Twiss (HBT) interferometer, which is used to record the second-order correlation function, $g^{(2)}(\tau)$, of the emitted PL using a Time-Correlated Single-Photon Counting (TCSPC) module (PicoQuant, TimeHarp200) that measures the temporal difference between one arrival photon in one APD and another photon detected by a second APD (details in the next chapter). The flip-mounted 50:50 beam splitter (FBS) can be removed to send the fluorescence towards only one APD. The TTL electrical signal from the output of this APD is sent to an Arduino board that has a microcontroller, which is programmed to perform different tasks making possible the realization of the magnetometer. Details of this microcontroller will be discussed in section 3.3.

3.2 Design and calibration of electromagnets to produce magnetic fields

As discussed in section 2.5, the determination of the magnetic dipole moment axis orientation is relevant for measuring magnetic fields. Besides, by solving the Hamiltonian to find the energy eigenvalues, an expression (see equation 2.17) to determine the electron spin resonances was obtained. The interpretation of this expression shows that it is possible to build a system to generate magnetic fields in a static reference frame from the perspective of the ND coordinate frame to measure the orientation of its magnetic dipole moment direction. Thus, it is convenient for this work to build a coils system in a

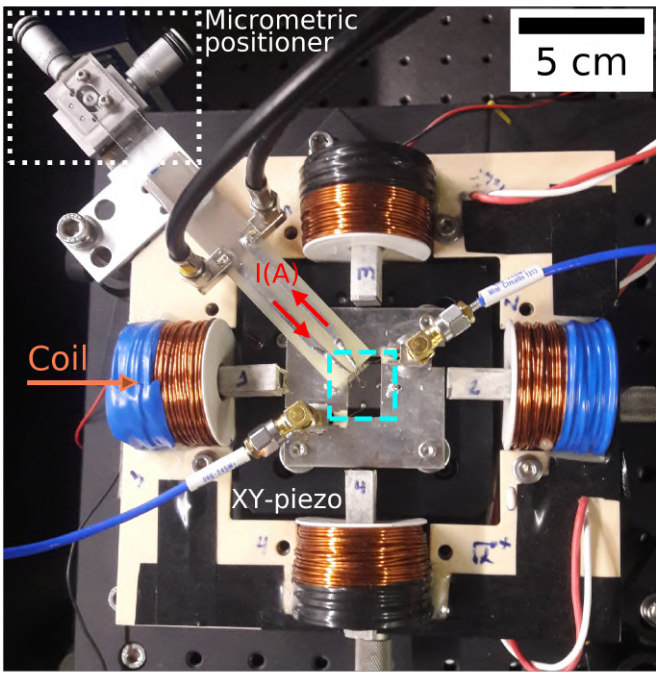

(a)

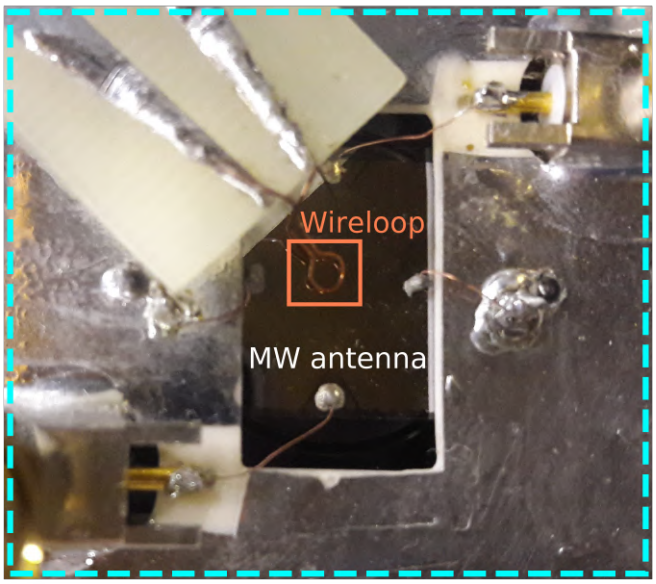

(b)

Figure 15: (a) Homemade, computer-controlled system for generating DC and AC magnetic fields up 15 mT in amplitude. This system can independently generate X and Y components of a magnetic field in the plane of the sample (Z=0), giving rise for example to an arbitrarily-oriented, rotating, magnetic field. The dotted rectangle (upper left corner) shows a micrometric positioner to bring a wire loop close to the ND. (b) Zoom of the dashed rectangle in the central area from (a) depicting the MW antenna where NDs are deposited and the wire loop used to drive the square wave current, I(A), to generate the ESR modulation magnetic field.

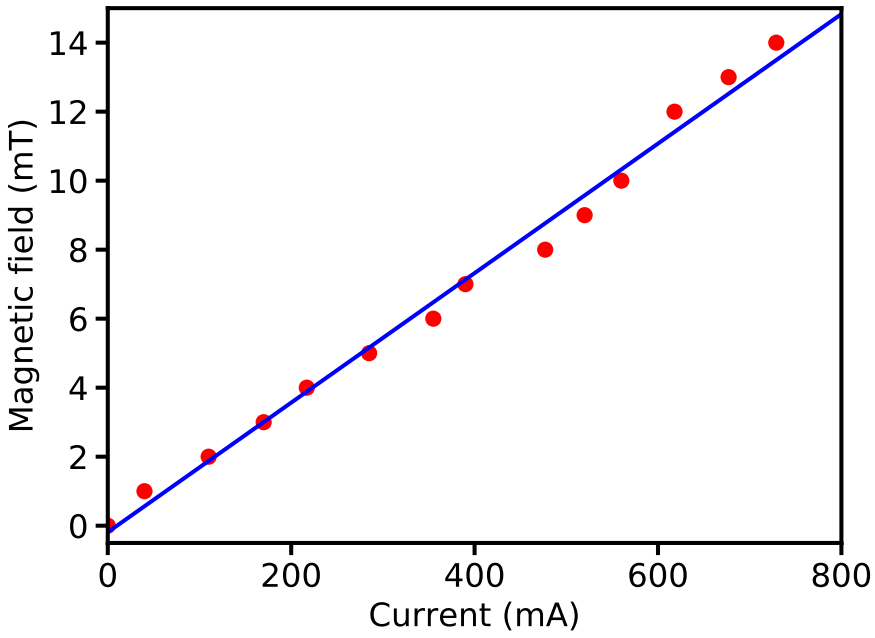

(a)

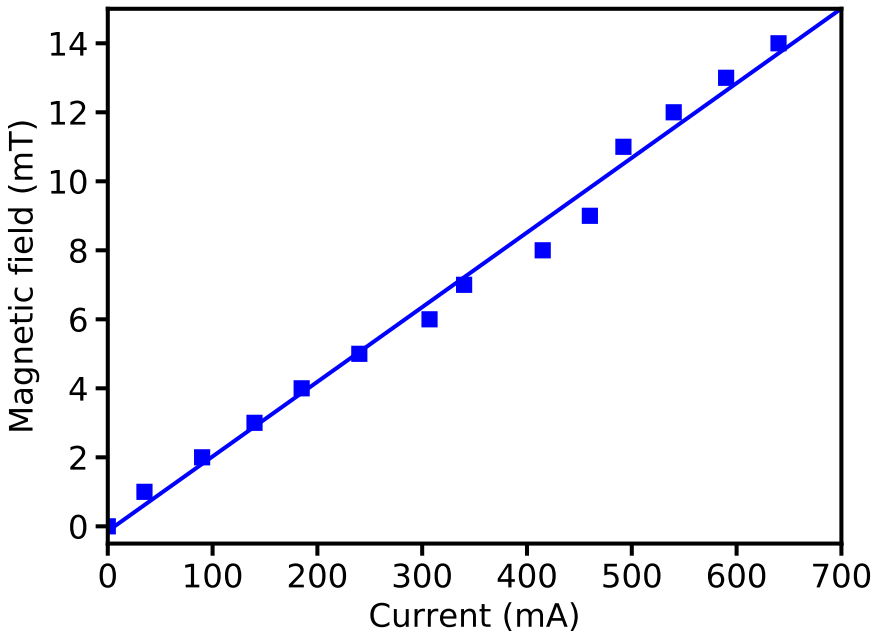

(b)

Figure 16: (a) and (b) show the coil calibration data obtained using a Hall probe while a DC current flows through the coils, placed along the X and Y axes respectively, was increased. Slope in (a) is lower than in (b), which means that coils in the X-axis needs more current to reach the same magnetic field amplitude than coils in Y-axis.

Helmholtz configuration (as seen in figure 15a) to generate the required magnetic fields. To fabricate those coils (22 turns per layer, 17 layers), copper wire with 1 mm of diameter was wound on PVC spools (11 mm of internal diameter and 24 mm long). To increase the field strength at the ND location, iron cores were introduced in the spools. The control system can independently drive the currents flowing through the two pairs of Helmholtz coils oriented along the X and Y directions using a visual programming language, LabVIEW. Furthermore, the magnetic field at the sample position was calibrated as a function of the driving currents using a Hall probe. The calibration results are plotted in figure 16. Linear fitting was done to obtain the slopes of the resulting curves, which gives us an important parameter that is introduced in the block diagram created in LabVIEW to determine/control the strength of the magnetic fields. With the coils built and calibrated it is possible to measure the dipole axis orientation, as described in section 2.5.

In order to implement a magnetometer which involves reasonable sensitivity in comparison with other sophisticated systems, compact design, easy manipulation and low cost, an electronic system (microcontroller-based, details in the next section) was developed, to feed a wire loop (500 μm of diameter) through which square current (A(I)) pulses are applied. As depicted in figure 15a, two cables drive the current pulses (ranging from 0 to 500 mA) toward the wire loop through two connectors, generating an alternating square magnetic field. To move the wire loop and bring it close to the position of the ND, a XYZ micrometric positioner (figure 15a) is used. Due to the Zeeman effect produced by the alternated magnetic field, B_{mod}, modulation of the ESR frequency is observed. By monitoring this modulation, it is possible to measure an external magnetic field, B, only making tracking of the ESR frequency by detecting changes of the fluorescence intensity and measuring its shift in response to an external magnetic field applied. Every step taken to reach a magnetic field measurement is performed by a microcontroller programmed to execute different tasks in real-time. Details about the implementation of a magnetometer using that microcontroller are presented in the next section.

3.3 Microcontroller-based magnetometer implementation

To carry out magnetometry experiments using the chosen approach it is necessary to implement a control system that can perform different tasks in a synchronized way (see details of the circuit in Appendix A). Thus, it is impossible to escape from programming and automation. Besides, it is important for this work to use a low cost hardware/software easy to use but good enough to realize high level experiments. For this reason, Arduino becomes an excellent tool for our purposes.

The present implementation employs an Arduino Due microcontroller as the control device. Although Arduino is not the fastest microcontroller available, this does not represent a limitation because its clock oscillates at 84 MHz, meaning that a single computational operation with this device requires $\sim$ 12 ns. Considering that the lifetime of the NV^- defects is around 1 ns and taking into account that the collection+detection efficiency of the setup is $\sim 0.1\%$, one can detect PL photons at rates of almost 1 MHz (one photon each μs) such that Arduino is $\sim 80\times$ faster than this. The choice of a member of the Arduino family to implement the nanomagnetometer was based on its versatility, translated by the fact that Arduino has its high-level programming language (contrarily to what happens to other faster microcontroller types), which facilitates the task of programming. This makes Arduino microcontrollers very popular, counting with a large community of users, who in turn produce vast documentation, publicity available in the World Wide Web. Besides this, Arduino has several analog and digital inputs and outputs that allow communication with other equipment and devices via Transistor-Transistor Logic (TTL) signals [88].

In the present case, Arduino must be able to recognize the pulses coming from the APDs, whereby an analog circuit was designed to adequate the pulse width and intensity to the TTL standard (see Appendix A). For ESR modulation, another Arduino-controlled approach is implemented that incorporates a bipolar home-made current source (H-Bridge), a device that feeds the wire loop allowing the generation of magnetic field square pulses in alternating senses (as seen in figure 14). Within the framework of the task that the

microcontroller must perform as an essential device for data acquisition, it must synchronize APD pulses with the MW generator signal, the modulation field, and separately allocate each data (APD counts) in different variables of the control program for further analysis as well. To reach these goals, a C++ programming language is used (see Appendix A). With such an approach, it is possible to perform some counting modes, such as differential and integral, and other tasks, as the implementation of real-time digital filters. The information exchanged between the microcontroller and the computer is done by serial Universal Asynchronous Receiver-Transmitter (UART) communication protocol and used LabVIEW to acquire and save this pre-processed data, which is useful when one runs the programs (in LabVIEW) that allow us to determine magnetic filed in real-time and make magnetic imaging. Thus, Arduino also works as the intermediate step in data processing and analysis.

Chapter 4

Experimental results

This chapter presents the different measurements carried out using the implemented setup and the microcontroller on an Arduino board. It begins with the characterization of NDs that allows us to find single photon emitters followed by the NV^- defect magnetic dipole moment axis orientation measurement. Then, an explanation of the approach to measuring magnetic fields using the Zeeman effect is given, taking into account a Lorentzian lineshape for the ODMR curve. To optimize the magnetic field measurements, the capabilities of the system will be evaluated, like the sampling time and sampling mode. Besides, the linearity of the system is checked and its capability to measure AC fields is investigated. Finally, the magnetic field gradient produced by a magnetized microwire is imaged using the developed nanomagnetometer.

4.1 Nanodiamond characterization and determination of the NV^- defect magnetic dipole moment orientation

Localization of NDs can be easily reached by scanning confocal image (figure 17a) and observing its fluorescence spectroscopy as seen in figure 3, but to determine whether the ND contains a single NV^- defect it is necessary to measure its antibunching behavior (see figure 17b). In the present work, it is essential to know whether the ND investigated

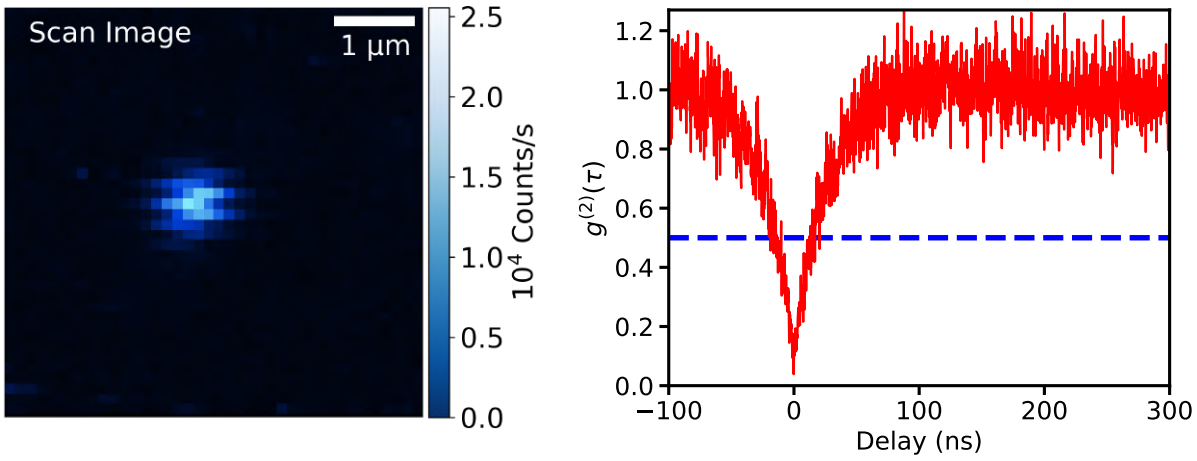

(a) (b)

Figure 17: (a) Typical PL scan image (5 μm×5 μm) showing that a ND was detected. (b) Second-order correlation function recorded by means of a photon coincidence histogram. The antibunching dip below the dashed blue line indicates $g^{(2)}(0) < 0.5$, which is enough to ensure the single-photon character of the emitted light.

has only a single defect, for which an implementation of experimental procedures used in quantum optics is relevant to measure the photon antibunching [91, 92] by recording the second order correlation function $g^{(2)}(\tau)$ (details in Appendices) of the emitted PL of the ND.

In order to detect NDs firstly a scan over a micrometric region of the MW antenna is performed using an XY piezo (see figure 14) while the CW laser illuminates the sample. A typical scanning PL (with an average brightness of 3×10^4 counts/s) image is depicted in figure 17a. Since one wants to select a ND hosting a single NV$^-$ defect, the setup is coupled to a Hanbury-Brown and Twiss interferometer, to record $g^{(2)}(\tau)$ of the emitted PL. Figure 17b shows the unsaturated antibunching behavior with $g^{(2)}(0) < 0.5$, ensuring that a single emitter was selected (for more details see Appendix C). Thus, all measurements presented in this work will be performed with this single emitter.

Then, PL signal can also be sent to an APD that activates a TTL electrical signal for every photon count. The Arduino microcontroller counts these pulses with a temporal resolution of 12 ns. Furthermore, a MW generator feeds the photolitographed antenna to perform ODMR. In this canonical approach, the PL intensity is recorded as a function of

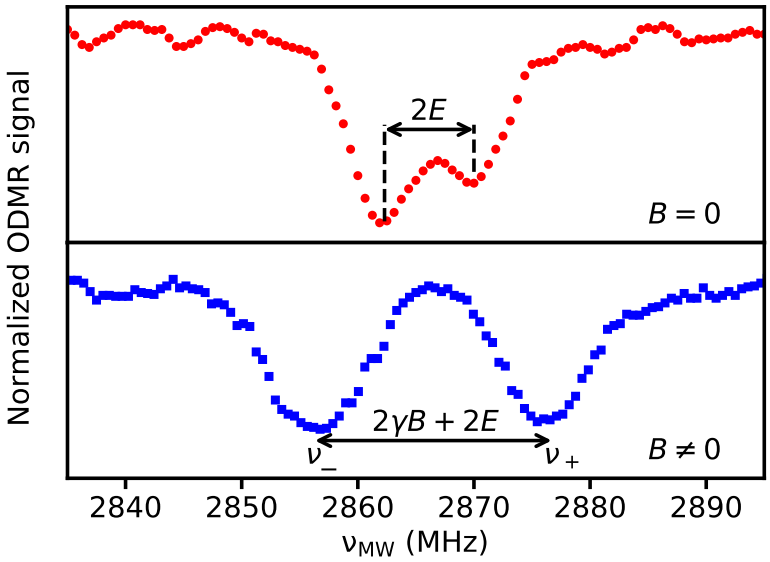

Figure 18: Normalized ODMR spectra of a single NV$^-$ defect in the absence (red dots) and presence (blue squares) of an external magnetic field generated by a permanent magnet brought close to the ND. The typical ODMR signal contrast is around 15% for both ESRs. The spectrum in the absence of the external magnetic field allows determining the piezoelectric coupling constant $2E = 7.2$ MHz.

the MW frequency ν_{MW}. As already discussed, whenever it meets the resonance condition for spin transitions $m_s = 0 \rightarrow m_s = \pm 1$, spin flips occur and the emitted PL decreases.

The ODMR spectra shown in figure 18 exhibit two ESRs separated by $2E = 7.2$ MHz due to the natural ESR splitting at zero external magnetic field. As previously mentioned, this is related to surface strain present in nanodiamond associated with the piezoelectric properties of this matrix and/or the presence of residual external electric fields. When an external magnetic field is present, the Zeeman effect accounts for further splitting. The simplified spin Hamiltonian neglecting the hyperfine interactions reads as equation 2.3. One can compute the energy eigenvalues of the NV$^-$ defect Hamiltonian in order to find the ESR frequencies $\nu_\pm$ as a function of any magnetic field amplitude. For small transverse field components ($B_z^2 \gg B_x^2 + B_y^2$) and weak magnetic fields amplitudes such as $B_z \ll hD/g\mu_B \approx 100$ mT, the eigenfrequencies were computed from equation 2.13. In NV$^-$-based magnetometer, the knowledge about NV$^-$ axis orientation is valuable and has to be determined. As mentioned before, the spin-coating procedure used to deposit the NDs on the MW antenna randomizes the NV$^-$ symmetry axis orientation, and it must

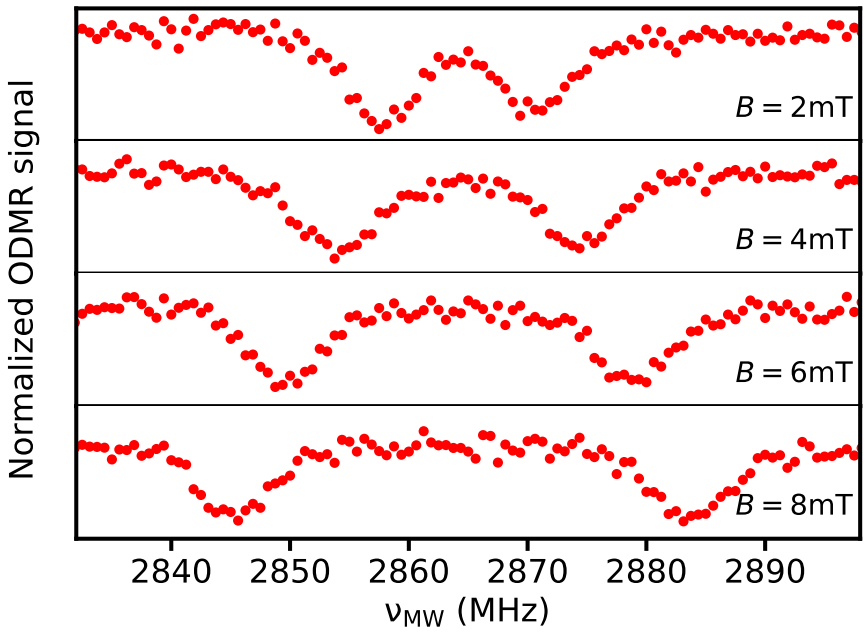

(a)

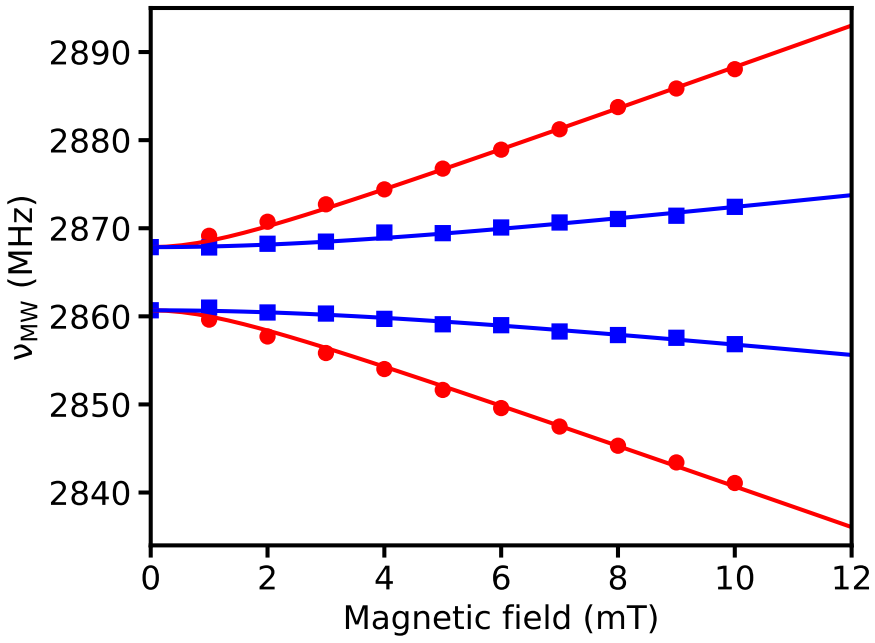

(b)

Figure 19: (a) ODMR signal recorded for different external magnetic field amplitudes while the frequency of the microwave field is swept. (b) ESR frequencies ν_{MW} as a function of the external magnetic field applied along the X (red circles) and Y (blue squares) directions. The solid lines are fittings of equation 2.19, with best fit parameters $\theta = 5.0°$ and $\varphi = 16.3°$.

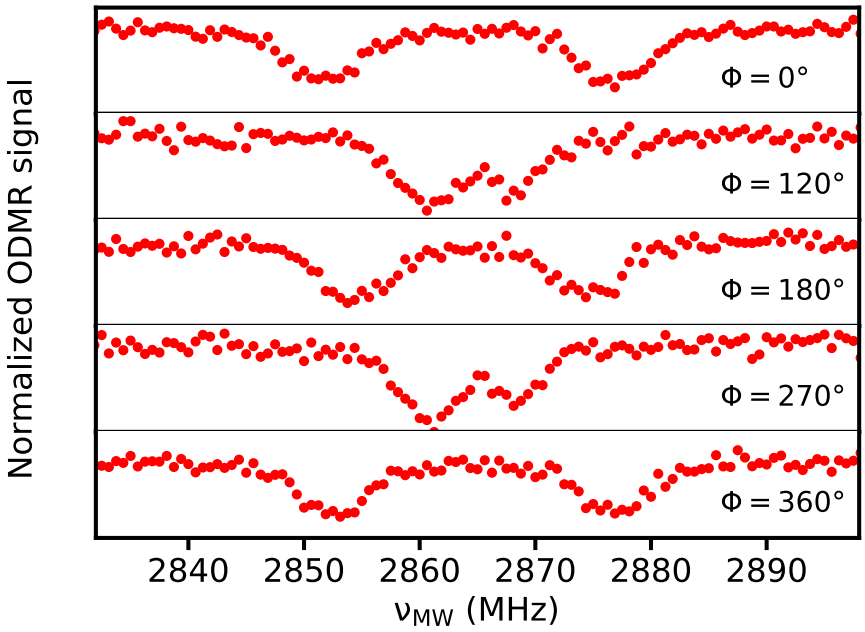

(a)

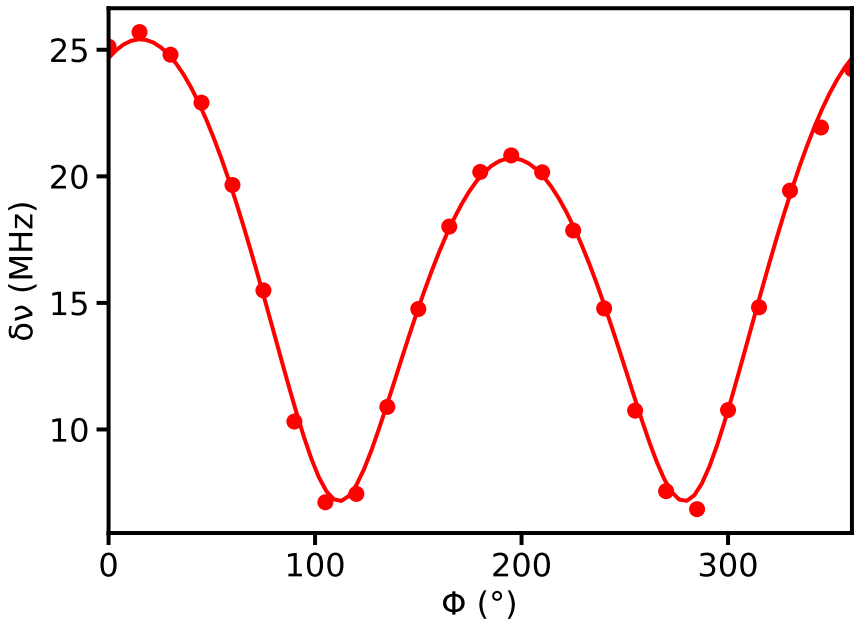

(b)

Figure 20: (a) ODMR signal is recorded while the microwave frequency is swept, keeping a constant magnetic field amplitude of 5 mT. This was performed for every field rotation angle, Φ, around the Z-axis. (b) Split $\delta\nu = \nu_+ - \nu_-$, as function of the orientation Φ of the external magnetic field direction rotated in the Z=0 plane. The solid line is a fit of the equation 4.1, with best fit parameters $\theta = 4.6°$ and $\varphi = 15.3°$. Φ starts from X-axis.

be measured for each single ND studied. A coordinate transformation from the NV^- *xyz* coordinate system to a laboratory XYZ reference frame leads to equation 2.16 where θ and φ are the polar and azimuthal angles, respectively, of the NV^- defect magnetic dipole moment orientation in the laboratory reference frame as depicted in figure 7.

In order to determine the NV^- symmetry axis orientation, a home-made automated system was used (see section 3.2). ODMR spectra were taken varying the amplitude of the DC magnetic field created by the Helmholtz coils (as seen in figure 19a) independently along the X and Y directions. The measured ESR central frequencies are shown in figure 19b, and fitting was done using equation 2.17. It is then obtained that $\theta = 5.0°$ and $\varphi = 16.3°$ for the spatial orientation of this NV^- defect, indicating that its magnetic dipole moment stands almost perpendicularly to the coverslip.

Another possibility to determine the NV^- axis orientation angles is to fix the magnetic field magnitude (set to $B_0 = 5$ mT in the present experiments) in the Z=0 plane and to rotate it by an angle Φ around the Z-axis while recording the ODMR spectra for each value of Φ, as shown in figure 20a. From the equation 2.20, the ESR splitting can be rewritten as

$$\delta\nu = 2\sqrt{\left(\frac{g\mu_B B_0 \sin\theta}{h}\right)^2 [\cos(\varphi - \Phi)]^2 + E^2} \tag{4.1}$$

and is recorded as a function of the field rotation angle Φ. The results are depicted in figure 20b, and a fitting indicates that $\theta = 4.6°$ and $\varphi = 15.3°$ for the NV^- symmetry axis orientation. The average of the results retrieved from both approaches, $\theta = 4.8°$ and $\varphi = 15.8°$, was then adopted as the magnetic dipole moment orientation angles of the NV^- defect used throughout the entire work.

4.2 Measurement of external magnetic fields: method

Measurements of external magnetic fields are performed with prior ND characterization and determination of the NV^- defect magnetic dipole moment spatial orientation, as

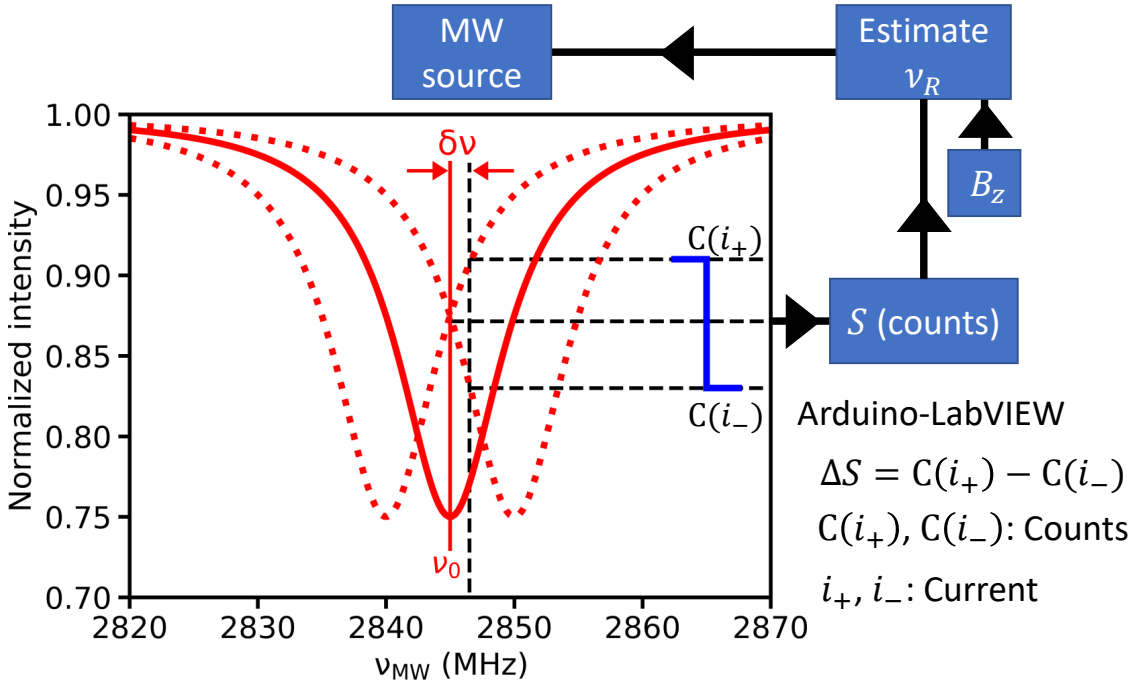

Figure 21: ODMR signal (continuous red line) showing one ESR frequency. $\delta\nu$ is a frequency shift produced when an external magnetic field is applied. A square wave current creates an alternating magnetic field that modulates the ESR frequency as depicted with the two red dotted lines. ΔS is the error signal measured, given by the count's difference between $C(i_+)$ (photon counts when the current is positive) and $C(i_-)$ when current is negative. Then, this error signal is processed to estimate the magnetic field and find the MW frequency, ν_{MW}, corresponding to the new ESR condition.

previously described. Thereby, one gets the system ready to be used as a nanomagnetometer. As described in the section 3.3, an Arduino Due board was used to control the polarity of a H-Bridge employed to generate a square wave current that feeds a wire loop antenna. The resulting AC magnetic field modulates the ESR frequency and can be used to generate an error signal as follows: When the MW is in resonance with the NV^- electronic spin transition, the symmetric modulation of the AC magnetic field by $\pm\delta B_{mod}$ implies equal PL counts during both modulation magnetic field orientations, as seen in figure 21. A differential measurement, therefore, results in zero counts when the MW field is resonant with the spin transition. The presence of an external magnetic field shifts the ESR, unbalancing the PL differential counts. This imbalance generates an error signal that can be used to correct the MW frequency and re-establish a balanced condition. By knowing the NV^- axis orientation and tracking the frequency shifts due to external magnetic fields,

it becomes possible to determine the amplitude of the external magnetic field over the NV^- magnetic dipole.

To better understand the implemented lock-in procedure, in what follows it is assumed that the splitting between the $m_s = \pm 1$ Zeeman sublevels is large enough so that only the ODMR due to a single Zeeman sublevel is considered. The MW signal is kept at a constant frequency ν_0 (resonant to the spin transition, leading to zero differential counts) while the magnetic field due to the square current signal modulates the NV^- ESR Zeeman shift at a known frequency ν_{mod}. The quantity $S(\nu_{MW} - \nu_0)$ is defined as the PL signal for a fixed MW frequency, when the tracked ESR frequency is ν_0 (either ν_+ or ν_-). Since the external magnetic field modulates ν_0 by $\pm\Delta\nu_0$ through a square wave, it is possible to measure $S(\nu_{MW} - \nu_0 + \Delta\nu_0)$ and $S(\nu_{MW} - \nu_0 - \Delta\nu_0)$ by collecting light synchronously to the current modulation and obtain their difference to first order as

$$\Delta S(\nu_{MW} - \nu_0) = 2\frac{dS(\nu_{MW} - \nu_0)}{d\nu_{MW}}\frac{d\nu_0}{dB_{mod}}\delta B_{mod}, \tag{4.2}$$

where $\Delta\nu_0 = \frac{d\nu_0}{dB_{mod}}\delta B_{mod}$ is the resonance frequency shift induced by the modulation field. Notice that $\frac{dS(\nu_{MW}-\nu_0)}{d\nu_{MW}}$ can be determined from the ODMR curve directly. Meanwhile, $\frac{d\nu_0}{dB_{mod}} = \pm g\mu_B/h$, when the total Zeeman shift of the sublevel $m_s = \pm 1$ is much larger than the natural split $2E$. Indeed, this condition can be easily satisfied with the application of a bias field and is required for NV^- magnetometry. The modulation amplitude δB_{mod} can be calibrated by measuring the peak to peak variation in ΔS as a function of ν_{MW} such that all terms in equation 4.2 can be determined.

The microcontroller counts the detected photons in phase with the applied square wave modulated current and determines ΔS. If $\nu_{MW} = \nu_0$, then $\frac{dS(\nu_{MW}-\nu_0)}{d\nu_{MW}} = 0$ (ODMR curve minimum) and $\Delta S = 0$. A small diference between ν_{MW} and ν_0 due to a varying external magnetic field will lead to $\Delta S \neq 0$. Assuming a Lorentzian lineshape for the ODMR curve [93, 94], one has

$$S = I_0\Delta t\left[1 - \frac{C}{(\nu/\Gamma)^2 + 1}\right], \tag{4.3}$$

where I_0 is the PL emission rate, Δt is the integration time, C is the ODMR spectrum contrast, and Γ is the ESR linewidth. For small variations in ν_0 (for example, due to an external magnetic field), using the equation 4.3, equation 4.2 becomes

$$\Delta S(\nu_{MW} - \nu_0) = I_0 \Delta t \frac{4C\delta\nu_0}{\Gamma} \frac{g\mu_B \delta B_{mod}}{h\Gamma}. \tag{4.4}$$

Thus, if the resonance frequency shifts by $\delta\nu_0$ due to the presence of an external magnetic field, then ΔS is proportional to this shift. A characterization of this system determines such proportionality constant and allows to compensate this frequency shift through the MW field by tuning the MW frequency making $\delta\nu_{MW} = -\delta\nu_0$. Tracking ν_{MW} such that $\Delta S \approx 0$ allows to follow the local magnetic field perceived by the NV^- magnetic dipole moment through equation 2.13.

Finally, it is worth remarking that in the limit of small $\Delta\nu_0$, equation 4.4 also can be written as

$$\Delta S(\nu_{MW} - \nu_0) = \frac{\Delta S(\nu_{MW} - \nu_0)}{d\nu_{MW}}\Big|_{\nu_{MW}=\nu_0} 2\Delta\nu_0, \tag{4.5}$$

and the slope of $\Delta S(\nu_{MW} - \nu_0)$ *versus* ν_{MW} close to $\nu_{MW} \approx \nu_0$ can be used to directly calibrate how the experimental system responds to external magnetic fields. When $\Delta\nu_0$ is due to those fields only, $\Delta\nu_0 = \frac{d\nu_0}{dB_z}\delta B_z$, where $\frac{d\nu_0}{dB_z} = g\nu_B/h = 28$ MHz/mT. The sensitivity can also be rewritten in the terms of directly measurable parameters as

$$\eta = \left[\frac{d\Delta S(\nu_{MW} - \nu_0)}{d\nu_{MW}}\right]^{-1}_{\nu_{MW}=\nu_0} \frac{dB_z}{d\nu_0}\sigma_{\Delta S}\sqrt{\Delta t} \tag{4.6}$$

where $\sigma_{\Delta S}$ is the noise in ΔS.

4.3 Evaluation of the system capabilities

Using the previously described approach, it was possible to track the frequency of an ESR in real-time and, thus, measure the amplitude of external static and time-varying magnetic fields. The Arduino board counted with an integration time of 100 ms the number of PL

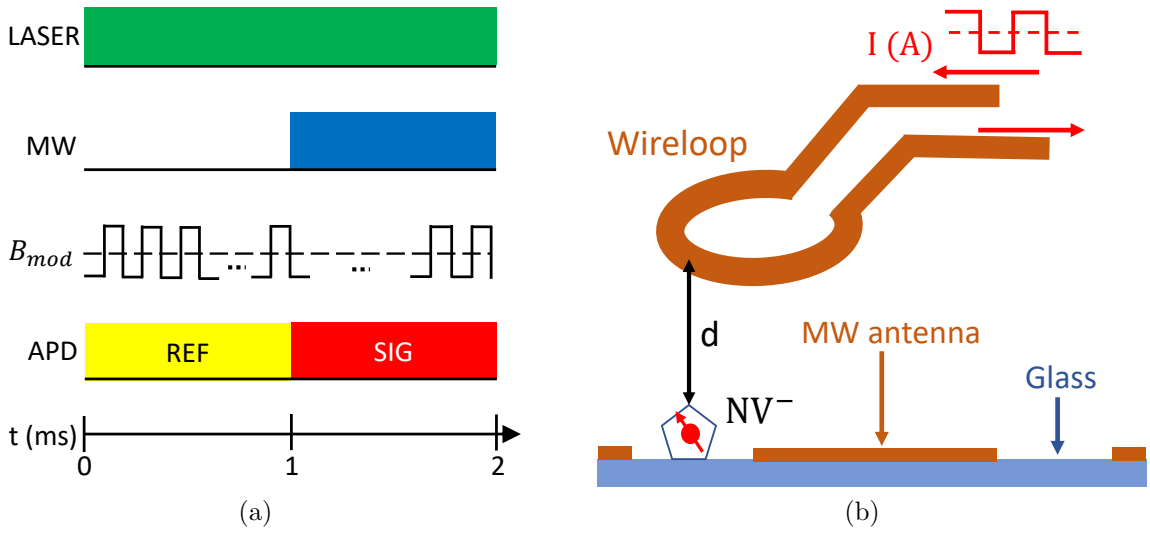

Figure 22: (a) Pulse sequence implemented to modulate the ESR frequency employing a modulation field B_{mod}. (b) Side view scheme (not to scale) of the microwave antenna lithographed on a coverslip and a ND with a single NV^- defect pictorially represented on it. A wire loop is placed to a distance of d∼250 micrometers from its center towards the ND sample.

photons phase-locked with the square wave AC modulation magnetic field switched at 10 kHz unless otherwise noticed. To calibrate the magnetometer, one ESR is chosen and the error signal $\Delta S(\nu_{MW} - \nu_0)$ is monitored while sweeping the MW frequency around this resonance.

The pulse sequence designed to perform this task is depicted in figure 22a and the protocol is the following: First, the spin states are optically initialized in $m_{gs} = 0$ via optical pumping at 532 nm, keeping the laser ON all the time. The modulation field B_{mod} is also activated with a 50% duty cycle, which symmetrically modulate the spectral position of the spin transition line. The APD is always detecting photons coming from the ND sample while a routine written in Arduino software, known as Integrated Development Environment (IDE), separates photon counts during the first millisecond when the MW is OFF (reference signal-REF) and the last millisecond when the MW is ON (fluorescence signal-SIG). During all this process the routine of the program also separately allocates the photon counts in different variables corresponding to photons counted depending of the direction of the current that generates the B_{mod}. This pulse sequence is repeated for every

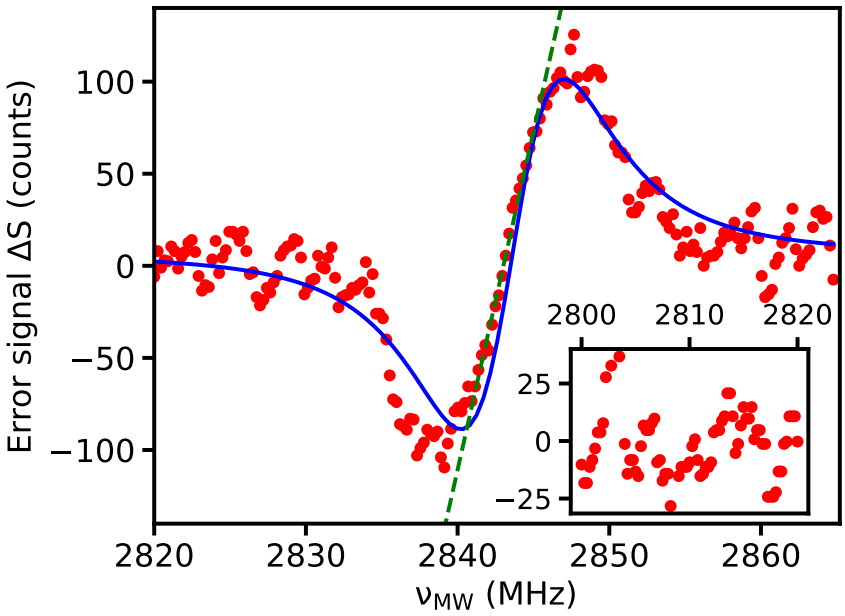

(a)

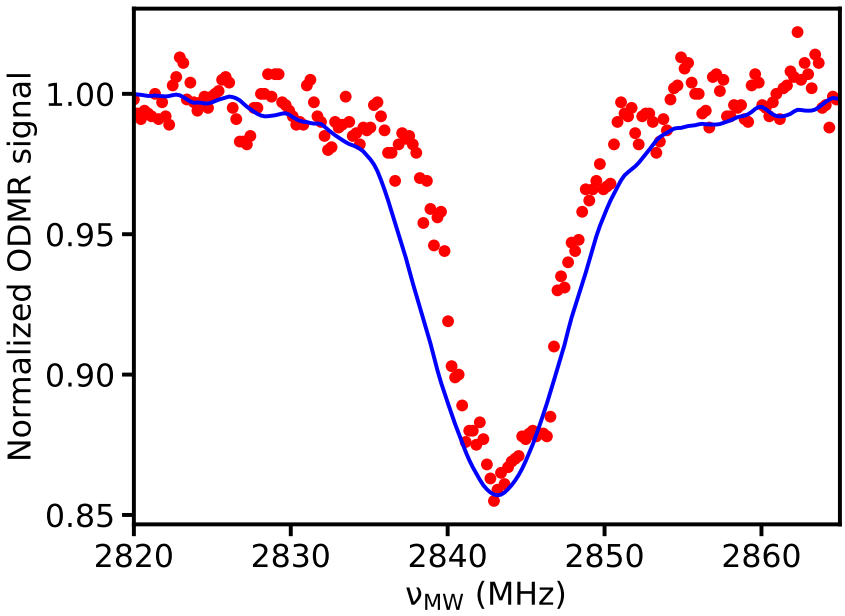

(b)

Figure 23: (a) $\Delta S(\nu_{MW} - \nu_0)$ for B_{mod} switching at 10 kHz in the vicinity of an ESR (red circles). The dashed green line presents a slope of 37.6 counts/MHz. Inset shows the signal baseline with a standard deviation of $\delta_{\Delta S} = 12$ counts for ν_{MW} far from the ESR. The solid line represents the fit to the data using the derivative of a Lorentzian lineshape and is used to determine the modulation depth $\frac{g\mu_B \delta B_{mod}}{h\Gamma} = 0.14$. (b) Normalized ODMR spectrum around the resonance (red dots) and integral of data in (a) (solid blue line). The integral of $\Delta S(\nu_{MW} - \nu_0)$ is smoother than the direct measurement of the ODMR curve for the same integration time per frequency step. As required, the frequency for which a dip is observed in the ODMR curve coincides with the frequency for which the signal in (a) is zero.

MW frequency value and integrated during 100 ms, along the entire sweep. Data shown in figure 23a is consistent with a signal proportional to the derivative of the ODMR signal. Indeed, the solid curve in figure 23a is a fit of experimental data using the derivative of a Lorentzian lineshape and consistent with a modulation depth of $\frac{g\mu_B\delta B_{mod}}{h\Gamma} = 0.14$. The original ODMR spectrum can be recovered by integrating the signal in figure 23a, resulting in the smoother blue curve shown in figure 23b, evidencing a broadening of the linewidth by a few MHz. This is because for the ideal case when the ESR modulation field is small, it is taken only as perturbation without an appreciable effect in the resonance broadening. In this work, however, the observed ESR curve broadening is produced by the modulation field that contributes to the linewidth broadening. In fact, the field amplitude, which is more or less arbitrarily chosen for modulating the ESR has a power strong enough to broaden the ESR curve by few MHz, as the following estimate shows: taking into account that the output power of the microwave generator (Aim & Thurlby Thandar Instruments TGR6000) is -30dBm or 1 μW (this is a parameter under the experimentalist's control) it is possible to estimate the power that passes through the antenna after being amplified (Mini-circuits ZHL-16W-43-S+) by 45 dB. Thus, according to the definition

$$\text{gain power (dB)} = 10\log\left(\frac{\text{RF Output Power}}{\text{RF Input Power}}\right). \tag{4.7}$$

Then, replacing properly

$$45 = 10\log\left(\frac{P_{out}}{1\mu\text{W}}\right), \tag{4.8}$$

and solving the equation 4.8, we get $P_{out} \sim 32$ mW. Due to the typical dimensions of the MW antenna, only for estimation purposes, one can suppose that the ND investigated was located at ~ 50 μm from its center (see figure 13a). Thus, due to the inverse-square law, the intensity at the position of the ND is ~ 13 $\mu\text{W}/\mu\text{m}^2$. On the other hand, the power generated by the current along the wire loop to produce the ESR modulation field also can be calculated. Using the following expression

$$\text{I}_\text{w}(\text{A}) = \sqrt{\frac{\text{P}_\text{w}(\text{W})}{\text{R}_\text{w}(\Omega)}}, \tag{4.9}$$

where I_w is the current flowing through the wire loop, P_w the power dissipated by it and R_w its resistance. In the experiment, an alternating current of 400 mA of amplitude was used to modulate the magnetic field, and the resistance of the wire loop was measured to be 45 Ω. Replacing values in equation 4.9, one obtains 7.2 W of MW power. As the wire loop is located ∼ 250 micrometers away from ND (see the scheme in figure 22b), one can estimate the intensity at the position of the ND to be ∼ 115 $\mu W/\mu m^2$. It means that the resulting intensity is ∼9× larger than the intensity generated by the antenna. The power added by B_{mod} produced by the wire loop becomes an additional dephasing channel for the electron spin coherence, implying in ESR broadening and loss of sensitivity. However, for the purposes of the present work, this broadening does not invalidate the applied method because the slope shown in figure 23a to generate the error signal takes this into account. This is a good sign because decreasing the power of the ESR modulation field will narrow the ODMR dip, thus increasing the slope in figure 23a, contributing to increasing the sensitivity of the device. What one should not confuse are the effects of both, the MW signal drives transitions between sublevels of the ground states whereas that B_{mod} modulates the resonance position.

In comparison with the standard ODMR measurement (red dots in figure 23b), the integral of the error signal is centered at the same frequency. From the data in figure 23a, equation 4.6 is used to determine that the system's noise floor is 12.6 μT. Using the equation 2.28, this corresponds to a field sensitivity of 4 $\mu T/\sqrt{Hz}$ at a 100 ms integration time per experimental point. Looking at figure 23, one sees that the method provides an error signal variation of ∼ 80% in a frequency interval of 5 MHz. On the other hand, the "standard" method consists of monitoring the NV^- PL at a microwave frequency where the ODMR curve slope is greatest. If one measures the NV^- PL on the greatest slope of the ODMR curve, variations in this measurement produced by shifts due to the external magnetic fields can give information about the strength of the applied magnetic field. In the "standard" method, the error signal variation is ∼ 13% in the same frequency interval. Thus, the approach used in the present work provides a sensitivity of ∼ 6× larger than the standard approach. And, as previously mentioned, this could be easily improved.

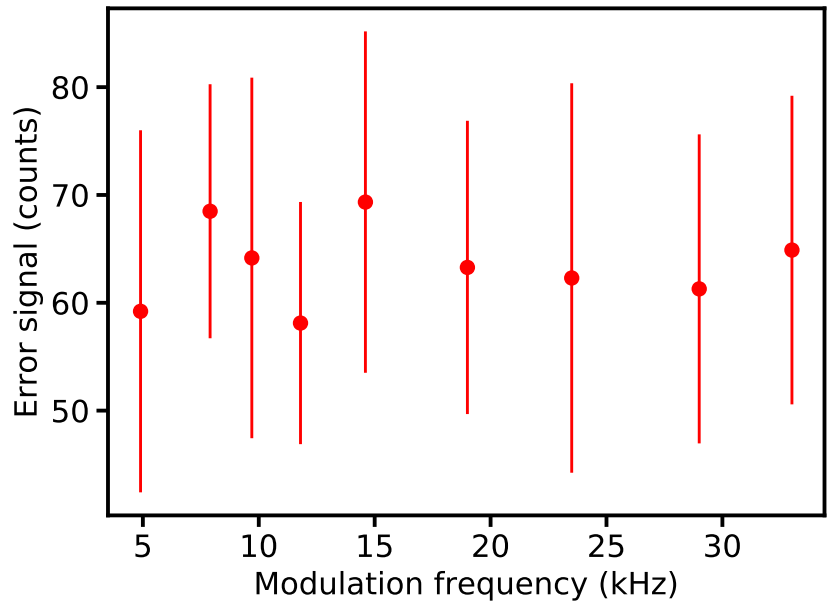

(a)

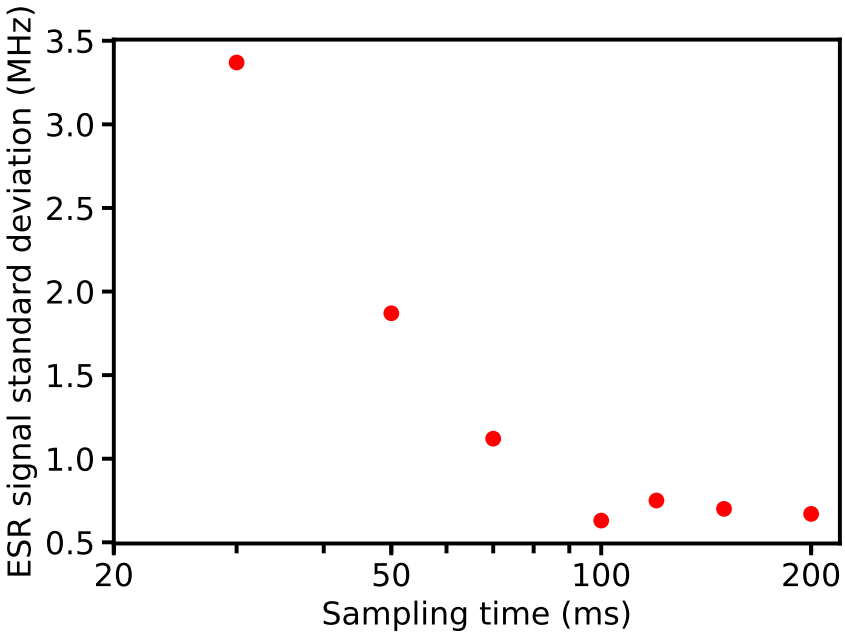

(b)

Figure 24: (a) Error signal amplitude as a function of the magnetic field modulation frequency, showing a constant behavior within the experimental uncertainties. (b) Noise at the ESR central frequency ν_0 as a function of sampling time. The noise was determined through the standard deviation of the signal measured by the tracking system after a time interval of 2 minutes.

Further measurements were performed to evaluate other system capabilities. Let's first consider the behavior of the system concerning the H-Bridge used to switch the wire loop current direction. The bridge is free from overshoot up to 40 kHz, producing a clean square wave current modulation. In figure 24a, it is shown that the magnetic field modulation frequency has no significant effect on the measured error signal. To operate the ESR modulation system more comfortably, it was then chosen to modulate the magnetic field at 10 kHz, which is sufficiently high to not limit the system's detection bandwidth. Now, let's examine figure 24b that shows the ESR signal standard deviation as a function of the sampling time. A nearly monotonic decreasing behavior can be seen practically not reducing further for a sampling time of 100 ms. Thus, sampling times of 100 ms were chosen as a good compromise between noise and speed for the following nanomagnetometry experiments.

4.3.1 Tracking of DC and AC external magnetic fields

To check the linearity of the measurement system upon external magnetic fields, a current ramp was applied to the Helmholtz coils pair oriented along the X-direction. Then, to follow the ESR position, a tracking system was developed in LabVIEW allowing monitoring in real-time the variation of the ESR frequency. Each ESR was tracked in a different run, and the results for the monotonic variation of ν_{MW} with time are shown in figure 25a. The linearity of the system is evident, while the separation between both ESR branches follows that expected for a Zeeman splitting.

The capability to measure AC magnetic fields was also verified. An ESR was tracked under the influence of an external magnetic field sinusoidally varying in time (amplitude of 6 mT, frequency of 0.1 Hz) applied through the pair of calibrated Helmholtz coils along the Y direction (figure 25b). The tracking system smoothly follows the applied AC signal, which demonstrates that the developed system measures magnetic field variations around 4 mT/s. 0.1 Hz was the highest experimental frequency that the present implementation was able to follow. This limitation could be because it is used as a serial communication protocol between LabVIEW and Arduino, which slows down the transfer of information

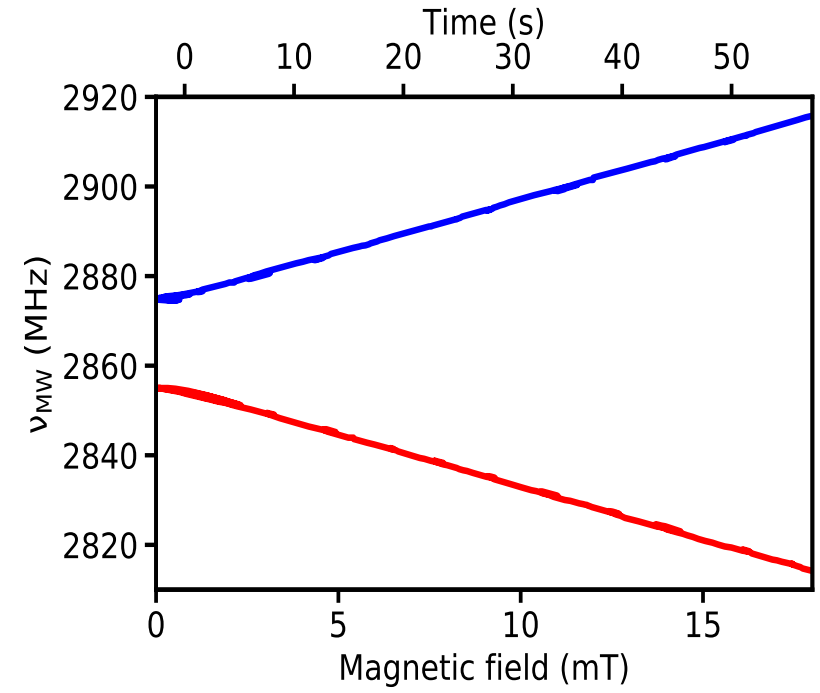

(a)

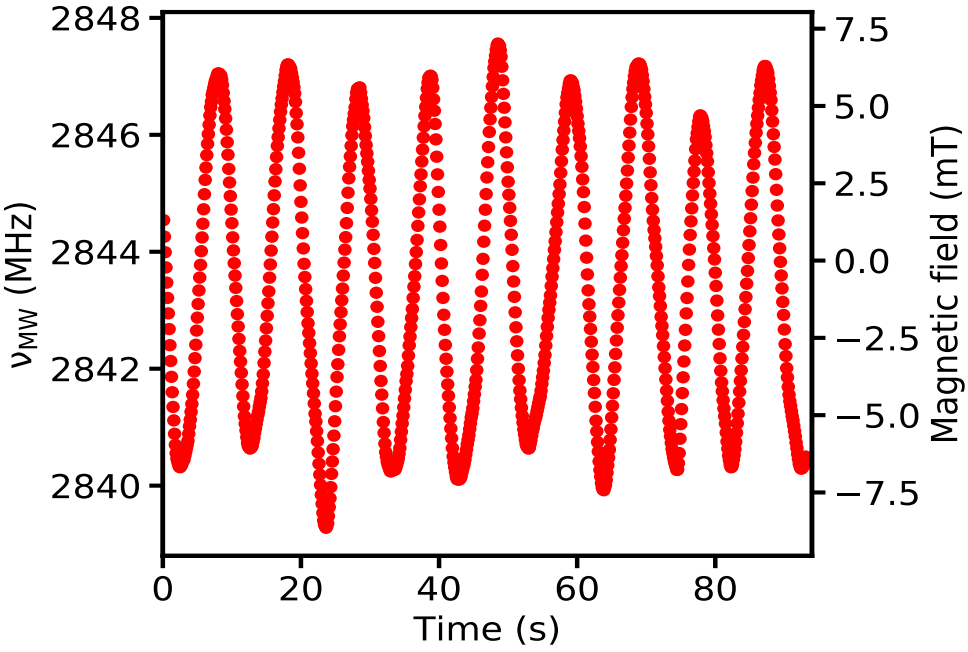

(b)

Figure 25: (a) Zeeman splitting induced by a DC magnetic field ramp produced by a calibrated Helmholtz coils pair oriented along the X-direction. The two ESR frequencies (ν_+, upper and ν_-, lower) were obtained in 2 different runs. (b) Real-time measurements of an AC magnetic field oscillating at 0.1 Hz. The closed loop control system can follow magnetic fields varying at rates around 4 mT/s.

between them. The variation in amplitude of the figure 25b is within the noise limit of the system. Notice from the figure 24b that the standard deviation of the system is 0.6 MHz, which agrees with the experimental data depicted in figure 25b.

4.4 Nanometric scale imaging of the magnetic field produced by a magnetic microwire

After the complete characterization of the ND and the system capabilities, the device was used to perform nanomagnetometry of a magnetic field produced by a magnetized steel microwire moved at a constant height over the ND. The wire has a submicrometer tip (as depicted with the electron microscopy image in figure 26a) that was obtained from a steel wool, which was cut with scissors in one of its endings to give the tip shape. Then, it was magnetized using a permanent magnet. This was sufficient to produce a detectable magnetic field gradient in a micrometer-scale region. To obtain a magnetic image, the steel microwire is inserted into a micropipette and glued (see figure 26b). This was fixed to a 2D piezo stage. Then, this tip was positioned over the nanodiamond. For this step, the tracking system employed in the previous section is used to monitor in real-time the ESR. Thus, one knows that the tip is close to the ND when the ESRs split effect is stronger. Once positioned over the diamond one can perform a magnetic image by scanning the microwire over micrometric sized regions. A spatial scan of the magnetic field due to the wire over 8 μm$\times$8 μm is shown in figure 27a. The pixel size is 190 nm$\times$190 nm, and an integration time per pixel of 1 s was used, resulting in a total scan time of 30 min. Figure 27a presents magnetic field gradients of approximately 24 μT/190 nm for a total field variation of 1000 μT. An image with a higher spatial resolution of the 4 μm$\times$4 μm region limited by dashed lines in figure 27a was also recorded, and the result can be seen in figure 27b. The total scan time was 58 min, and an integration time per pixel of 850 ms was used. Field gradients up to 13 μT/63 nm are observed for a total field variation of 800 μT, demonstrating that the system can measure magnetic fields with fairly high sensitivity and spatial resolution in the nanoscale. Just for comparison, the maximum magnetic field

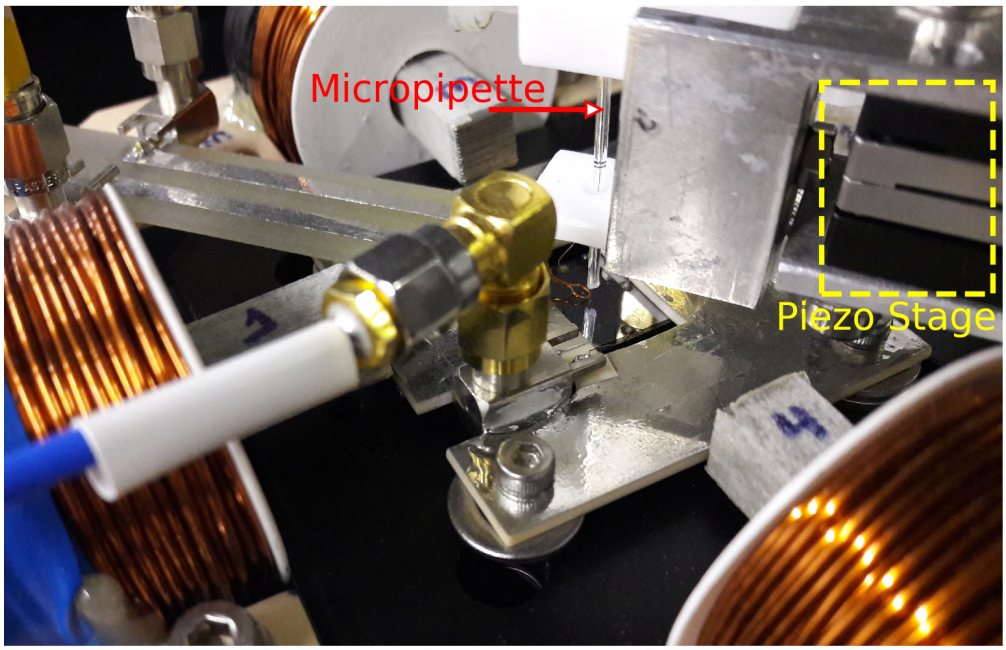

(a)

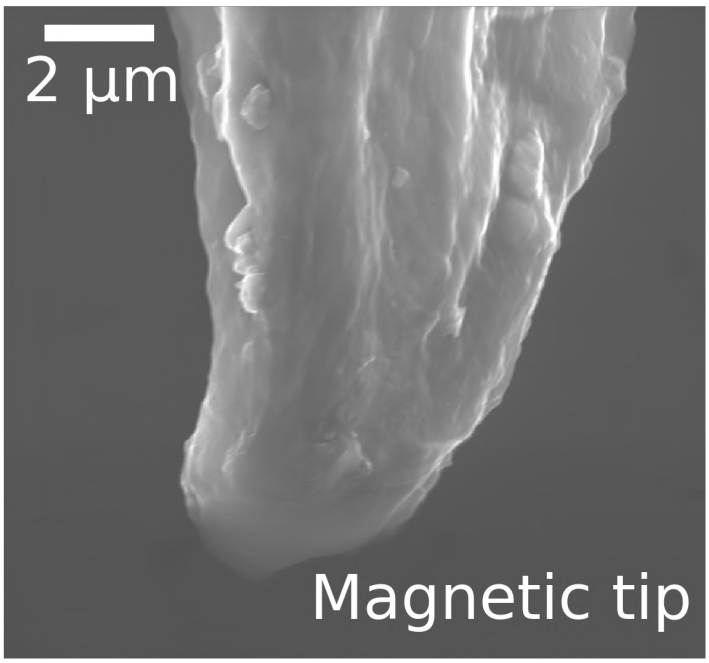

(b)

Figure 26: (a) Picture of the home-made tracking system and the XY-piezo (yellow dashed square) stage holding the micropipette with the magnetized steel microwire inserted in it. (b) Electron microscopic images of the magnetized tip used to perform magnetic imaging.

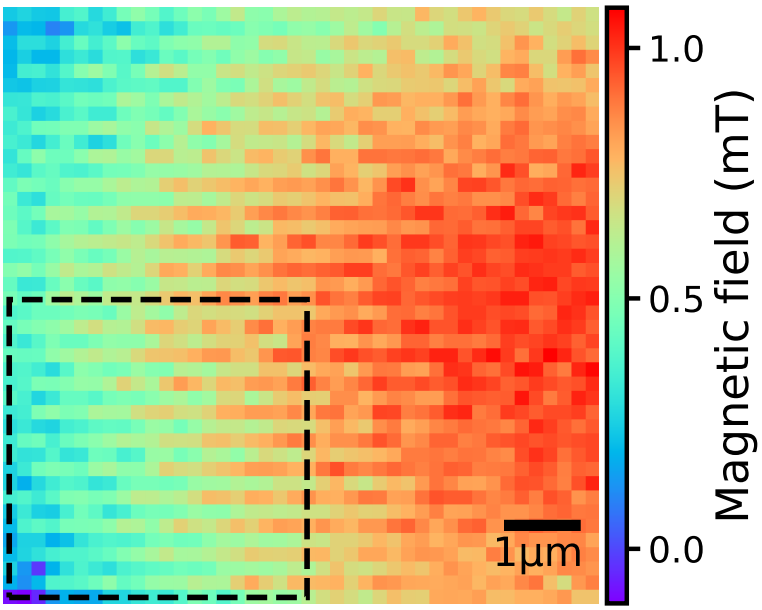

(a)

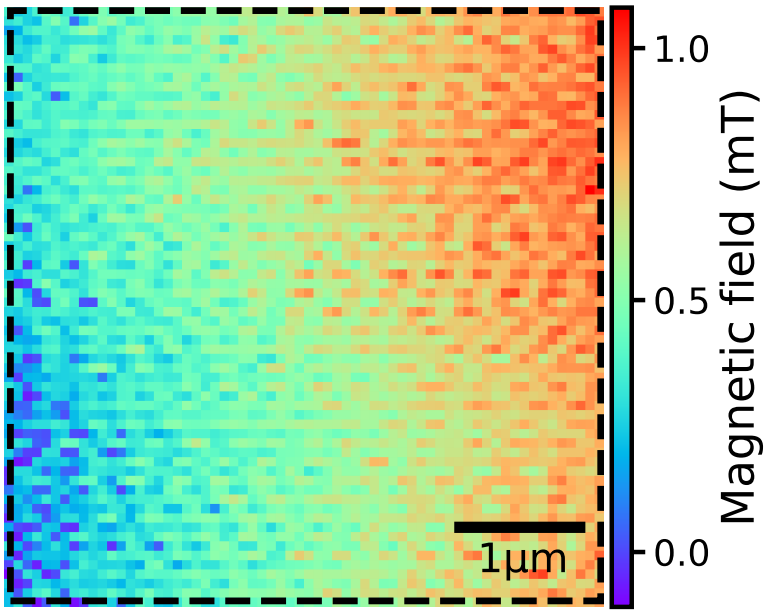

(b)

Figure 27: (a) Spatial maps of the magnetic field produced by the tip of a magnetized steel microwire. The spatial map (a) shows the scan over 8 μm $\times$ 8 μm region, while (b) contains the magnetic imaging field over a 4 μm $\times$ 4 μm region (dashed region in (a)). The magnetic field scale is the same for (a) and (b).

attained in a laser is about 10^{-10} T. For a laser emitting at 532 nm, the magnetic field amplitude goes from 0 to this maximum value at a distance of $\lambda/4$, which is ~ 133 nm. The resulting magnetic field gradient is thus 50 pT/66.5 nm. It is worth remarking that the spatial resolution of the developed system is roughly limited by the ND dimensions, such that it should still be possible to measure $\sim 2\times$ steeper magnetic field gradients than that investigated in the present work.

Chapter 5

Conclusion and perspectives

In this work, confocal scanning optical microscopy was used to detect NDs in microregions of a lithographically deposited MW antenna. These NDs proved to have an excellent photostability besides being single photon sources (with an average brightness of 3×10^4 counts/s) that can be shown by measuring the second order correlation function by HBT interferometry. For the ND used to perform all experiments described in this Thesis, the value found for $g^{(2)}(0)$ was of 0.1 indicating it as a single emitter since $0 < g^{(2)}(0) < 0.5$.

To evidence the properties of the paramagnetic ground state of the NV^- defect, the ODMR technique was employed to probe its spin states. The spectrum obtained agrees with the expectations for the general case, finding two ESR frequencies around the central frequency $D = 2.87$ GHz. For this experiment, it was found $2E = 7.2$ MHz. In order to detect external magnetic fields the NV^- symmetry axis orientation was also measured, resulting in $\theta = 4.8°$ and $\varphi = 15.8°$ for the NV^- symmetry axis of the chosen ND.

A nanomagnetometry system using a single NV^- defect in a ND was designed and characterized. The approach to optically track the electronic spin resonance frequencies of the NV^- center uses a single microwave source and the modulation of the ESR produced by a 10 kHz switched magnetic field. Several of the measurement tasks (photon counting, magnetic field switching, and error signal used for the tracking) were performed using home-made systems employing low-cost electronics (an Arduino Due board and an H-Bridge for the current modulation). The system exhibits magnetic field sensing capabilities

that are at the same order of magnitude of a state of the art single ND-based measurement systems under similar conditions, presenting a reasonable sensitivity and high spatial resolution, in the tens of nanometers range. This suggests that the present approach can be useful in the development of compact ND-based magnetometers. Moreover, this kind of magnetometers can be implemented without the requirement of highly sophisticated equipment, unlike others that need expensive apparatus (e.g SQUIDs) to reach cryogenic temperatures for its operation or atomic magnetometers that are not suitable to operate on the nanoscale. Several other features and capabilities for the presented system could be further integrated with the microcontroller and in peripheral electronics. For instance, it is possible to use the digital to analog outputs to drive a voltage controlled oscillator in the required MW range. In this way, the full control and detection system can fit the microcontroller board, which would allow the entire measurement system to reach construction volumes compatible with the cm^3 scale.

As a perspective, it is intended to explore another physical effect of the NV^- defect, the behavior of the spontaneous emission rate when the NV^- defect in ND interacting with a drop of liquid crystal (LC), which is an "intermediate" phase between liquid and solid crystal that exhibits unusual optical and electrical properties because of its anisotropic structure. This LC suffers a phase transition at a temperature of $\sim 44°C$ evidencing a change in the local density of optical states (LDOS) for the electromagnetic field. Thus, one wants to investigate the changes in the lifetime of the NV^- electronic excited state due to the changes in the LDOS and how it can be influenced by the relative orientation between the NV^- symmetry axis and the local LC molecular orientation.

References

[1] https://quotefancy.com/quote/1101/Richard-P-Feynman.

[2] F. Primdahl, "The fluxgate magnetometer." J. Phys. E: Sci. instr. **2**, 241 (1979).

[3] W. Viehmann, "Magnetometer based on the Hall effect." Rev. Sci. instrum. **33**, 537 (1962).

[4] A. Grosz, M. Haji-Sheikh and S. Mukhopadhyay, *High sensitivity magnetometers*. Switzerland: Springer, (2017).

[5] M. Buchner, K. Höfler, B. Henne, V. Ney and A. Ney, "Tutorial: Basic principles, limits of detection, and pitfalls of highly sensitive SQUID magnetometry for nanomagnetism and spintronics." J. Appl. Phys. **124**, 161101 (2018).

[6] R. Fagaly, "Superconducting quantum interference device instruments and applications.", Rev. Sci. Instrum. **77**, 101101 (2006).

[7] A. Dönszelmann, A. Baede, E. Overboom and J. Rozing, "A rubidium magnetometer using small vapour cells for homogeneity measurements." Appl. Sci. Res. **18**, 61 (1968).

[8] D. Grujic, A. Koss, G. Bison and A. Weis, "A sensitive and accurate atomic magnetometer based on free spin precession." Eur. Phys. J. D. **69**, 135 (2015).

[9] W. Chalupczak, R. Godun, S. Pustelny and W. Gawlik, "Room temperature femtotesla radio-frequency atomic magnetometer." Appl. Phys. Lett. **100**, 242401 (2012).

[10] K. Kominis, T. Kornack, J. Allred and M. Romalis, "A subfemtotesla multichannel atomic magnetometer." Nature **422**, 596 (2003).

[11] I. Savukov, "Ultra-Sensitive Optical Atomic Magnetometers and Their Applications." *Advances in Optical and Photonic Devices*, 329 (2010).

[12] F. Casola, T. van der Sar and A. Yacoby, "Probing condensed matter physics with magnetometry based on nitrogen vacancy centres in diamond." Nat. Rev. Mater. **3**, 1 (2018).

[13] N. Sadzak, M. Héritier and O. Benson, "Coupling a single nitrogen-vacancy center in nanodiamond to superparamagnetic nanoparticles." Sci. Rep. **8**, 8430 (2018).

[14] A. Boretti L. Rosa, J. Blackledge and S. Castelletto, "Nitrogen-vacancy centers in diamond for nanoscale magnetic resonance imaging applications." Beilstein J. Nanotechnol. **10**, 2128 (2019).

[15] G. Varvaro and F. Casoli, *Ultrahigh-Density Magnetic Recording: Storage Materials and Media Designs*. CRC Press (2016).

[16] E. Fullerton and J. Childress, "Spintronics, magnetoresistive heads, and the emergence of the digital world." Proc. IEEE **104**, 1787 (2016).

[17] K. Neuman and A. Nagy, "Single-molecule force spectroscopy: Optical tweezers, magnetic tweezers and atomic force microscopy." Nat. Methods **5**, 491 (2008).

[18] J. Lipfert, M. van Oene, M. Lee, F. Pedaci and N. Dekker, "Torque spectroscopy for the study of rotary motion in biological systems." Chem. Rev. **115**, 1449 (2015).

[19] P. Reineck, M. Capelli, D. Lau, J. Jeske, M. Field, T. Ohshima, A. Greentreea and B. Gibson, "Bright and photostable nitrogen-vacancy fluorescence from unprocessed detonation nanodiamond." Nanoscale **9**, 497 (2017).

[20] G. Balasubramanian, P. Neumann, D. Twitchen, M. Markham, R. Kolesov, N. Mizuochi, J. Isoya, J. Achard, J. Beck, J. Tissler, V. Jacques, R. Hemmer, F. Jelezko

and J. Wrachtrup, "Ultralong spin coherence time in isotopically engineered diamond." Nat. Mat. **8**, 383 (2009).

[21] N. Bar-Gil, L. Pham, A. Jarmola, D. Budker and R. Walsworth, "Solid-state electronic spin coherence time approaching one second." Nat. Commun. **4**, 1743 (2013).

[22] A. Dobrinets, *HPHT-treated diamonds*, Springer-Verlag Berlin An. (2016).

[23] P. Mandracci, *Chemical Vapor Deposition for Nanotechnology*. BoD-Books on Demand, (2019).

[24] T. Fukui, Y. Doi, T. Miyazaki, Y. Miyamoto, H. Kato, T. Matsumoto, T. Makino, S. Yamasaki, R. Morimoto and N. Tokuda, "Perfect selective alignment of nitrogen-vacancy centers in diamond." Appl. Phys. Exp. **7**, 055201 (2014).

[25] S. Hermelaar, P. de Boer, M. Chipaux, W. Zuidema, T. Hamoh, F. Martinez, A. Nagl, J. Hoogenboom, B. Giepmans and R. Schirhagl, "Nanodiamonds as multi-purpose labels for microscopy." Sci. Rep. **7**, 720 (2017).

[26] A. Beveratos, S. Kuehn, R. Brouri, T. Gacoin, J. Poizat and P. Grangier, "Room temperature stable single-photon source." Sci. Rep. **18**, 191 (2002).

[27] F. Jelezko, C. Tietz, A. Gruber, I. Popa, A. Nizovtsev, S. Kilin and J. Wrachtrup, "Spectroscopy of Single N-V Centers in Diamond." Single Mol. **2**, 255 (2001).

[28] M. Doherty, N. Manson, P. Delaney, F. Jelezko, J. Wrachtrup and L. Hollenberg, "The nitrogen-vacancy colour centre in diamond." Phys. Rep. **528**, 1 (2013).

[29] J. Chao, E. Perevedentseva, PH Chung, KK Liu, CY Cheng, CC Chang and CL Cheng, "Nanometer-sized diamond particle as probe for biolabeling." Biophys. J. **93**, 2199 (2007).

[30] D. Sage, K. Arai, D. Glenn, S. DeVience, L. Pham, L. Rahn-Lee, M. Lukin, A. Yacoby, A. Komeili and R. Walsworth, "Optical magnetic imaging of living cells." Nature **496**, 486 (2013).

[31] V. Acosta and P. Hemmer, "Nitrogen-vacancy centers: Physics and applications." MRS bulletin **38**, 127 (2013).

[32] P. Neuman, R. Kolesov, V. Jacques, J. Beck, J. Tisler, A. Batalov, L. Rogers, N. Manson, G. Balasubramanian and F. Jelezko, "Excited-state spectroscopy of single NV defects in diamond using optically detected magnetic resonance." New J. Phys. **11**, 013017 (2009).

[33] Y. Matsuzaki, H. Morishita, T. Shimooka, T. Tashima, K. Kakuyanagi, K. Semba, W. Munro, H. Yamaguchi, N. Mizuochi and S. Saito, "Optically detected magnetic resonance of high-density ensemble of NV centers in diamond." J. Phys.: Condens. Matter **28**, 275302 (2016).

[34] Z. Ma, S. Zhang, Y. Fu, H. Yuan, Y. Shi, J. Gao, L. Qin, J. Tang, J. Liu, and Y. Li, "Magnetometry for precision measurement using frequency-modulation microwave combined efficiency photon collection technique on an ensemble of nitrogen-vacancy centers in diamond." Opt. Exp. **26**, 382 (2018).

[35] J. Webb, J. Clement, L. Troise, S. Ahmadi, G. Johansen, A. Huck and U. Andersen, "Nanotesla sensitivity magnetic field sensing using a compact diamond nitrogen-vacancy magnetometer." Appl. Phys. Lett. **114**, 231103 (2019).

[36] R. Schoenfeld and W. Harneit, "Real time magnetic field sensing and imaging using a single spin in diamond." Phys. Rev. Lett. **106**, 030802 (2011).

[37] F. Stürner, A. Brenneis, J. Kassel, U. Wostradowski, R. Rölver, T. Fuchs, K. Nakamura, H. Sumiya, S. Onoda, J. Isoya and F. Jelezko, "Compact integrated magnetometer based on nitrogen-vacancy centres in diamond." Diamond Relat. Mater. **93**, 50 (2019).

[38] R. Schirhagl, K. Chang, M. Loretz and C. Degen, "Nitrogen-Vacancy centers in diamond: nanoscale sensors for physics and biology." Annu. Rev. Phys. Chem. **65**, 83 (2014).

[39] A. Erdemir and C. Donnet, "Tribology of diamond-like carbon films: recent progress and future prospects." J. Phys. D: Appl. Phys. **39**, R311 (2006).

[40] N. Yang, *Novel Aspects of Diamond: From Growth to Applications*. Second Edition. Springer, (2019).

[41] J. Walker, "Optical absorption and luminescence in diamond." Rep. Prog. Phys. **42**, 108 (1979).

[42] F. Jelezko and J. Wrachtrup, "Single defect center in diamond: A review." Phys. Stat. Sol. (a) **203**, 3207 (2006).

[43] L. Childress and R. Hanson, "Diamond NV centers for quantum computing and quantum networks." MRS bulletin **38**, 134 (2013).

[44] A. Sajid, M. Ford and J. Reimers, "Single-photon emitters in hexagonal Boron Nitride: A review of progress." Rep. Prog. Phys. **83**, 044501 (2020).

[45] N. Mizuochi, T. Makino, H. Kato, D. Takeuchi, M. Ogura, H. Okushi, M. Nothaft, P. Neumann, A. Gali, F. Jelezko, J. Wrachtrup and S. Yamasaki, "Electrically driven single-photon source at room temperature in diamond." Nat. Photon **6**, 299 (2012).

[46] M. Jason, S. Meynell , A. Jayich and J. Meijer, "Colour centre generation in diamond for quantum technologies." Nanophotonics **8**, 1889 (2019).

[47] K. Bogdanov, M. Zhukovskaya, V. Osipov, E. Ushakova, M. Baranov, K. Takai, A. Rampersaud, and A. Baranov, "Highly intensive emission of the NV^- centers in synthetic HPHT microdiamonds at low nitrogen doping." APL Mater. **6**, 086104 (2018).

[48] T. Chakraborty, F. Lehmann, J. Zhang, S. Borgsdorf, N. Wöhrl, R. Remfort, V. Buck, U. Köhler, and D. Suter, "CVD growth of ultrapure diamond, generation of NV centers by ion implantation, and their spectroscopic characterization for quantum technological applications." Phys. Rev. Mat. **3**, 065205 (2019).

[49] A. Haque and S. Sumaiya, "An overview on the formation and processing of nitrogen-vacancy photonic centers in diamond by ion implantation." J. Manuf. Mater. Process. **1**, 1 (2017).

[50] F. Alghannam and P. Hemmer, "Engineering of shallow layers of nitrogen vacancy colour centres in diamond using plasma immersion ion implantation." Sci. Rep. **9**, 5870 (2019).

[51] W. Zhang, J. Zhang, J. Wang, F. Feng, S. Lin, L. Lou, W. Zhu, and G. Wang, "Depth-dependent decoherence caused by surface and external spins for NV centers in diamond." Phy. Rev. B **96**, 235443 (2017).

[52] G. Duffey, *Modern Physical Chemistry: A Molecular Approach.* Kluwer Academic, (2000).

[53] A. Gali, "Ab initio theory of the nitrogen-vacancy center in diamond." Nanophotonics **8**, 1907 (2015).

[54] A. Lenef and S. Rand, "Electronic structure of the N-V center in diamond: Theory." Phys. Rev. B **53**, 441 (1996).

[55] J. Maze, A. Gali, E. Togan, Y. Chu, A. Trifonov, E. Kaxiras and M. Lukin, "Properties of nitrogen-vacancy centers in diamond: the group theoretic approach." New J. Phys. **13**, 025025 (2011).

[56] M. Doherty, N. Manson, P. Delaney and L. Hollenberg, "The negatively charged nitrogen-vacancy centre in diamond: the electronic solution." Phys. Rev. B **13**, 025019 (2011).

[57] M. Doherty, F. Dolde, H. Fedder, F. Jelezko, J. Wrachtrup, N. Manson, and L. Hollenberg, "Theory of the ground-state spin of the NV center in diamond." Phys. Rev. B **85**, 205203 (2012).

[58] S. Hong, M. Grinolds, L. Pham, D. Le Sage, L. Luan, R. Walsworth and A. Yacoby, "Nanoscale magnetometry with NV centers in diamond." MRS bulletin **38**, 155 (2013).

[59] F. Poggiali, P. Cappellaro, and N. Fabbri, "Measurement of the excited-state transverse hyperfine coupling in NV centers via dynamic nuclear polarization." Phys. Rev. B **95**, 195308 (2017).

[60] N. Manzon, J. Harrison, and M. Sellars, "Nitrogen-vacancy center in diamond: Model of the electronic structure and associated dynamics." Phys. Rev. B **74**, 104303 (2006).

[61] M. Goldman, M. Doherty, A. Sipahigil, N. Yao, S. Bennett, N. Manson, A. Kubanek, and M. Lukin, "State-selective intersystem crossing in nitrogen-vacancy centers." Phys. Rev. B **91**, 165201 (2015).

[62] M. Acosta, A. Jarmola, E. Bauch, and D. Budker, "Optical properties of the nitrogen-vacancy singlet levels in diamond." Phys. Rev. B **82**, 201202 (2010).

[63] J. Harrison, M. Sellars and N. Manson, "Optical spin polarization of the N-V centre in diamond." J. Lumin. **107**, 245 (2004).

[64] L. Gang-Quin and P. Xin-Yu, "Quantum information processing with nitrogen–vacancy centers in diamond." Chin. Phys. B **27**, 020304 (2018).

[65] J. Taylor, P. Cappellaro, L. Childress, L. Jiang, D. Budker, P. Hemmer, A. Yacoby, R. Walsworth and M. Lukin, "High-sensitivity diamond magnetometer with nanoscale resolution." Nat. Phys. **4**, 810 (2008).

[66] G. Balasubramanian, I. Chan, R. Kolesov, M. Al-Hmoud, J. Tisler, C. Shin, C. Kim, A. Wojcik, P. Hemmer, A. Krueger, T. Hanke, A. Leitenstorfer, R. Bratschitsch, F. Jelezko and J. Wrachtrup, "Nanoscale imaging magnetometry with diamond spins under ambient conditions." Nature **455**, 648 (2008).

[67] C. Degen, "Scanning magnetic field microscope with a diamond single spin sensor." App. Phys. Lett. **92**, 243111 (2008).

[68] L. Rondin, J. Tetienne, T. Hingant, J. Roch, P. Maletinsky and V. Jacques, "Magnetometry with nitrogen-vacancy defects in diamond." Rep. Prog. Phys. **77**, 056503 (2014).

[69] R. Hanson, O. Gywat, and D. Awschalom, "Room-temperature manipulation and decoherence of a single spin in diamond." Phys. Rev. B **74**, 161203 (2006).

[70] M. Barbiero, S. Castelletto, X. Gan and M. Gu, "Spin-manipulated nanoscopy for single nitrogen-vacancy center localizations in nanodiamonds." Light: Sci. & Applic. **6**, e17085 (2017).

[71] J. Wrachtrup, C. von Borczyskowski, J. Bernard, M. Orrit and R. Brown , "Optical detection of magnetic resonance in a single molecule." Nature **363**, 244 (1993).

[72] A. Lund and M. Shiatoni, *EPR of free radicals in solids: Trends in method and applications.* Springer-Science (2003).

[73] D. Kane, A. Micolich, and J. Rabeau, *Nanothecnology in Australia: Showcase of early career research.* Taylor & Francis group, LCC (2011).

[74] P. Robert, "Ultra Diamond from Pure Carbon-12." Science **249**, 4964 (1990).

[75] E. Levine, M. Turnera, P. Kehayias, C. Hart, N. Langellier, R. Trubko, D. Glenn, R. Fu and R. Walsworth, "Principles and techniques of the quantum diamond microscope." Nanophotonics **8**, 1945 (2019).

[76] H. zheng, J. Xu, G. Iwata, T. Lenz, J. Michl, B. Yavkin, K. Nakamura, H. Sumiya, T. Ohshima, J. Isoya, J. Wrachtrup, A. Wickenbrock, and D. Budker, "Zero-field magnetometry based on nitrogen-vacancy ensembles in diamond." Phys. Rev. App. **11**, 064068 (2019).

[77] A. Blom, "Exact Solution of the Zeeman Effect in Single-Electron Systems." Phys. Scr. **2005**, 90 (2005).

[78] A. Boretti and S. Castelletto, "Nanometric resolution magnetic resonance imaging methods for mapping functional activity in neuronal networks." MethodX **3**, 297 (2016).

[79] L. Rondin, Réalisation d'un magnétomètre à centre coloré NV du diamant. Thèse, École Normale Supérieure de Cachan, November (2012).

[80] R. Horowitz, J. Alemán, J. Christle, N. Cleland, and D. Awschalom "Electron spin resonance of nitrogen-vacancy centers in optically trapped nanodiamonds." Proc. Natl. Acad. Sci. **109**, 13493 (2012).

[81] A. Dréau, M. Lesik, L. Rondin, P. Spinicelli, O. Arcizet, J. Roch, and V. Jacques, "Avoiding power broadening in optically detected magnetic resonance of single NV defects for enhanced DC-magnetic field sensitivity." Phys. Rev. B **84**, 195204 (2011).

[82] E. Sánchez, Optically detected magnetic resonance in nanodiamonds with single nitroge-vacancy defects. Dissertation, Universidade Federal de Pernambuco, April (2016).

[83] L. Pahm, Magnetic Field Sensing with Nitrogen-Vacancy Color Centers in Diamond. Thesis, Harvard University, May (2013).

[84] P. Maletinsky, S. Hong, M. Grinolds, B. Hausmann, M. Lukin, R. Walsworth, M. Loncar and A. Yacoby, "A robust scanning diamond sensor for nanoscale imaging with single nitrogen-vacancy centres." Nat. Nanotech. **7**, 320 (2012).

[85] J. Maze, P. Stanwix, J. Hodges, S. Hong, J. Taylor, P. Cappellaro, L. Jiang, M. Dutt, E. Togan, A. S. Zibrov, A. Yacoby, R. Walsworth and M. Lukin, "Nanoscale magnetic sensing with an individual electronic spin in diamond." Nature **455**, 644 (2008).

[86] Zhi-Hui Wang, G. de Lange, D. Riste, R. Hanson and V. Dobrovitski, "Comparison of dynamical decoupling protocols for a nitrogen-vacancy center in diamond." Phys. Rev. B **85**, 155204 (2012).

[87] J. Shim, I. Niemeyer, J. Zhang and D. Suter, "Robust dynamical decoupling for arbitrary quantum states of a single NV center in diamond." Europhys. Lett. **99**, 40004 (2012).

[88] https://www.arduino.cc/ (accessed on 17th April, 2020)

[89] B. Luonis and M. Orrit, "Single-photon sources." Rep. Prog. Phys. **68**, 1129 (2005).

[90] P. Grünwald, "Effective second-order correlation function and single-photon detection." New J. Phys. **21**, 093003 (2019).

[91] M. Nothaft, S. Höhla, F. Jelezko, N. Frühauf, J. Pflaum and J. Wrachtrup, "Electrically driven photon antibunching from a single molecule at room temperature." Nat. Commun. **3**, 1 (2012).

[92] E. Suarez, D. Auwärter, T. Arruda, R. Bachelard, P. Courteille, C. Zimmermann and S. Slama, "Photon-antibunching in the fluorescence of statistical ensembles of emitters at an optical nanofiber-tip." New J. Phys. **21**, 035009 (2019).

[93] K. Jensen, V. Acosta, A. Jarmola, and D. Budker, "Light narrowing of magnetic resonances in ensembles of nitrogen-vacancy centers in diamond." Phys. Rev. B **87**, 014115 (2013).

[94] M. Mrozek, A. Wojciechowski, D. Rudnicki, J. Zachorowski, P. Kehayias, D. Budker, and W. Gawlik, "Coherent population oscillations with nitrogen-vacancy color centers in diamond." Phys. Rev. B **94**, 035204 (2016).

[95] A. Zaitev, *Optical porperties of diamond.* Springer-Verlag (2001).

[96] A. Gruber, A. Dräbenstedt, C. Tietz, L. Fleury, J. Wrachtrup and C. von Borczyskowski, "Scanning Confocal Optical Microscopy and Magnetic Resonance on Single Defect Centers." Science **276**, 2012 (1997).

[97] H. Zhang, C. Belvin, W. Li, J. Wang, J. Wainwright, R. Berg and J. Bridger, "Little bits of diamond: Optically detected magnetic resonance of nitrogen-vacancy centers." Am. J. Phys. **86**, 225 (2018).

[98] https://en.wikipedia.org/wiki Schmitt_trigger. (accessed on 17th April, 2020)

[99] http://ww1.microchip.com/downloads/en/DeviceDoc/Atmel-11057-32-bit-Cortex-M3-Microcontroller-SAM3X-SAM3A_Datasheet.pdf (accessed on 17th April, 2020)

[100] M. Fox. Quantum Optics: An introduction. 1st ed. Oxford University Press, 2006.

[101] R. Hambury-Bron and Twins "Correlation between photons in two coherent beams of light." Nature **177**, 27 (1956).

[102] R. Hambury-Bron and Twins "A test of a new type of stellar interferometer on Sirius." Nature **178**, 1046 (1956).

[103] R. Loudon. The Quantum Theory of Light. 2nd ed. Oxford Science Publications; Oxford University Press, 1983.

Appendix A

Microcontroller: design and operation

The Arduino microcontroller used in this experiment is of central importance, because it makes the tasks of information acquisition and control of the different essential devices by detection of magnetic fields, which is the aim of the present work. Thus, in the following details about the electronic circuit and the implemented software to build the operation system of the magnetometer will be shown.

In the process of developing the electronic system for the magnetometer, it is important that the output signal amplitude from the APD (2.2 V) be compatible with the digital input of Arduino Due (3.3 V). The operational sequence of the electronic circuit seen in figure 28 is the following: An APD pulse activates a transistor which operates like a switch to charge the capacitor C1 and activate a comparator known as Schmitt trigger [98]. After a characteristic rise time (10 ns) of the APD signal, the capacitor discharges in a RC time, where R is an equivalent resistance between R1 and R5. Then, the voltage decays exponentially to zero. Trimpot R5 operates as a pulse width adjustment. Thus, the circuit can adjust the amplitude and the pulse width.

Pulse signals coming from the APD are treated as digital counts. Then, a program written in C++ counts the APD pulses with a temporal resolution determined by the clock of the

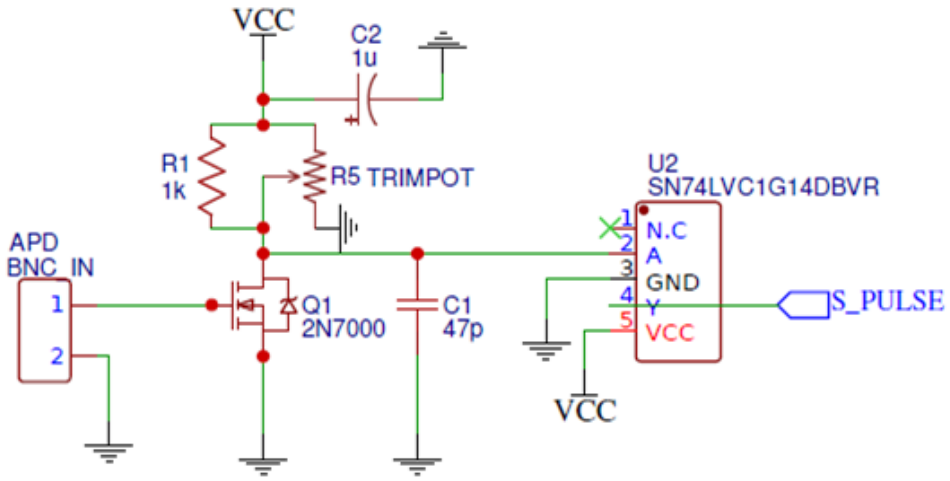

Figure 28: Scheme depicting the electronic circuit employed to adapt the signal amplitude from the APD, so that it reaches a suitable signal amplitude allowed for the digital input of the Arduino board.

Arduino Due (84 MHz). The program also has a routine to synchronize the signal from the APD with the MW signal and the magnetic field modulation signal (see figure 29).

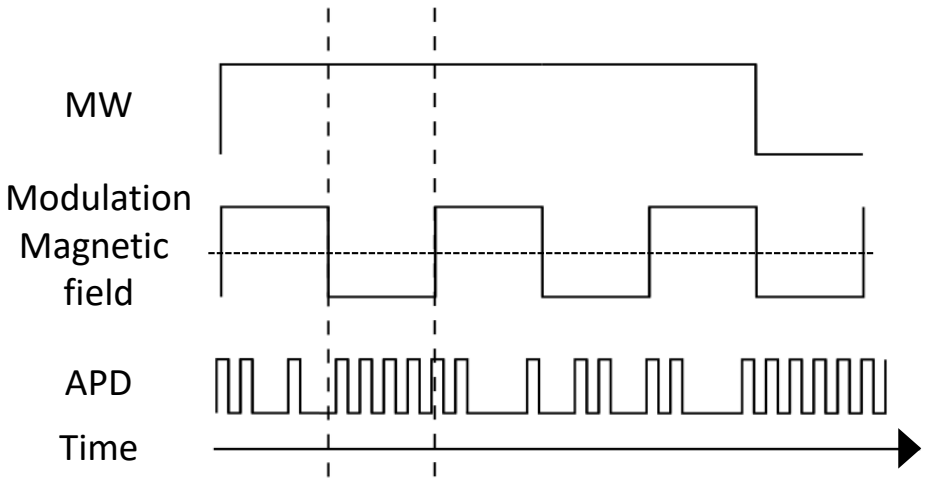

Figure 29: Pulse sequences created in Arduino to generate a modulated magnetic field synchronous with the MW signal .

Besides, by making use of its versatility it is possible to write an algorithm to create a digital filter to smooth the data in real time:

```
///FILTRO SAVITZKY-GOLAY - ORDEM 1
float coef[N]= {0.09090909,0.09090909,0.09090909,0.09090909,0.09090909
,0.09090909,0.09090909,0.09090909,0.09090909,0.09090909,0.09090909};
float soma1 = 0;
float soma2 = 0;
for(int i=0; i< N-1; i++){
  odmr_buffer_total_pos[i]=odmr_buffer_total_pos[i+1];
  odmr_buffer_total_neg[i]=odmr_buffer_total_neg[i+1];
}
  odmr_buffer_total_pos[N-1]=total_pos;
  odmr_buffer_total_neg[N-1]=total_neg;
for(int j=0; j< N; j++){
  soma1 += coef[j] * odmr_buffer_total_pos[j];
  soma2 += coef[j] * odmr_buffer_total_neg[j];
}
odmr_buffer_total_pos[int((N-1)/2)]=soma1;
odmr_buffer_total_pos[int((N-1)/2)]=soma2;
```

One of the digital ports in connection with the APD is configured in the counts internal mode with the highest possible speed (42 MHz). The data information is recorded in the internal memory buffer of the microcontroller. A signal trigger of the MW generator activates an interrupt routine, which redirects counts for a different buffer that allows to distinguish when MW signal is in ON or OFF. Moreover, Arduino also controls the modulation signal of the current, allowing to allocate photon counts in case when the current is positive or negative. Then, when data are collected a Savitzky-Golay digital filter is used to improve the quality of the signal and subsequently improve the tracking control. Details about programming in the Arduino board can be found in [99].

The photon counts are performed by a channel of the Timer Counter (TC) module, as can be reviewed in the page 856 of Arduino's microcontroller datasheet [99]. Code for the configuration of the counter is given by

```
PCM->PCM_PCER0 = PCM_PCER0_PID27;
TC0->TC_CHANNEL[0].TC_CCR = TC_CCR_CLKDIS;
TC0->TC_CHANNEL[0].TC_CMR = TC_CMR_CLKDIS_XC0;
TC0->TC_BMR = TC_BMR_TC0XC0S_TCLK0;
```

and the counter routine is

```
void Counter_Mode(){
  //pwml(84,42);
  int intervalos = 1;
  tempo = 100; // milliseconds
  wind32_t contagem = 0;
  TC0->TC_CHANNEL[0].TC_CV = 0;
  TC0->TC_CHANNEL[0].TC_CCR = TC_CCR_SWTRG
                            | TC_CCR_CLKEN;
    delay(tempo);
    contagem = TC0->TC_CHANNEL[0].TC_CV;
  Serial.print("A");
  Serial.println(contagem/intervalos);
 }
```

The channel TC0->TC_CHANNEL[0] initializes the pulse counting from the pin 22 and saves the counts in a internal buffer. It is possible to access this channel by using the TC0→TC_CHANNEL[0] →TC_CV command. At the beginning of the routine the counter is reset before to enable the counting, then it waits a time (delay) until it gets the value in the buffer. To reach a lower temporal resolution, functions can be used, as `delaymicroseconds`, or even a function can be created to give some clock cycles using the command `for` as a volatile variable. With this, the system can reach up to 400 ns of temporal resolution.

Another routine enabled during the ODMR sequence that is used separate the counts when MW frequency is in ON or OFF is written as the following code

```
void Counter_Mode(){
  int intervalos = 50;
  long total_A = 0;
  long total_B = 0;
  volatile unit32_t contagem1 [50];
  volatile unit32_t contagem2 [50];
  volatile unit32_t zero = 0;
  TC0->TC_CHANNEL[0].TC_CV = 0;
  TC0->TC_CHANNEL[0].TC_CCR = TC_CCR_SWTRG
                            | TC_CCR_CLKEN;

  while((PIOB->PIO_PDSR >> 25) & 1 ==0){}
  while((PIOB->PIO_PDSR >> 25) & 1 ==1){}
  long a = millis();
  for(int i=0; 1<intervalos;i++){

    zero = TC0->TC_CHANNEL[0].TC_CV;)
    while(((PIOB->PIO_PDSR >> 25) & 1 ==0){ }
    contagem1[i] = TC0->TC_CHANNEL[0].TC_CV-zero;
    zero = TC0->TC_CHANNEL[0].TC_CV;
    while(((PIOB->PIO_PDSR >> 25) & 1) ==1){ }
    contagem2[i] = TC0->TC_CHANNEL[0].TC_CV-zero;
 }
```

The register PIOB→PIO_PDSR >> 25 verifies whether the pin is receiving voltage, which means that MW signal is in ON. Moreover, as control device the microcontroller has several analog and digital inputs and outputs that allow communication with other equipment.

For modulation of magnetic fields it is designed a bipolar current source, a so-called H-Bridge, which is an electronic circuit that switches the polarity of the current making it possible generate a modulated magnetic field. The chosen frequency to switch the equipment is 10 kHz with a maximun current of 500 mA. A LVTTL (3.3 V Low-Voltage

TTL) pulse of $\sim$ 500 ns generated by the Arduino's microcontroller allows to change the direction of the current. The code that allows to modulate the magnetic field is the following:

```
while(((PIOB->PIO_PDSR >> 25) & 1)==0){
  ATOMIC(){
  //MANDA UM PULSO DE 500== ns
  PIOC->PIO_SODR = (1<<22);
  noIntDelayUs(2);
  PIOC->PIO_CODR = (1<<22);
  zero = TC0->TC_CHANNEL[0].TC_CV;
  noIntDelayUs(delaytime_us);
  contagem1A[i] = TC0->TC_CHANNEL[0].TC_CV-zero;

  //MANDA UM PULSO DE 500== ns
  PIOC->PIO_SODR = (1<<22);
  noIntDelayUs(2);
  PIOC->PIO_CODR = (1<<22);
  zero = TC0->TC_CHANNEL[0].TC_CV;
  noIntDelayUs(delaytime_us);
  contagem2A[i] = TC0->TC_CHANNEL.TC_CV-zero;
  }
}
```

Code done in IDE language

This program performs the counting of square wave peaks in time intervals of the order of microseconds. Moreover, it is used to performs magnetometry experiments.

```
#Include<SimplyAtomic.h>
```

```
typedef struct {
  String conteudo;
  volatile uint16_t valor[2];
}ComSerial;

uint16_t integra = 100; // INTEGRATION TIME
uint16_t freq = 10; // FERQUENCY TO SWITCHING THE CURRENT (kHz)
unsigned int mode = 0; //0 = COUNTER ; 1 = PLL ; 2 = ODMR
bool state=0;

const int N=11; // SAMPLING RATE OF THE FILTER
float odmr_buffer_total_pos[N]; // BUFFERS FOR THE FILTER
float odmr_buffer_total_neg[N];
float pll_buffer[N];

void setup(){

  for(int i=0;i<N;i++){
  odmr_buffer_total_pos[i]=0;
  odmr_buffer_total_neg[i]=0;
  pll_buffer[i]=0;
  }

Serial.begin(115200);
  pinMode(2,INPUT);
  pinMode(8,OUTPUT);
  pinMode(4,OUTPUT);

  PMC->PMC_PCER0 = PMC_PCER0_PID27;    // interrupt line TC0 selected -
                                          enables the control of voltage
  TC0->TC_CHANNEL[0].TC_CCR = TC_CCR_CLKDIS ;    // counter clock
```

```
                                                disabled for initialization
  TC0->TC_CHANNEL[0].TC_CMR = TC_CMR_TCCLKS_XC0;  // counter clock
                                                    selected : XC0
  TC0->TC_BMR = TC_BMR_TC0XC0S_TCLK0;   // signal connected to XC0:
                                    TCLK0=PB26=Arduino_Due_Digital_Pin_22
}

void pwm1(uint16_t value, uint16_t duty){
  // GERADOR DE ONDA: PINO DIGITAL 7
  int32_t mask_PWM_pin = digitalPinToBitMask(7);
  REG_PMC_PCER1 = 1<<4;              // activate clock for PWM controller
  REG_PIOC_PDR |= mask_PWM_pin;      // activate peripheral functions for
                                        pin (disables all PIO functionality)
  REG_PIOC_ABSR |= mask_PWM_pin;     // choose peripheral option B
  REG_PWM_CLK = 0;                   // choose clock rate, 0 -> full MCLK
                                        as reference 84MHz
  REG_PWM_CMR6 = 0<<9;               // select clock and polarity for PWM
                                        channel (pin7) -> (CPOL = 0)
  REG_PWM_CPRD6 = value;      // initialize PWM period -> T = value/84MHz
                                 (value: up to 16bit),EX. value=4 -> 21 MHz
  REG_PWM_CDTY6 = duty;       // initialize duty cycle, REG_PWM_CPRD6
  REG_PWM_ENA = 1<<6;         // enable PWM on PWM channel (pin 7 = PWML6)
}

void pwm2(uint16_t value, uint16_t duty){ //(DISABLED)
  // WAVE GENERATOR: PINO DIGITAL 8
  int32_t mask_PWM_pin2 = digitalPinToBitMask(8);
  REG_PMC_PCER1 = 1<<4;               // activate clock for PWM controller
  REG_PIOC_PDR |= mask_PWM_pin2;      // activate peripheral functions for
                                         pin (disables all PIO functionality)
  REG_PIOC_ABSR |= mask_PWM_pin2;    // choose peripheral option B
```

```
  REG_PWM_CLK = 0;        // choose clock rate, 0 -> full MCLK as reference
                             84MHz
  REG_PWM_CMR5 = 0<<9;    // select clock and polarity for PWM channel
                             (pin8) -> (CPOL = 0)
  REG_PWM_CPRD5 = value;  // initialize PWM period -> T = value/84MHz
                             (value: up to 16bit),EX. value=84 -> 1 MHz
  REG_PWM_CDTY5 = duty;   // initialize duty cycle, REG_PWM_CPRD6 / value
  REG_PWM_ENA = 1<<5;     // enable PWM on PWM channel (pin 8 = PWML5)
}

ComSerial LerSerial() {
    ComSerial aux;
    char numero[10];
    char *eprt;
    int ascii;
    int i=0, j=0, l=0;

    while(Serial.available()>0) {
      ascii=Serial.peek();
      //Serial.println(ascii);
      if(ascii != 13) {
        if (ascii > 47 && ascii < 58) {
          delay(50);
            do {
              numero[i]= Serial.read();
              ascii = Serial.peek();
              i++;
            } while (ascii > 47 && ascii < 58);

          i=0;
          long int var = strtol(numero,&eprt,10);
```

```
            aux.valor[j] = var;

            for (int k=0; k<10;k++){
              numero[k]=0;
            }
            j++;
          }
          else {
            char carac = Serial.read();
            if (carac > 96 && carac < 123){
              carac -= 32;
            }
            aux.conteudo.concat(carac);
          }
        }
        delay(10);//VERIFICAR
      }
      return aux;
}

void noIntDelayUs(uint32_t cycles){
  volatile uint32_t j;
  for(j=0;j<cycles;j++){}
}

void Counter_Mode(){
  uint32_t contagem = 0;

  unsigned long timeout = 84000000; // 1s max for the next clock pulse
  unsigned long k=0;
  unsigned long zero;  // Ver pag. 862, 36.6.6 (Trigger) no manual do SAM3X
```

```
  TC0->TC_CHANNEL[0].TC_CCR = TC_CCR_SWTRG        // sowftware trigger:
                                                  // reset counter, start
                                                  // clock
                            | TC_CCR_CLKEN;       // counter clock enabled
  zero = TC0->TC_CHANNEL[0].TC_CV;
  while((TC0->TC_CHANNEL[0].TC_CV == zero)&&(k<timeout)){
    k++;
  }
  delay(integra);
  contagem = TC0->TC_CHANNEL[0].TC_CV;
  Serial.print("A");
  Serial.println(int(contagem));
}

void PLL_Mode(){

  int intervalos = int((integra)/2);

  long total_A1=0;
  long total_B1=0;
  long total_A2=0;
  long total_B2=0;

  uint16_t tempo = int((1./freq)*(1000/2)); //MEIO PERIODO DA CORRENTE

  volatile uint32_t contagem1A [intervalos];
  volatile uint32_t contagem2A [intervalos];
  volatile uint32_t contagem1B [intervalos];
  volatile uint32_t contagem2B [intervalos];
  volatile uint32_t zero0 = 0;
```

```
int cnt1=0;
int cnt2=0;

for(int i=0;i<intervalos;i++){
  contagem1A[i] = 0;
  contagem2A[i] = 0;
  contagem1B[i] = 0;
  contagem2B[i] = 0;
}

// ZERAMENTO DO CONTADOR
unsigned long timeout = 84000000; // 1s max for the next clock pulse
unsigned long k=0;
unsigned long zero;    // Pag. 862, 36.6.6 (Trigger) no manual do SAM3X
TC0->TC_CHANNEL[0].TC_CCR = TC_CCR_SWTRG     // sowftware trigger: reset
                                                counter, start clock
                          | TC_CCR_CLKEN; // counter clock enabled
zero = TC0->TC_CHANNEL[0].TC_CV;
while((TC0->TC_CHANNEL[0].TC_CV == zero)&&(k<timeout)){
  k++;
}

while((PIOB->PIO_PDSR >> 25 ) & 1 == 0){}
while((PIOB->PIO_PDSR >> 25 ) & 1 == 1){}    // Aguardar fase com o sinal

for(int i=0;i<intervalos;i++){
  while(((PIOB->PIO_PDSR >> 25 ) & 1)==0){    //ciclo negativo da RF
    //MANDA UM PULSO DE 500 ns
    PIOC->PIO_SODR = (1<<22); //set C22/Pin8 high
    noIntDelayUs(2); // approx 500 ns
    PIOC->PIO_CODR = (1<<22); //set C22/Pin8 low
```

```
    zero0 = TC0->TC_CHANNEL[0].TC_CV;
    delayMicroseconds(tempo);
    contagem1A[i] += TC0->TC_CHANNEL[0].TC_CV-zero0;    //leitura do
                                        // registrador do TC0 - canal 0

    //MANDA UM PULSO DE 500 ns
    PIOC->PIO_SODR = (1<<22); //set C22/Pin8 high
    noIntDelayUs(2); // approx 500 ns
    PIOC->PIO_CODR = (1<<22); //set C22/Pin8 low

    zero0 = TC0->TC_CHANNEL[0].TC_CV;
    delayMicroseconds(tempo);
    contagem2A[i] += TC0->TC_CHANNEL[0].TC_CV-zero0;
    cnt1++;
  }
  while(((PIOB->PIO_PDSR >> 25 ) & 1)==1){     //ciclo positivo da RF
    //MANDA UM PULSO DE 500 ns
    PIOC->PIO_SODR = (1<<22); //set C22/Pin8 high
    noIntDelayUs(2); // approx 500 ns
    PIOC->PIO_CODR = (1<<22); //set C22/Pin8 low

    zero0 = TC0->TC_CHANNEL[0].TC_CV;
    delayMicroseconds(tempo);
    contagem1B[i] += TC0->TC_CHANNEL[0].TC_CV-zero0;    //leitura do
                                        // registrador do TC0 - canal 0

    //MANDA UM PULSO DE 500 ns
    PIOC->PIO_SODR = (1<<22); //set C22/Pin8 high
    noIntDelayUs(2); // approx 500 ns
    PIOC->PIO_CODR = (1<<22); //set C22/Pin8 low
```

```
      zero0 = TC0->TC_CHANNEL[0].TC_CV;
      delayMicroseconds(tempo);
      contagem2B[i] += TC0->TC_CHANNEL[0].TC_CV-zero0;
      cnt2++;
    }
  }

  for (int i=0;i<intervalos;i++){ //Take the differences
    if((contagem1A[i]!=0)&&(contagem2A[i]!=0)&&(contagem1B[i]!=0)&&
    (contagem2B[i]!=0)){
    total_A1 += (contagem1A[i]);
    total_A2 += (contagem2A[i]);
    total_B1 += (contagem1B[i]);
    total_B2 += (contagem2B[i]);
  }}
  long result = total_B2+total_A1-(total_A2+total_B1);

  ////////// FILTRO SAVITZKY-GOLAY - ORDEM 1
    float coef[N] = {0.09090909,0.09090909,0.09090909,0.09090909,
    0.09090909,0.09090909,0.09090909,0.09090909,0.09090909,0.09090909,
    0.09090909};
    float soma1 =0;
    for(int i=0; i< N-1; i++){
      pll_buffer[i]=pll_buffer[i+1];
    }
      pll_buffer[N-1]=result;
    for(int j=0;j< N;j++){
      soma1 += coef[j] * pll_buffer[j];
    }
    pll_buffer[int((N-1)/2)]=soma1;
```

```
  //////////

  Serial.print("A");
  Serial.print("1");
  Serial.print("\t B");
  Serial.println(int(soma1));
}

void ODMR_Mode(){

  int intervalos = int((integra)/2);
  volatile uint32_t contagem1 [intervalos];
  volatile uint32_t contagem2 [intervalos];
  uint32_t aux [intervalos];
  long total_pos=0;
  long total_neg=0;

  int cnt1=0;
  int cnt2=0;

  // ZERAMENTO DO CONTADOR
  unsigned long timeout = 84000000; // 1s max for the next clock pulse
  unsigned long k=0;
  unsigned long zero=0;
  // Ver pag. 862, 36.6.6 (Trigger) no manual do SAM3X
  TC0->TC_CHANNEL[0].TC_CCR = TC_CCR_SWTRG
  // sowftware trigger: reset counter, start clock
  | TC_CCR_CLKEN;                // counter clock enabled
  zero = TC0->TC_CHANNEL[0].TC_CV;
  while((TC0->TC_CHANNEL[0].TC_CV == zero)&&(k<timeout)){
    k++;
```

```
}
while((PIOB->PIO_PDSR >> 25 ) & 1 == 0){}
while((PIOB->PIO_PDSR >> 25 ) & 1 == 1){}  // Aguardar fase com o sinal
for(int i=0;i<intervalos;i++){

  while(((PIOB->PIO_PDSR >> 25 ) & 1)==0){
  //ciclo negativo
      contagem1[i] = TC0->TC_CHANNEL[0].TC_CV;
      //leitura do registrador do TC0 - canal 0
  }
  while(((PIOB->PIO_PDSR >> 25 ) & 1)==1){
  //ciclo positivo
      contagem2[i] = TC0->TC_CHANNEL[0].TC_CV;
  }
}

 aux[0]=contagem2[0];
for(int j=1; j<intervalos; j++){
  aux[j]=contagem2[j];
  contagem2[j] -= (contagem1[j]);
  contagem1[j] -= (aux[j-1]);
}

contagem1[0] = 0;
contagem2[0] = 0;

for (int i=0;i<intervalos;i++){
  if((contagem1[i]!=0)&&(contagem2[i]!=0)){
  total_pos += contagem1[i];
  total_neg += contagem2[i];
  contagem1[i]=0;
```

```
    contagem2[i]=0;
    }
  }

  ////////// FILTRO SAVITZKY-GOLAY - ORDEM 1
    float coef[N] = {0.09090909,0.09090909,0.09090909,0.09090909,
    0.09090909,0.09090909,0.09090909,0.09090909,
    0.09090909,0.09090909,0.09090909};
    float soma1 =0;
    float soma2 =0;
    for(int i=0; i< N-1; i++){
      odmr_buffer_total_pos[i]=odmr_buffer_total_pos[i+1];
      odmr_buffer_total_neg[i]=odmr_buffer_total_neg[i+1];
    }
      odmr_buffer_total_pos[N-1]=total_pos;
      odmr_buffer_total_neg[N-1]=total_neg;
    for(int j=0;j< N;j++){
      soma1 += coef[j] * odmr_buffer_total_pos[j];
      soma2 += coef[j] * odmr_buffer_total_neg[j];
    }
    odmr_buffer_total_pos[int((N-1)/2)]=soma1;
    odmr_buffer_total_neg[int((N-1)/2)]=soma2;
  //////////

  Serial.print("A");
  Serial.print(int(soma1));          // REFERENCE: MICROWAVE OFF
  Serial.print("\t B");
  Serial.println(int(soma2));        // SIGNAL: MICROWAVE  ON */
}

void Set_current_frequency(uint16_t value){ //CHANGE THE CURRENT
```

```
  freq = value;
}
void Set_current_time_integration(uint16_t value){
// CHANGE THE INTEGRATION TIME
  integra = value;
}

void loop (){
  ComSerial rec;
  bool sair = 0;
  while (1) {
    while (mode == 0){ //avalia o trigger do counter
      Counter_Mode(); //executa o modo counter
      if (Serial.available()){
        rec = LerSerial();
        if (rec.conteudo == "PLL"){
          mode = 1;
          break;
        }
        if (rec.conteudo == "ODMR"){
          mode = 2;
          break;
        }
        else {
          sair = 1;
          break;
        }
      }
    }

     while (mode == 1){ //avalia o trigger do PLL
```

```
    PLL_Mode();//executa o modo PLL
    delay(10);
    if (Serial.available()){
      rec = LerSerial();
      if (rec.conteudo == "CNT"){
        mode = 0;
        break;
      }
      if (rec.conteudo == "ODMR"){
        mode = 2;
        break;
      }
      else {
        sair = 1;
        break;
      }
    }
  }
  while (mode == 2){ //avalia o trigger do ODMR
    ODMR_Mode();//executa o modo ODMR
    if (Serial.available()){
      rec = LerSerial();
      if (rec.conteudo == "CNT"){
        mode = 0;
        break;
      }
      if (rec.conteudo == "PLL"){
        mode = 1;
        break;
      }
      else {
```

```
            sair = 1;
            break;
          }
        }
      }
      if (sair == 1) break;
    }
    if (rec.conteudo == "*IDN?") {
     Serial.println("r:UNIVERSIDADE FEDERAL DE PERNAMBUCO");
      Serial.println("r:DEPARTAMENTO DE FISICA");
      Serial.println("r:CONTADORA DE FOTONS");
    }
    if (rec.conteudo == "PWM(,)"){
      if (rec.valor[0] <= 0 || rec.valor[1] >= rec.valor[0]){
        Serial.println("r:Insira valores validos. Consulte 'help?'");
      } else{
        pwm1(rec.valor[0],rec.valor[1]);
        Serial.println("r:PWM(I) ativado com sucesso - PINO DIGITAL 7");
      }
    }
    if (rec.conteudo == "SETCF()"){
      if (rec.valor[0] < 1 || rec.valor[0] > 40){
        Serial.println("r:Insira valores validos. Consulte 'help?'");
      } else{
        Set_current_frequency(rec.valor[0]);
      }
    }
    if (rec.conteudo == "SETCI()"){
      if (rec.valor[0] < 10 || rec.valor[0] > 200){
        Serial.println("r:Insira valores validos. Consulte 'help?'");
      } else{
```

```
            Set_current_time_integration(rec.valor[0]);
        }
    }
}
```

Design of the circuit to implement the microcontroller

The scheme of this circuit is designed to satisfy some requirements as the suitable signal that Ardunio Due needs to operate and performs the programmed tasks. Thus, it is implemented the circuit to broaden the pulse and control the tension level that feeds the digital input of the Arduino Due. The PWM Buffer is used to generate the pulse sequences and synchronize the tasks and the DAC Buffer to allocate information in the internal memory of the microcontroller.

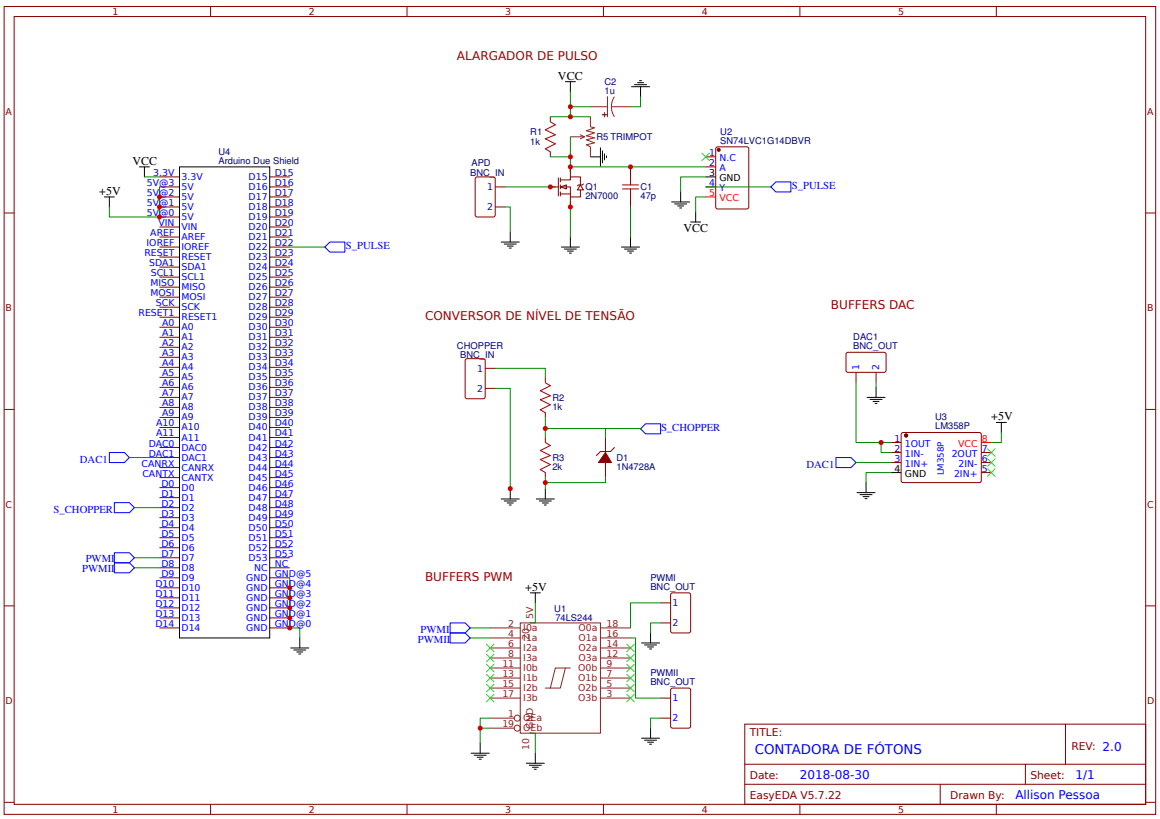

Figure 30: Scheme depicting the circuit of the photon counter that includes the circuit that switches the current to induce a modulated magnetic field B_{mod}.

Appendix B

Sample preparation

Photolithography

This technique is used to deposit the metallic material (gold) on the coverslip surface which is employed to drive microwaves. To begin with this procedure, first it is deposited by coating a negative photoresist on a coverslip, then a patterned mask is applied to the surface to block ultraviolet (UV) radiation such that only unmask regions of the resist material is exposed to the light. Afterwards, a solvent known as a developer is applied to the surface to remove only the regions that were not exposed to UV light. Once this is done, the next step is sputter Chromium (Cr) to form a thin layer of 5 nm used to improve adhesion of gold, which is the next layer with a thickness of 180 nm. The last layer deposited on the top is again Cr (5 nm) used to protect the gold layer from dissolution and damages during the developing of the structure, and its use as the antenna.

Cleaning the MW antenna

The process to clean the surface of the MW antenna is as follows

1. Use a basic piranha solution (H_2SO_4+H_2O_2 (4:1). Add first H_2SO_4) for eliminating the organic impurities. Prepare it and keep the MW transmission line in it for 10 minutes.

- If a piranha solution is not available, consider placing the sample in acetone and keeping in there for 30-60 minutes. Then, wash it boundary with deionized (DI) water.

2. Rinse with DI water

3. Place the sample in a becker with DI water, and when available use an ultrasonic bath for 1-5 minutes. The ultrasonic bath shall possibly operate with high ultrasound frequency (the best would be 80 to 130 kHz) and low power. If that is not available, it is possible to use a lower ultrasound (30-45 kHz) but with very low power. If these requirements are not satisfied, the transmission line could get damaged in few seconds.

4. After finishing, rinse with DI water a last time and dry with nitrogen. The spin coating of NDs on the antenna can proceed as in the following:

   (a) Place the MW antenna on the spin coater and apply vacuum.

   (b) Place a droplet of nanodiamond colloid (measuring 10 microliters with the micropipete) on the center of the MW antenna.

   (c) Set up the first spinning cycle to ramp 6 seconds until 1500 rpm

   (d) Set up the second spinning cycle at 2800 rpm for 20 seconds

   (e) The sample should be ready for being used in the experiments.

Appendix C

Second order correlation function

The second order correlation function $g^{(2)}(\tau)$ describes intensity correlations unlike the first order correlation that describes amplitude correlations. Moreover, $g^{(2)}(\tau)$ gives information about the statistics of the light field. Thus, one can determine whether a light source exhibits a quantum emitter behavior only observing a photon antibunching and sub-Poissonian statistic. The second order correlation function is defined as [100]

$$g^{(2)}(\tau) = \frac{\langle \mathcal{E}^*(t)\mathcal{E}^*(t+\tau)\mathcal{E}(t+\tau)\mathcal{E}(t)\rangle}{\langle \mathcal{E}^*(t)\mathcal{E}(t)\rangle\langle \mathcal{E}^*(t+\tau)\mathcal{E}(t+\tau)\rangle} = \frac{\langle I(t)I(t+\tau)\rangle}{\langle I(t)\rangle\langle I(t+\tau)\rangle} \tag{C.1}$$

where $\mathcal{E}$ is the electromagnetic field and the I is the intensity of the light beam. Equation C.4 considers measurements of intensity values pairs which are detected with a delay time τ.

Hanbury-Brown and Twins

The measurements of the correlation of two intensities can be express in terms of $g^{(2)}(\tau)$ using a Hanbury-Brown and Twins (HBT) [101, 102] interferometer. A beam incident on a 50:50 beam splitter is divided into two beams, and each beam strikes on an avalanche photodiode (APD) detector that generates a pulse signal going into an electronic counter (Time correlated single photon count (TCSPC)) that records the time elapsed between the first pulse produced by the APD1 when this detect one photon and the second pulsed

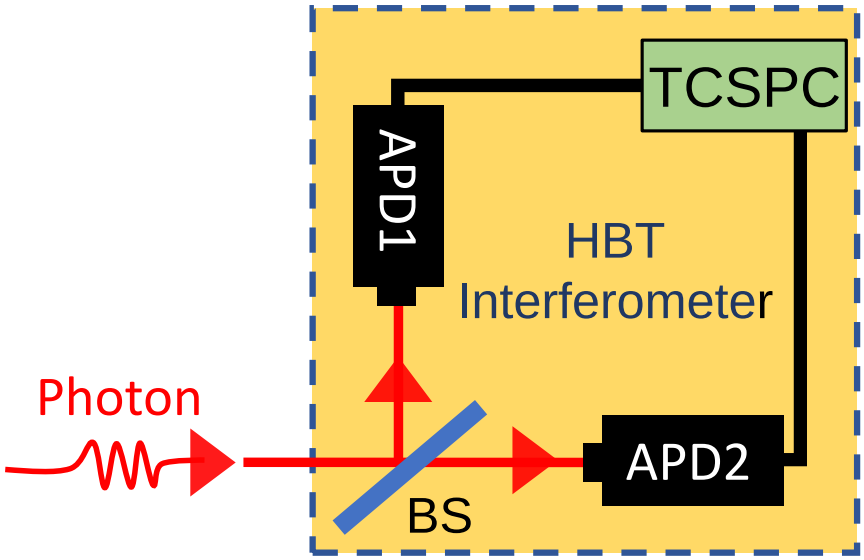

Figure 31: Experimental scheme of the Hanbury-Brown and Twiss setup used for realizing the intensity correlation measurements.

produced by the APD2 when this detect a second photon. The corresponding experimental scheme is in figure 31.

Since the number of photons (counts) is proportional to the intensity, we can rewrite the equation C.4 as a function of the counts registered by the detector at time t, as

$$g^{(2)}(\tau) = \frac{\langle n(t)n(t+\tau)\rangle}{\langle n(t)\rangle\langle n(t+\tau)\rangle} \tag{C.2}$$

Here one can express $g^{(2)}(\tau)$ making use of the creation and annihilation operators. Furthermore, it is considered that the first photon was detected at time $t = 0$:

$$g^{(2)}(\tau) = \frac{\langle \hat{a}^\dagger(0)\hat{a}^\dagger(\tau)\hat{a}(\tau)\hat{a}(0)\rangle}{\langle \hat{a}^\dagger(0)\hat{a}(0)\rangle\langle \hat{a}^\dagger(\tau)\hat{a}(\tau)\rangle} \tag{C.3}$$

It is helpful to understand the behavior of this correlation function when τ because it permits us to distinguish between different light statistics. So,

$$g^{(2)}(\tau = 0) = \frac{\langle \hat{a}^\dagger(0)\hat{a}^\dagger(0)\hat{a}(0)\hat{a}(0)\rangle}{\langle \hat{a}^\dagger(0)\hat{a}(0)\rangle\langle \hat{a}^\dagger(0)\hat{a}(0)\rangle} = \frac{\langle \hat{a}^\dagger\hat{a}^\dagger\hat{a}\hat{a}\rangle}{\langle \hat{a}^\dagger\hat{a}\rangle^2} \tag{C.4}$$

Using $\hat{n} = \hat{a}^\dagger \hat{a}$ and the commutation relation $\left[\hat{a}, \hat{a}^\dagger\right] = 1$, the second-order correlation function can be express in terms of the photon numbers for $\tau = 0$

$$\begin{aligned} g^{(2)}(\tau = 0) &= \frac{\langle \hat{a}^\dagger (\hat{a}\hat{a}^\dagger - 1)\hat{a} \rangle}{\langle \hat{a}^\dagger \hat{a} \rangle^2} \\ &= \frac{\langle \hat{n}\hat{n} \rangle - \langle \hat{n} \rangle}{\langle \hat{a}^\dagger \hat{a} \rangle^2} \\ &= 1 - \frac{1}{n} \end{aligned} \tag{C.5}$$

The last equation provides an easy way to find out whether the detected light is the result of a coherent source or a single photon emitter. This type of distinction is crucial in the present work because it is looking for single photon emitters. Equation C depends only on one variable, n, which is the number of photons emitted. Thus, measuring $g^{(2)}(0)$ one can know if single photons are produced. For example, coherent states reproduce classic electromagnetic waves in the limit of a large number of photons. Thus, when $n \to \infty$ one gets $g^{(2)}(0) = 1$ for coherent light. When $g^{(2)}(0) = 0$ is measured one is detecting single emitters. Theoretically, in the special case that $g^{(2)}(0) = 0$, n can be considered both as a number of photons and/or a number of emitters. However, to obtain $g^{(2)}(0) = 0$ experimentally is not possible due to the electronic noise generated in the APDs and the efficiency limited by their dead time. In this sense it is enough for to obtain $0 < g^{(2)}(0) < 0.5$ ($g^{(2)}(0) = 0.5$ when $n = 2$) because with that one strictly verifies the detection of single emitter [100, 103].

Appendix D

Works done during the D.Sc. Program

Contributions to conferences

[1] E. Sánchez, B. Bononi and L. de S. Menezes, "Coherent dynamics of a single nitrogen-vacancy defect in nanodiamond observed using optically detected magnetic resonance." Poster in the 10th International Conference on Nanophotonics, Recife-PE (2017). This poster got Honorific Mention from the organizing committee.

[2] E. Sánchez, B. Bononi and L. de S. Menezes, "Estudio de propiedades ópticas y de spin en nanodiamantes con defectos individuales de Nitrógeno-Vacancia usando Resonancia Magnética Ópticamente Detectada." Oral presentation in the XXV Encuentro Científico Internacional de Verano, Lima, Peru (2018).

[3] E. Sánchez, A. Pessoa, A. Amaral and L. de S. Menezes, "Optically detected magnetic resonance with single nitrogen-vacancy centers in nanodiamond for magnetic field sensing with nanometric spatial resolution." Oral presentation in the Encontro de Outono da Sociedade Brasileira de Física, Aracaju-SE (2019).

[4] E. Sánchez, A. Pessoa, A. Amaral and L. de S. Menezes, "Medida da orientação do momento do dipolo magnético de um defeito de nitrogênio vacância individual

em nanodiamante." Poster in the XXXIV Encontro de Físicos do Norte e Nordeste, Maceió-AL (2019).

[5] E. Sánchez, A. Pessoa, A. Amaral and L. de S. Menezes, "Sensoriamento de campos manéticos AC usando nanodiamantes contendo defeitos de nitrogênio vacância individuais." Oral presentation in the XXXIV Encontro de Físicos do Norte e Nordeste, Maceió-AL (2019).

[6] E. Sánchez, A. Pessoa, A. Amaral and L. de S. Menezes, "Implementation of a nanomagnetometer using a single nitrogen-vacancy defect in nanodiamond." Poster in the II Instituto Nacional de Fotônica (INFo) Workshop, Araraquara-SP (2020).

Published paper

[7] E. Sánchez, A. Pessoa, A. Amaral and L. de S. Menezes, "Microcontroller-based magnetometer using a single nitrogen-vacancy defect in a nanodiamond." AIP Adv. **10**, 025323 (2020).